



EUROPEAN MECHANICAL SCIENCE

 OPEN
ACCESS

ISSN: 2587-1110

Volume 5
Issue 3
June 2021



Editor in Chief: M. Ozcanli

Editor in Chief

Mustafa Ozcanli (Automotive Engineering, Cukurova University, Turkey)

Editors

Sandra Spaszkiwicz (West Pomeranian University of Technology, Poland)
Iva Petrikova (Applied Mechanics, Technical University of Liberec, Czech Republic)
Elżbieta Piesowicz (West Pomeranian University of Technology, Poland)
Tomeh Elias (Vehicles and Engines, Technical University of Liberec, Czech Republic)
Aleksandra Borsukiewicz, West Pomeranian University of Technology, Poland
Alptekin Ergenç (Automotive Engineering, Yildiz Technical University, Turkey)
Hasan Serin (Automotive Engineering, Cukurova University, Turkey)
M. Atakan Akar (Automotive Engineering, Cukurova University, Turkey)
Ahmet Çalık (Mechanical and Metal Technologies, Mersin University, Turkey)
Tayfun Ozgur (Automotive Engineering, Cukurova University, Turkey)

Layout Editor

Ahmet Calik (Mersin University, Turkey)

Secretary

Şafak Yıldızhan (Cukurova University, Turkey)

Indexed / Abstracted in:

TR-Dizin, CrossRef, Index Copernicus, Journal Factor, Rootindexing, ResearchBip, JournalFactor, JIFACTOR, Google Scholar, I2OR, Cosmos Impact Factor, International Innovative Journal Impact Factor (IIJIF), Scientific Indexing Services, InfoBase Index, Scientific Journal Impact Factor

Aims and Scopes

European Mechanical Science (EMS) is an international, peer reviewed journal which publishes full length original research papers, reviews related to all areas of Mechanical Engineering such as: Solid Mechanics, Materials Engineering, Automotive Engineering, Fluid Mechanics, Thermal Engineering, Engine and Power Engineering, Dynamics & Control, Robotics & Mechatronics, Transportation Engineering, Computational Mechanics, Design, Systems, Manufacturing, Bio-Medical Engineering; Process Engineering, Aerospace Engineering. No charges are required from the Authors to publish the articles.EMS is a quarterly published journal operating an online submission and peer review system. It allows authors to submit articles online and track their progress via its web interface.

<http://dergipark.gov.tr/ems>

Contents

— *Research Paper*

- Fracture Analysis of a Case-Hardened Kingpin 92
Tuğrul Soyusinmez, Oğuzcan Güzelipek, Tolga Palandüz, Onur Ertuğrul
- High Voltage Gain Multi-port Bidirectional DC-DC Converter with an Effective Multi-loop Control Strategy for PV/Battery Integrated Systems 99
Murat Mustafa Savrun, Alihan Atay
- Effect of Fabric Structural Parameters on Various Comfort Properties of Automobile Seat Cover Fabrics 105
Mine Akgun, Hayrūnnisa Aydan Kamacı
- A preliminary Investigation of Surface Micro Modification Effects on the Biocompatibility of 316L Stainless Steel 109
Sıdıka Mine Toker, Erdoğan Serhad Özbulut, Zübeyir Kolçak, Esra Güner
- Effect of Build Orientation on Mechanical Behaviour and Build Time of FDM 3D-Printed PLA Parts: An Experimental Investigation 116
Meltem Eryildiz
- Characterization of Mechanical of CTBN Liquid Rubber-Modified Epoxy Cured by Anhydride- and Amine-Based Agent 121
Harun Sepetcioglu
- Static Analysis of Trailers with Demountable Chassis 130
Tuğba Gedik, Mehmet Vurgun, Banu Özkeser, Erhan Biçer
- Estimating Global Solar Radiation from Empirical Models: An Application 135
Özgür Ballı
- Electromagnetic Analysis of Organic Waste and Blast Furnace Slag Mixtures 148
Mustafa Kaan Baltacıoğlu, Mustafa Tunahan Başar, Muharrem Karaaslan, Fatih Özkan Alkurt, Samet Alparslan Aripek



Fracture Analysis of a Case-Hardened Kingpin

Tuğrul Soyusinmez^{1*} , Oğuzcan Güzelipek¹ , Tolga Palandüz¹ , Onur Ertuğrul² 

¹Totomak A.Ş., İzmir, Turkey

²İzmir Katip Çelebi University, Dept. of Materials Science and Engineering, İzmir, Turkey

Abstract

Kingpin parts are one of the critical products for heavy vehicles and are generally made of 20MnCr5 steel. A kingpin is a heavy metal cylindrical pin that is located underneath the front end of the trailer. The kingpin is the mechanism on the trailer that locks it to a road tractor. The parts in this study have undergone to case hardening heat treatment after the rough machining operation. During the operation in the assembly line, cracks have been realized on the surface of the parts. In this study, the kingpin parts are examined with optical microscopy, Scanning Electron Microscopy (SEM), hardness tests and %C potential analysis in order to determine the potential causes of the crack formations. By the help of the analysis, the presence of cracks became clear. There are no signs of hydrogen embrittlement. The exact outcome of the fracture could not be determined. It is seen that heat treatment of the parts is not homogeneously obtained throughout their surfaces or desired volume, and therefore fractures occur. With the present structure, it can be expected that even a low dynamic load can lead to breakage. As a result, the investigations suggest that the parts were exposed to inappropriate heat treatment parameters.

Keywords: Kingpin, Case Hardening, Scanning Electron Microscopy (SEM), Crack formation, 20MnCr5 steel

1. INTRODUCTION

The n-trailer system is a unlike a flat system, who is flat (or linearizing) outputs are the Cartesian coordinates of the middle point of last trailer's rear axle. Mobile robots with trailers are flat systems as soon as the trailers are hitched to the middle point of the axle of the previous ones. Placing the king pin off the axle will cause the system not to be straight. The placement of the kingpin outside the axle makes the system not flat.[1] The kingpin sliding mechanism allows the kingpin to slide along the axle of the previous trailer. From the perspective of routing and control theory, a natural question is whether the system remains flat. It is also proved that the n-trailer system equipped with a sliding kingpin mechanism is a differentially flat system [2].

Steels used for surface hardening generally contain a carbon content of about 0.2%, and the carbon content of the carburized layer generally being controlled at between 0.7 and 1% C. However, the carbon content on the surface should generally not exceed 0.9% because high carbon content can result in retained austenite and brittle martensite (due to the formation of proeutectoid carbides on the grain boundaries) [3].

Surface hardening is a process that has been used for many years to improve the surface hardness of metals. Fast heating and rapid quenching methods are used to increase the surface hardness. Surface hardening is observed with the changes provided in the microstructure [4]. The compressive residual stresses prolong the fatigue lifetime of the hardened component. In the surface induction hardening process, heating is very fast and directly followed by quenching, so the generation of residual stresses is more complex than the common hardening process [5]. Calculating the variation of heat generation rate in components with a complex geometry is difficult, therefore the experimental measurements of surface heat fluxes are also used. Many finite element studies focused on the prediction of residual stresses in components during heating and quenching and a few papers on the surface induction hardening have been published in the past years. The finite element method (FEM) makes it possible to estimate the residual stresses in components during heating and quenching to determine the relationship between process parameters and the mechanical properties of the material being processed [6].

For iron or steel parts with low carbon content, which has poor hardenability due to the chemical composition, the

* Corresponding author
Email: tsoyusinmez@totomak.com.tr



case hardening process involves infusing additional carbon or nitrogen into the surface layer. Case hardening is usually applied after the part has been formed into its final shape, however, can also be applied to increase the hardening element content of bars to be used in a pattern welding or similar process: Case hardening process is applied intensively on parts subjected to high pressure or sharp impacts. Firing pins, rifle faces, engine crankshafts can be shown as examples of parts that have been processed. In these cases, the surface may be hardened selectively, leaving the center of the part in its original tough state [7,8].

Stress corrosion cracking and intergranular corrosion of are the most important corrosion types those affect the service behavior of austenitic stainless steels. Dissimilar material and environmental factors affect stress corrosion cracking behavior of austenitic stainless steels. The environmental factors include the processes of forming by cold plastic deformation and seam welding. The latter justifies that there is a growing interest in knowing the effect that prior to cold work and sensitization treatment have on the stress corrosion cracking behavior of these types of materials [9,10].

In this work, the reasons of a sudden failure of a steel part during its assembly have been investigated in detail. By conducting many experimental studies, a detailed fracture analysis has been made. The aim of the analysis is also to investigate the effects of the heat treatment parameters for determining the fracture of the kingpin parts.

2. MATERIAL AND METHODS

The spectral analysis, metallography and fractography studies, SEM analysis and hardness tests were carried out for the 16MnCr5 steel parts, respectively. The image of the kingpin part broken in assembly lines is shown in Figure 1. The chemical composition of the analyzed 16MnCr5 steel is shown in Table 1, and the mechanical properties are given in Table 2.

Table 1. Chemical composition of 16MnCr5 (1.7131) steel (wt.%)

| C | Si | Mn | P | S | Cr |
|-------------|---------|---------|-----------|-----------|-----------|
| 0.14 - 0.19 | max 0.4 | 1 - 1.3 | max 0.025 | max 0.035 | 0.8 - 1.1 |



Figure 1. Images of the (a)original, and (b)broken kingpin part

Table 2. Mechanical properties of the 16MnCr5 (1.7131) steel

| Property | Value |
|--|-------|
| Nominal thickness (mm): | to 16 |
| Rm - Tensile strength (MPa) hardening and tempering at 200°C | 1000 |
| Rm - Tensile strength (MPa) | 550 |
| Rp0.2 0.2% proof strength (MPa) | 420 |
| A - Min. elongation Lo = 80 mm (%) | 21 |
| Z - Reduction in cross section on fracture (%) | 62-64 |
| Vickers hardness (HV) | 170 |

Before the macroscopic examinations, the fracture surfaces were cleaned in an ultrasonic bath, and then examined under a stereo microscope. For further investigation, samples were prepared through the examined part. The locations where samples were taken out are shown in Figure 2. The samples were taken from three different positions and have been encoded as follows: RD-Radius (05-20-0619-1), FR-Fracture surface (05-20-0619-2), and FL-Flange (05-20-0619-3). Representative coding's are given in Table 3.

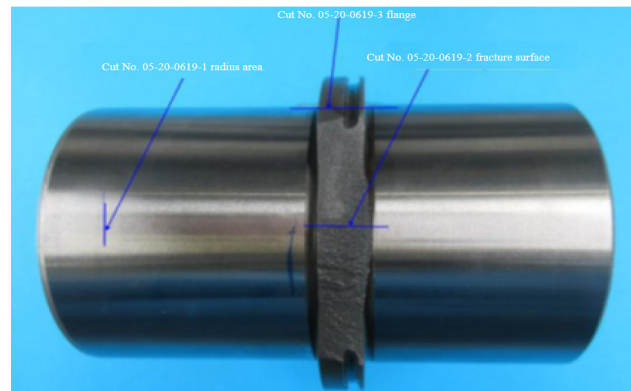


Figure 2. The locations where samples were taken out

Table 3. Representative coding's belong to three different locations.

| Sample Code | Location | Long name |
|-------------|------------------|--------------|
| RD | Radius | 05-20-0619-1 |
| FR | Fracture surface | 05-20-0619-2 |
| FL | Flange | 05-20-0619-3 |

In order to understand the reasons of the kingpin's failure, the broken failure areas were examined by Scanning Electron Microscopy (SEM). Also, Vickers set hardness tests, using 1 kg load, were carried out on from the surface of the

samples after heat treatment in order to determine the hardness depth of the parts.

3. RESULTS AND DISCUSSION

All the samples were examined from their cross-section by a light microscope. The images of the RD sample from its surface area with different magnifications have been shown in Figure 3, which present mainly the martensitic microstructure. And the microstructure belongs to the center part of the radius section containing mixed structure of bainite and coarse martensite phases which is shown in Figure 4. Moreover, the images from the cross section of the fracture surface with different magnifications have been shown in Figure 5. It is clearly shown here that the microstructure

consists of a mixed structure containing bainite and coarse martensite phases.

The surface area belongs to flange section contain hard martensitic structure as shown in Figure 6. And the microstructure belongs to the center part of the flange section having the mixed structure of bainite and coarse martensite phases are shown in Figure 7.

The metallographic investigations for both RD and FL samples show that there is a hard martensitic structure without any mesh or bone type carbide at the surface zones. In the center, there is an inhomogeneous mixed structure of bainite and coarse martensite phases. It can be assumed that the structure shows high strength. Based on the cen-

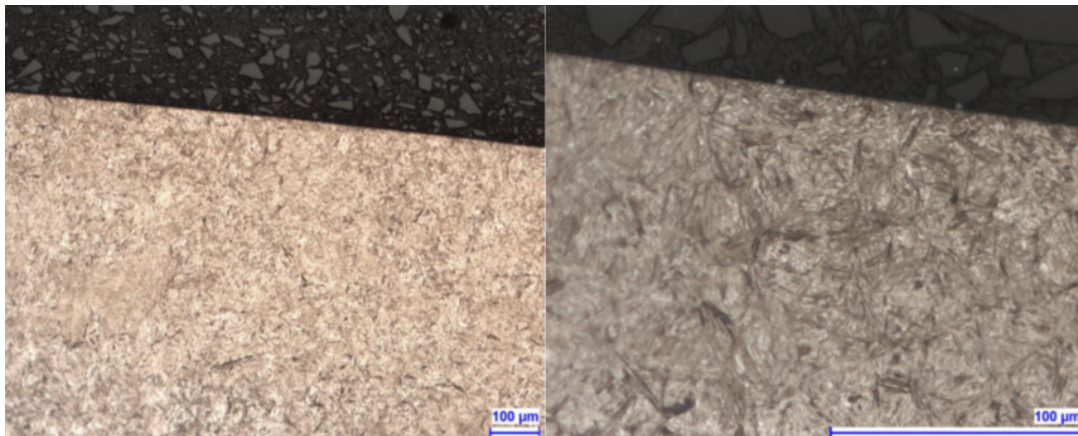


Figure 3. Surface structure of the RD sample showing the martensitic structure

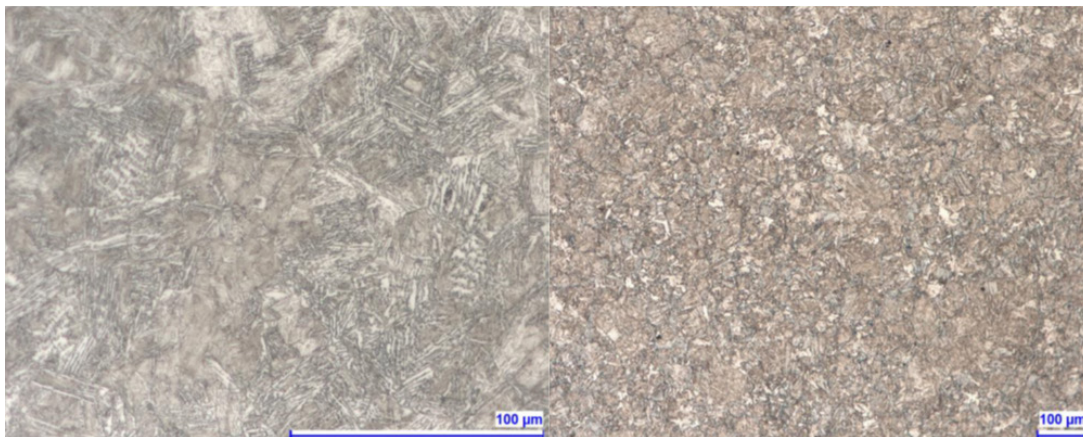


Figure 4. Mixed structure of bainite and coarse martensite phases on the center part of RD sample



Figure 5. Images of the FR sample showing a mixed structure of bainite and coarse martensite phases

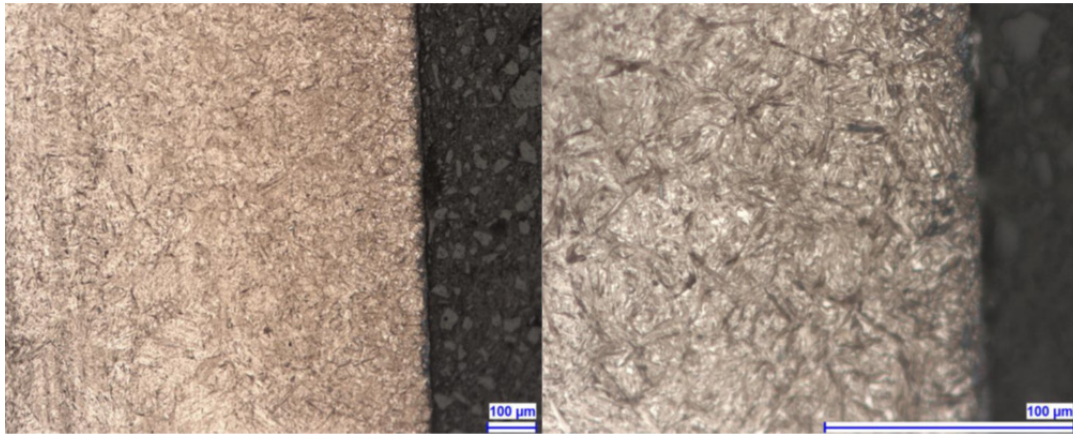


Figure 6. Surface structure of the FL sample having hard martensitic structure

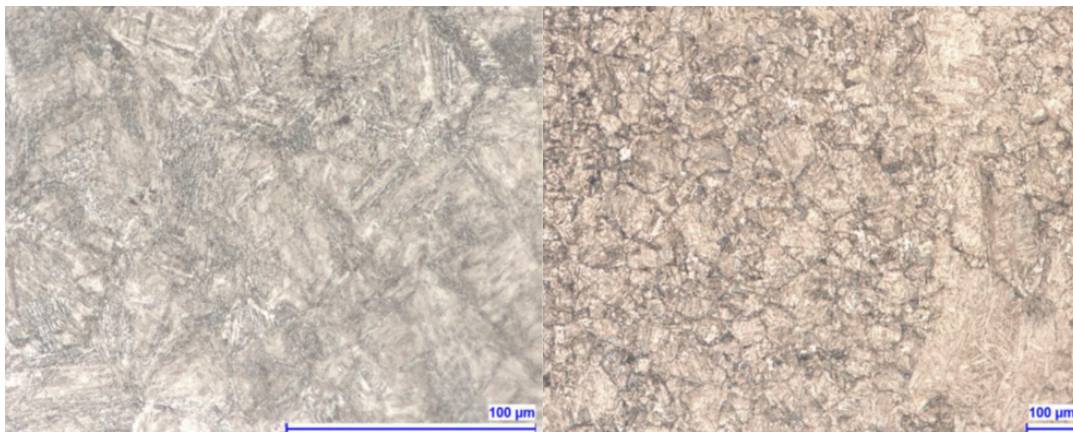


Figure 7. Flange area mixed structure of bainite and coarse martensite components

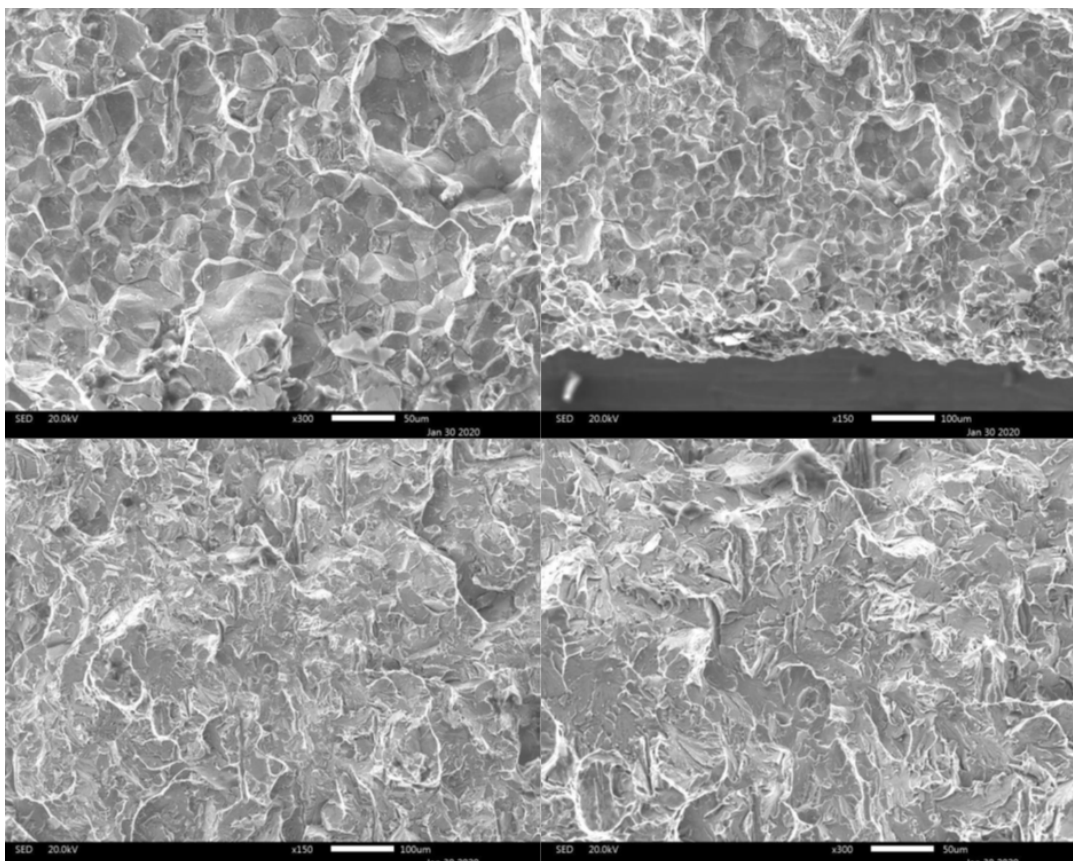


Figure 8. SEM images of different areas from the broken parts

ter structure and the determined core strength, it could be predicted that the component has little ductility and toughness. This can also be concluded with the presence of a shiny surface. However, in the area where the fracture occurred (FR sample), there is a mixed structure of bainite and coarse martensite phases also in the surface zone.

SEM images taken from the fracture surfaces with different magnifications are shown in Figure 8. It is seen from the figure that intergranular fracture (which is a sign of brittle fracture) is valid in the surface zone. And a mixed mode with cleavage type of fracture is visible in the core center part of the sample.

The polished cross section prepared from the radius area of the part is shown in Figure 9, and the hardness test results are given in Table 3 and Figure 10. It is known that Bainite phase is formed at slower cooling rates more than that for martensite formation and faster than that for ferrite and pearlite microstructure and martensite is formed when the cooling rate from austenitic microstructure is sufficiently fast. So, these hardness results confirm the microstructural analysis mostly.

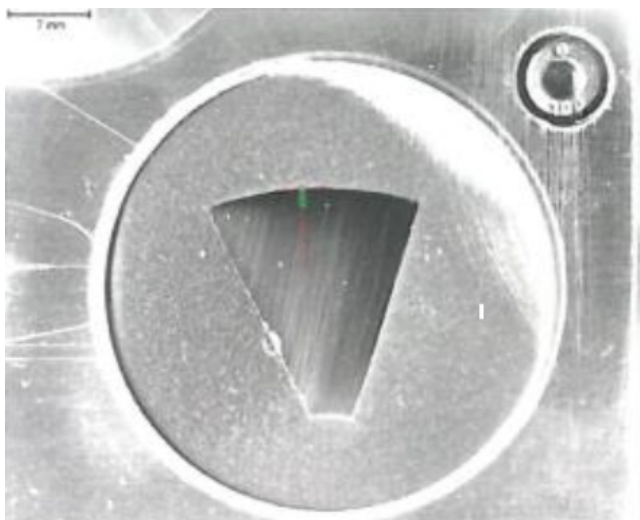


Figure 9. Prepared hardness test sample from the radius area

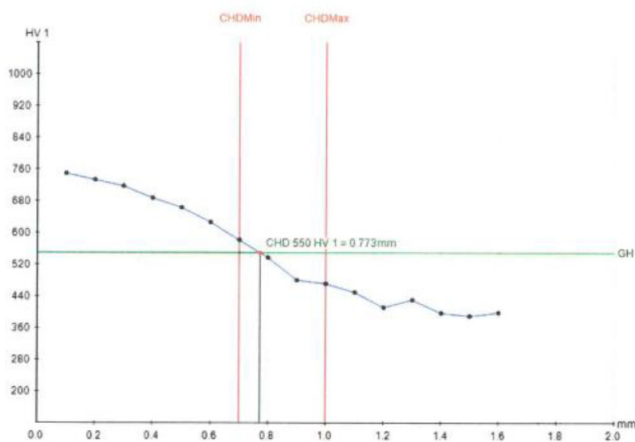


Figure 10. Graphical hardness test results of the RD sample

The polished cross section prepared from the fracture area of the part is shown in Figure 11, and the hardness test results are given in Table 4 and Figure 12.

Table 3. Hardness test results belong to RD sample.

| Step | Result (HV) | X- Position (mm) | Y- Position (mm) | Hardness Depth 550 HV1 |
|------|-------------|------------------|------------------|------------------------|
| 1 | 750 | 0,1 | 0 | 0,773 mm |
| 2 | 734 | 0,2 | 0,2 | |
| 3 | 718 | 0,3 | 0 | |
| 4 | 688 | 0,4 | 0,2 | |
| 5 | 664 | 0,5 | 0 | |
| 6 | 627 | 0,6 | 0,2 | |
| 7 | 582 | 0,7 | 0 | |
| 8 | 538 | 0,8 | 0,2 | |
| 9 | 481 | 0,9 | 0 | |
| 10 | 472 | 1 | 0,2 | |
| 11 | 450 | 1,1 | 0 | |
| 12 | 412 | 1,2 | 0,2 | |
| 13 | 431 | 1,3 | 0 | |
| 14 | 398 | 1,4 | 0,2 | |
| 15 | 390 | 1,5 | 0 | |
| 16 | 399 | 1,6 | 0,2 | |

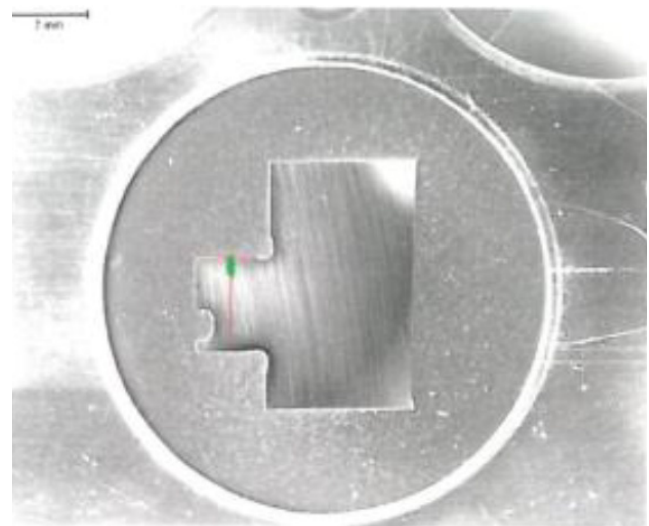


Figure 11. Prepared hardness test sample from the fracture area

Table 4. Hardness test results belong to FR sample.

| Step | Result (HV) | X- Position (mm) | Y- Position (mm) | Hardness Depth 550 HV1 |
|------|-------------|------------------|------------------|------------------------|
| 1 | 755 | 0,1 | 0 | 0,794 mm |
| 2 | 751 | 0,2 | 0,2 | |
| 3 | 702 | 0,3 | 0 | |
| 4 | 680 | 0,4 | 0,2 | |
| 5 | 657 | 0,5 | 0 | |
| 6 | 613 | 0,6 | 0,2 | |
| 7 | 579 | 0,7 | 0 | |
| 8 | 548 | 0,8 | 0,2 | |
| 9 | 533 | 0,9 | 0 | |
| 10 | 509 | 1 | 0,2 | |
| 11 | 475 | 1,1 | 0 | |
| 12 | 461 | 1,2 | 0,2 | |
| 13 | 436 | 1,3 | 0 | |
| 14 | 435 | 1,4 | 0,2 | |
| 15 | 438 | 1,5 | 0 | |
| 16 | 425 | 1,6 | 0,2 | |

As a result of the analysis, the exact outcome reason of the fracture could not be determined as there are no clear signs of possible failure types such as hydrogen embrittlement

failure. The only clear outcome is the presence of the brittle type of fracture mode especially in the surface part, which is concluded by the help of the SEM study. With the present structure it is to be expected that even a low dynamic load can lead to the sudden failure. Hydrogen absorption with martensitic structure causes cracks to occur on the weakest point of part, especially on the steel parts which become particularly brittle.

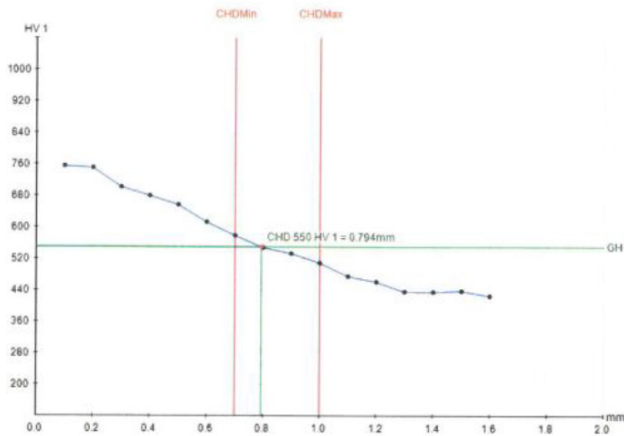


Figure 12. Graphical hardness test results of the FR sample

4. CONCLUSIONS

This study was conducted on the parts those are used as pins in the truck axles, and this detailed examination has emerged due to the sudden break of the part during assembly. The fracture is a brittle one. Based on the core structure and the determined core strength, it can be assumed that the component has no very low ductility or toughness. With the present structure it is to be expected that even a low dynamic load can lead to breakage. As a result, the following conclusions can be drawn:

1. The metallographic examination shows that there is a martensitic hardness structure without mesh or bone carbide at the edge.
2. In the core there is an inhomogeneous mixed structure of bainite and coarse martensite components.
3. It can be assumed that the structure shows high strength.
4. The investigations carried out suggest that the component was exposed to incorrect heat treatment parameters.
5. As a result of the work, it has been concluded that the heat treatment of the parts is not homogeneously distributed and therefore fractures occurred.

It is a target to prevent premature failures that may occur due to material selection, design, manufacturing, or heat treatment. It is very important for heat treatment companies to understand the cause of the break and to work on this issue. In addition, engineers and designers need to understand the effect of heat treatment to eliminate problems related to longevity and service performance.

CONFLICT OF INTEREST

There is no conflict of interest in this article.

REFERENCES

- [1] Jaroslav, M. (2003). Finite element analysis and simulation of quenching and other heat treatment processes. *Computational Materials Science*, 27, 313-332.
- [2] Ono, T., & Allaire, R. A. (2000). Fracture analysis, a basic tool to solve breakage issues. Taiwan FPD Expo 2000.
- [3] Garcia, C., Martin, F., De Tiedra, P., Heredero, J. A., & Aparicio, M. L. (2001). Effects of prior cold work and sensitization heat treatment on chloride stress corrosion cracking in type 304 stainless steels. *Corrosion science*, 43(8), 1519-1539.
- [4] Goldstein, J. I., Newbury, D. E., Michael, J. R., Ritchie, N. W., Scott, J. H. J., & Joy, D. C. (2017). *Scanning electron microscopy and X-ray microanalysis*. Springer.
- [5] Budinski, K. G. (1988). *Surface Engineering for Wear Resistance*. (Retrospective Coverage). Prentice-Hall, Inc, Englewood Cliffs, New Jersey 07632, United States
- [6] Krauss, G. (1990). *Steels: heat treatment and processing principles*. ASM International, 497.
- [7] Drozda, T., & Wick, C. (1985). *Tool and Manufacturing Engineers Handbook: Materials, Finishing and Coating (Vol. 3)*. Society of Manufacturing Engineers.
- [8] Grube, W. L., & Gay, J. G. (1978). High-rate carburizing in a glow-discharge methane plasma. *Metallurgical Transactions A*, 9(10), 1421-1429.
- [9] Akiniwa, Y., Stanzl-Tschegg, S., Mayer, H., Wakita, M., & Tanaka, K. (2008). Fatigue strength of spring steel under axial and torsional loading in the very high cycle regime. *International Journal of Fatigue*, 30(12), 2057-2063.
- [10] Meyers, M. A., & Chawla, K. K. (2008). *Mechanical behavior of materials*. Cambridge university press.
- [11] Shipley, R. J., Becker, W. T., & ASM, H. V. (2002). *Failure analysis and prevention*. ASM handbook, 11, 508.
- [12] ASTM E 350 (2000). *Standard Test Methods for Chemical Analysis of Carbon Steel, Low-Alloy Steel, Silicon Electrical Steel, Ingot Iron, and Wrought Iron*, 2000.
- [13] SAE J 404 Standard, *Chemical Compositions of SAE Alloy Steels* (2009). *International Journal of Engineering Research & Science (IJOER)*, 2(6) June-, p. 109
- [14] ASTM E 112 (2006) *Standard Test Methods for Determining Average Grain Size*
- [15] ASTM A 370 (2007). *Standard Test Methods and Definitions for Mechanical Testing of Steel Products*.
- [16] Hull, D. (1999). *Fractography: observing, measuring and interpreting fracture surface topography*. Cambridge University Press.
- [17] Vargas-Arista, B., Teran-Guillen, J., Solis, J., García-Cerecero, G., & Martínez-Madrid, M. (2013). Normalizing effect on fatigue crack propagation at the heat-affected zone of AISI 4140 steel shielded metal arc weldings. *Materials Research*, 16(4), 722-778.
- [18] Shoffner, B. W. (2008). Development and validation of a finite element analysis model used to analyze coupling reactions between a tractor's fifthwheel and a semitrailer's kingpin.
- [19] Dieter, G. E., & Bacon, D. J. (1976). *Mechanical metallurgy (Vol. 3)*. New York: McGraw-hill.

- [20] Gao, F. M., & Gao, L. H. (2010). Microscopic models of hardness. *Journal of superhard materials*, 32(3), 148-166.



High Voltage Gain Multi-port Bidirectional DC-DC Converter with an Effective Multi-loop Control Strategy for PV/Battery Integrated Systems

Murat Mustafa Savrun^{1*} , Alihan Atay² 

¹Adana Alparslan Türkeş Science and Technology University, Department of Electrical & Electronics Engineering, 01250, Adana, Turkey

²Solvaytech Engineering Industry and Trade LTD. Co., Adana, Turkey

Abstract

This study proposes a novel isolated bidirectional multi-port converter (MPC) based on a switched-capacitor converter and a half-bridge converter with an effective control scheme for photovoltaic (PV) powered and battery buffered systems. The proposed power electronics converter interface integrates the converters to the ports which are connected with a battery coupled common DC busbar and high-frequency transformer (HFT). Thus, the three-port converter is formed without any need for an additional converter to regulate battery power flow. In addition, to transfer power from a low voltage PV energy unit to the battery and load, a single switch DC-DC converter with high voltage gain is proposed. The power flow between the ports is controlled by an effective multi-loop control scheme that is able to perform a smooth transition between the loops. In order to validate the viability and effectiveness of the proposed MPC, a proof-of-concept simulation model has been developed with a 3 kW PV and 220 V 12 Ah battery. The performance of the proposed converter has been analyzed for different case studies, including dynamic operating and loading conditions.

Keywords: Multi-port DC-DC converter, switched-capacitor, photovoltaic, battery, multi-loop controller

5. INTRODUCTION

5.1. Overview

In the last few decades, the use and depletion of fossil fuels have accelerated in parallel with the significant increase in electricity demand [1]. The environmental concern and depletion of fossil fuels have led to develop renewable energy sources (RESs) powered clean applications such as electric vehicles [2], microgrids [3], residential grid-tie inverters [4]. Besides, RESs generating power in DC form are able to integrate with DC loads used in DC microgrids, which have become widespread in recent years, without using additional inverter devices [5]. Although RESs are good candidates for the aforementioned applications because of such advantages, they are by nature unstable in their availability and capacity [6]. The instantaneous production values of RESs vary with natural conditions such as solar irradiation/temperature [7], hydrogen pressure/temperature [8], and wind speed [9]. RES-based energy systems are frequently equipped with energy storage units in order to eliminate the non-linear behavior drawback of RESs. Battery units make it possible to provide uninterrupted power to loads by buffering fluctuations and interruptions of RESs.

The power flow between the RE- based energy unit, battery unit, and load is performed using power electronics converter interfaces. Traditionally, individual converters are employed and controlled in a decentralized manner to regulate the power flow [10]. Because of that, traditional RES-powered systems have high computational loads and costs. To overcome the aforementioned limitations, multi-port converters (MPC) are used, wherein RES-based energy units, battery units, and loads are connected to different ports of the MPC.

5.2. Literature Survey

MPCs are emerging power electronics solutions in order to integrate multi-inputs/outputs with combined functionalities and control schemes. MPCs can be divided into two categories as isolated and non-isolated converters and are presented in [11-13]. Non-isolated topologies have advantages such as simpler structure and compactness by the lack of a high-frequency transformer whereas they are not able to provide isolation and flexible voltage range [14]. On the other hand, isolated MPCs provide flexible voltage ranges via HFT turns ratio as well as isolation between the ports.

* Corresponding author
Email: msavrun@atu.edu.tr



Isolated MPCs are good candidates for RES powered and battery buffered systems because of their flexibility in performing power flow between the different ports.

Several isolated MPC topologies have been presented in the literature to integrate multi-input/output ports. Many studies have addressed isolated MPCs using the derivations of bridge converters that have capabilities of bidirectional power flow, galvanic isolation, zero-voltage switching, and zero-current switching [15]. Among the derivations of bridge converters, full-bridge converters have advantages of two times higher output voltage and higher power transfer capability, while half-bridge topologies with fewer switching devices are advantageous in relatively low power applications [16]. The turns ratio of HFTs makes it possible to provide flexibility in voltage conversion ratio, while the high turns ratio raises the problem of low efficiency. Therefore, MPCs that are endowed with low turns ratio HFTs and integrated with high gain converters stand out as in [7]. The power flow path at the MPC port where RESs are connected is designed to be unidirectional due to the nature of RESs. Because of that, RESs are equipped with unidirectional DC-DC converters. Various unidirectional high gain DC-DC converter topologies developed and applied in literature are reviewed in [17]. Step-up DC-DC converters temporarily store low voltage input energy on magnetic field storage components and transfer it to the output in high voltage levels [17]. The fundamental step-up converter is the traditional boost converters which have a restricted voltage gain with high output voltage ripple. In order to eliminate the output voltage ripples, interleaved topologies have been proposed [18]. Furthermore, multi-leg/multi-phase interleaved [19, 20], capacitor clamped h-bridge [21], and tristate boost converter [22] topologies are employed in order to further decrease the output voltage ripple and to improve the voltage conversion ratio. However, the related topologies have a limited gain and many active switching devices. The coupled inductor topologies make it possible to provide high voltage gain, but relatively large current ripples decay the service life of the connected port RES or battery unit [21]. Tang et al. [23] proposed a hybrid switched inductor converter. The switched inductor topology has a high voltage gain. However, the voltage stress on the diodes is the main drawback of the

related topology.

5.3. Key Contributions

Literature review reveals the current researches focused on MPCs in order to integrate multi-input/output ports with reduced switches and complexity. In addition, it is concluded that the unidirectional DC-DC converters that have a high voltage conversion ratio to extract maximum power from RESs play a critical role for RES-powered systems. Among the related DC-DC converter topologies, switched-capacitor boost converter and half-bridge converter excel with the aforementioned advantages.

This paper proposes a new MPC that is equipped with switched-capacitor DC-DC converter in order to integrate RES with an isolated DC-DC converter via a battery coupled common busbar. Since an additional DC-DC converter that regulates the power flow of the battery contributes significantly to the size and cost of the overall system, the power flow of the battery is regulated by the existing converters considering operation conditions. The proposed system is equipped with a multi-loop control structure that operates adaptively and allows instantaneous switching between the loops. In order to validate the viability and effectiveness of the proposed system, different load and temperature scenarios are operated.

The pattern of this study is organized as follows: the power circuit configuration of the proposed system is given in Section 2. In Section 3, the operation modes of the proposed MPC and overall control scheme are explained in detail. Performance analysis and case studies are investigated and discussed in Section 4. Finally, conclusions are presented in Section 5.

6. POWER CIRCUIT CONFIGURATION OF THE PROPOSED CONVERTER

The power circuit configuration of the proposed MPC which is illustrated in Figure 1 consists of a half-bridge converter, a controlled full-wave rectifier, a switched-capacitor DC-DC converter, and a secondary center-tapped high-frequency transformer (HFT). The proposed converter interface is purposed to integrate battery, PV, and load and supervise the optimal power flow between input and output ports.

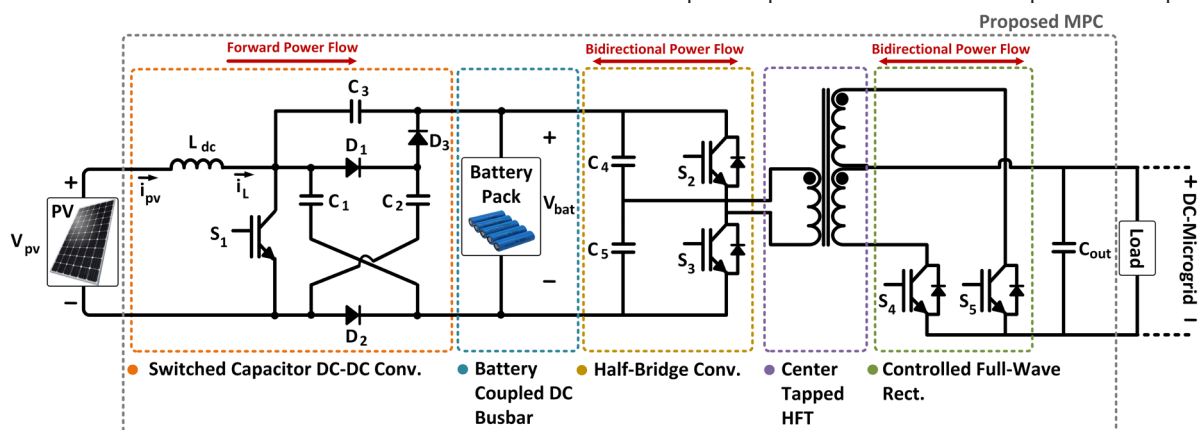


Figure 1. Circuit design of the proposed MPC

The switched-capacitor DC-DC converter is used to transfer power from PV to the battery/load with high efficiency. Besides, the related DC-DC converter makes it possible to connect low voltage PV into a relatively high voltage battery due to its high voltage conversion ratio capability. Half-bridge converter allows bidirectional power flow by transferring power from input ports to the output port and from the output port to the battery. While the half-bridge converter operates as an inverter during forward power flow, it operates as an uncontrolled full-wave rectifier during reverse power flow. The galvanic isolation between the input and output ports is provided by HFT with low turns ratio. The controlled full wave rectifier located on the secondary side, on the contrary to the half-bridge converter, operates as an uncontrolled full-wave rectifier during the forward power flow and operates as an inverter during reverse power flow.

The proposed MPC integrates three different converters; (i) the switched-capacitor DC-DC converter, (ii) the half-bridge converter, and (iii) the controlled full-wave rectifier via battery coupled common DC busbar and HFT. On the primary side, while the battery operates as a common DC bus, the switched-capacitor DC-DC converter performs the maximum power point tracking, constant current (CC), and constant voltage (CV) charging methods. The DC-busbar of the half-bridge converter is fed by PV and buffered by battery. Thus, uninterrupted power transfer to the load is provided. The relationship between the PV and battery voltages is computed using the duty cycle of S_1 . It is expressed as follows [24, 25];

$$Gain = \frac{V_{bat}}{V_{pv}} = \frac{2}{1-D} \tag{1}$$

where V_{bat} and V_{pv} represent the battery voltage and PV output voltage, respectively. D describes the duty cycle of switch S_1 and varies between 0-1 considering operation conditions of the system.

7. CONTROL SCHEME OF THE PROPOSED CONVERTER

The detailed control structure is shown in Figure 2. The main aims of the overall controller scheme are: (i) to ensure the continuity of the power transfer to the load with constant DC-link voltage, (ii) to transfer excessive power produced by PV to the battery, (iii) to provide bidirectional power flow between the ports. The effective control structure for the proposed MPC is a multi-loop control structure that is composed of power flow management, MPPT, CC/CV charging, and DC-link control. The system operates adaptively and allows instantaneous switching between the control loops.

The optimal power flow between input energy units and the output load with respect to the instantaneous PV generation, charge characteristics of the battery, and load variations are the main part of the proposed converter operation. According to the instantaneous states of the ports, there are three possible power flow circumstances as mode1, mode 2, and mode 3. Mode 1 corresponds to power transfer towards

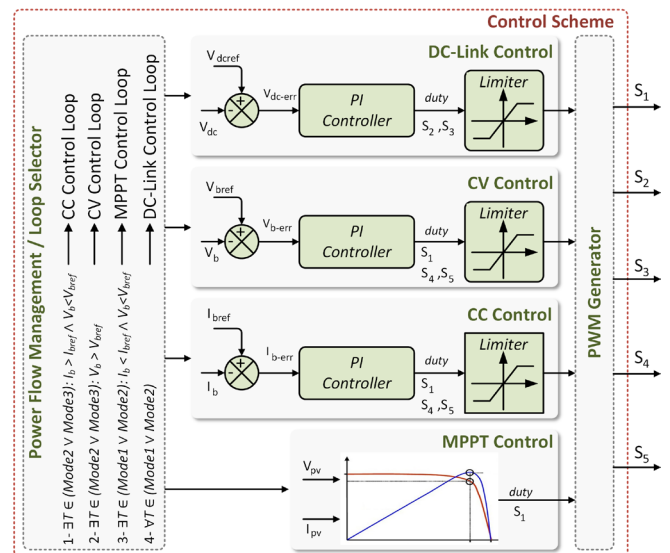


Figure 2. Control scheme of the proposed MPC

the load via PV and battery. In this mode, the battery operates in discharging mode. In mode 2, PV feeds the load, whereas the battery is charged via PV. Mode 3 represents the reverse power flow that is towards from the load side to the battery. In this mode, the battery operates in charging mode.

In mode 1, the power of the load is provided from the PV and battery at the same time. There are two potential circumstances in this case. The primary condition may take place when the load power consumption is higher than the available PV power. In this time interval, the battery buffers the PV to transfer uninterrupted power to the load. The secondary condition is that the PV operates under rated power due to environmental situations such as irradiation reduction (i.e. the generated power of PV decreases with irradiation reduction). The analytical relationship between power flows is given in Eq (2).

$$\int_{t_0}^{t_1} P_{load}(t) dt = \int_{t_0}^{t_1} P_{pv}(t) dt + \int_{t_0}^{t_1} P_{bat}(t) dt \tag{2}$$

In mode 2, the PV supplies battery, and the load, namely the power produced by PV feeds the load and charges the battery at the same time. This situation may occur under low load consumption ratings. The PV power could be decreased when the low power is consumed. However, in cases where the PV generation is insufficient to supply the load, the battery must be charged to keep the DC-link voltage constant by buffering the PV. In cases where the battery state of charge is less than 100%, the excessive power of the PV is used to charge the battery. During this time interval, power flows are expressed mathematically in Eq (3).

$$\int_{t_1}^{t_2} P_{load}(t) dt = \int_{t_1}^{t_2} P_{pv}(t) dt - \int_{t_1}^{t_2} P_{bat}(t) dt \tag{3}$$

In mode 3, the battery is charged from the load side. This case may occur under a condition where there is no solar irradiation and the battery is charged by the DC-microgrid to which the load is connected. By this way, the power flowing through the PV is zero. The power flow for this state is expressed as below:

$$\int_{t_2}^{t_3} P_{load}(t) dt = \int_{t_2}^{t_3} P_{bat}(t) dt \quad \& \quad \int_{t_2}^{t_3} P_{pv}(t) dt = 0 \quad (4)$$

The power transfer towards the load is performed using the DC-link control loop continuously, while the latter control loops are enabled considering the instantaneous power production value of PV. The power transfer from the load side to the battery is performed using CC/CV charging algorithms. The common aspect of the aforementioned control loops is the use of the pulse width modulation (PWM) method. The duty cycle values of the switches regulate the power flow rating by adjusting the voltages of output DC-link and battery coupled DC busbar.

The DC-link control loop is used to regulate the output DC-link voltage by triggering S_2 and S_3 switching devices. The duty cycles of switches S_2 and S_3 with a 180° phase shift between each other varies within the limits of 0-50%. A duty cycle of more than 50% causes the relevant switches to open simultaneously and short circuit. The duty cycles of the switches are computed using a PI controller. The difference between the reference (V_{dcref}) and actual voltages (V_{dc}) of the output load is applied to the PI controller.

The MPPT control loop is activated during mode 1 and some states of mode 2. The MPPT control loop is used to extract maximum power from PV by triggering the S_1 switching device. The maximum power tracking is performed by the perturb and observe (P&O) MPPT method due to the ease of operation and reduced computational load. The controller monitors the output voltage (V_{pv}) and current (I_{pv}) of PV and computes the instantaneous available power. The algorithm perturbs the operating voltage to ensure maximum power by adjusting the duty cycle of switch S_1 . The operating voltage perturbation is performed by computing the instantaneous duty cycle of S_1 switch as follows;

$$D_{new} = D_{old} + \Delta D \quad (if \ P > P_{old}) \quad (5)$$

$$D_{new} = D_{old} - \Delta D \quad (if \ P < P_{old}) \quad (6)$$

$$D_{new} = D_{old} \quad (if \ P = P_{old}) \quad (7)$$

The available excessive power of PV is crucial in enabling one of the MPPT or CC control loops. The battery charging scenario has great importance to improve the service life of the battery. Therefore, the battery charge current is frequently is restricted with $0.5 C$ (C represents the nominal capacity of the battery) charging current. Considering the charging current limits of the battery, the related control

loops are enabled. If the battery charge current reaches the charge current limit, the MPPT control loop switches to the CC control loop. The CC control loop rises the battery voltage to its reference value of 242 V. The CV control is enabled following the completion of the described operation of the CC loop. The CV charging continuous until the charging current gradually decreases to $0.05C$. The CC/CV charging is achieved by adjusting the duty cycle of the switch S_1 . In addition, the CC/CV control loops are also enabled in mode 3, which is another power transfer state towards to battery. The duty cycle value of the S_1 switch is computed using PI controllers during related control loops are enabled. The CC control loop computes the duty cycle by using the error value between the reference (I_{bref}) and actual (I_b) values of the battery current while the CV control loop computes the duty cycle by using the error value between the reference (V_{bref}) and actual (V_b) values of the battery voltage.

8. PERFORMANCE ANALYSIS

In this section, to verify the effectiveness and viability of the proposed MPC and the controller, a 3 kW proof-of-concept model which consists of 3 kW PV and 220 V 12 Ah battery has been developed using MATLAB/Simulink. The parameters of the simulation model are shown in Table 1. The performance of the proposed system is tested under two case studies including all modes of operations. The case studies which are summarized in Table 2 are formed by varying the irradiation of PV and loading.

Table 1. Parameters of the proposed MPC

| System | Parameters | Value |
|--------------------|---|---------|
| PV | PV maximum power (1000W/m ²) | 3197 W |
| | Maximum Power Point Voltage (1000W/m ²) | 87 V |
| | Maximum Power Point Current (1000W/m ²) | 36.75 A |
| | PV maximum power (250W/m ²) | 801.3 W |
| | Maximum Power Point Voltage (250W/m ²) | 86.9 V |
| | Maximum Power Point Current (250W/m ²) | 9.221A |
| Battery | Battery Capacity | 12 Ah |
| | Battery Nominal Voltage | 220 V |
| | Battery Maximum Charge Current | 6 A |
| Switched Capacitor | Inductor (L_{dc}) | 1 mH |
| | Capacitor (C_1) | 250 uF |
| | Capacitor (C_2) | 250 uF |
| | Capacitor (C_3) | 500 uF |
| General | Half Bridge Capacitors (C_4, C_5) | 2 mF |
| | DC-Link Capacitor (C_{out}) | 1 mF |
| | Nominal DC-Link Voltage | 200 |
| | Switching Frequency | 20 kHz |
| | HFT Turns Ratio | 1:2:2 |

Table 2. Details of case studies

| | Case 1 | | | | Case 2 | |
|--------------------------|----------------------|----------------------|-----------------------|-----------------------|-------------|-------------|
| | Time Intervals | | | Time Intervals | | |
| Time | 0-0.25 s | 0.25-0.5 s | 0.5-0.75 s | 0.75-1 s | 0-0.25 s | 0.25-0.5 s |
| Irradiation | 300 W/m ² | 650 W/m ² | 1000 W/m ² | 1000 W/m ² | - | - |
| Celsius | 25 C° | 25 C° | 25 C° | 25 C° | - | - |
| DC-Link Demand | 1500 W | 1500 W | 1500 W | 1500 W | -2000 W | -2000 W |
| Battery Charge/Discharge | Discharge | Charge | Charge (CC) | Charge (CV) | Charge (CC) | Charge (CV) |
| Mode | Mode 1 | Mode 2 | Mode 2 | Mode 2 | Mode 3 | Mode 3 |

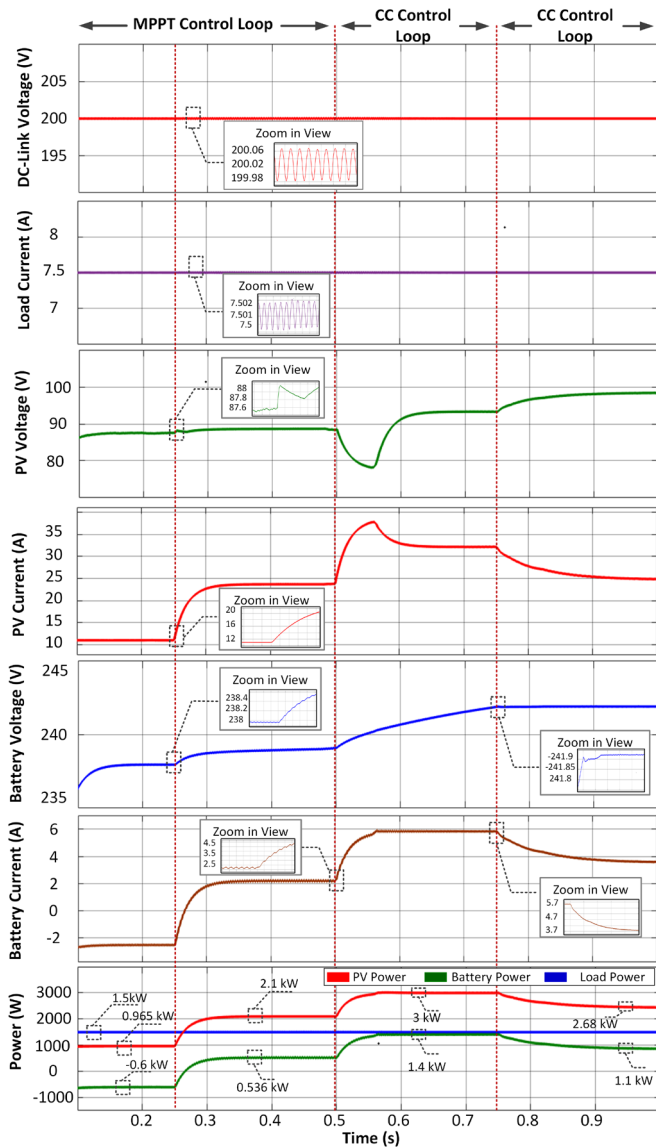


Figure 3. Performance results for case 1

The first case includes operating conditions in which mode 1, mode 2, and all control loops (MPPT, CC, CV, DC-link) are active, as well as the state responses of the transitions between these modes and loops. The different time intervals correspond to different operation modes and active control loops. Figure 3 shows the steady-state and dynamic responses of the proposed system during loop and mode transitions. It can be seen from the results that when the instantaneous power value of PV is lower than the load demand, the battery buffers and provides uninterrupted power to load. Following the raise in irradiation, the battery switches to charging in parallel with the increase in instantaneous power value of PV. During the state that the PV has relatively low output power, the MPPT control loop regulates the power flow from PV and the battery is charged with excessive power. However, in the case of high power generation from PV, the CC control loop is activated and the battery current is restricted. Following the battery voltage reaches a certain value, the CV control loop begins and keeps the output voltage of PV at a certain value. It is seen that the power of PV is increased to 1 kW, 2 kW, and 3 kW with the

raise in irradiation, while the battery is first discharged and then charged to the maximum voltage value.

The second case represents mode 3 operation in which the battery is charged by the DC microgrid. Figure 4 shows the steady-state and dynamic responses of the proposed converter during reverse power flow conditions. In this case study, the battery is charged with a constant current during the time interval of 0-0.5 s. The charge current of the battery is adjusted by the CC control loop. The CC charging is followed by CV charging during the time interval of 0.5-1 s.

The performance waveforms highlight that the proposed MPC and controller smoothly regulates the steady-state and transient power-sharing during different irradiation and loading variations. Besides, the efficiency of the proposed converter has been also evaluated. As can be seen from Figure 3-4, the efficiency values considering the operating modes are 96%, 96.8%, and 90%, respectively. The efficiency values of the proposed converter show its effectiveness under all possible power flow conditions.

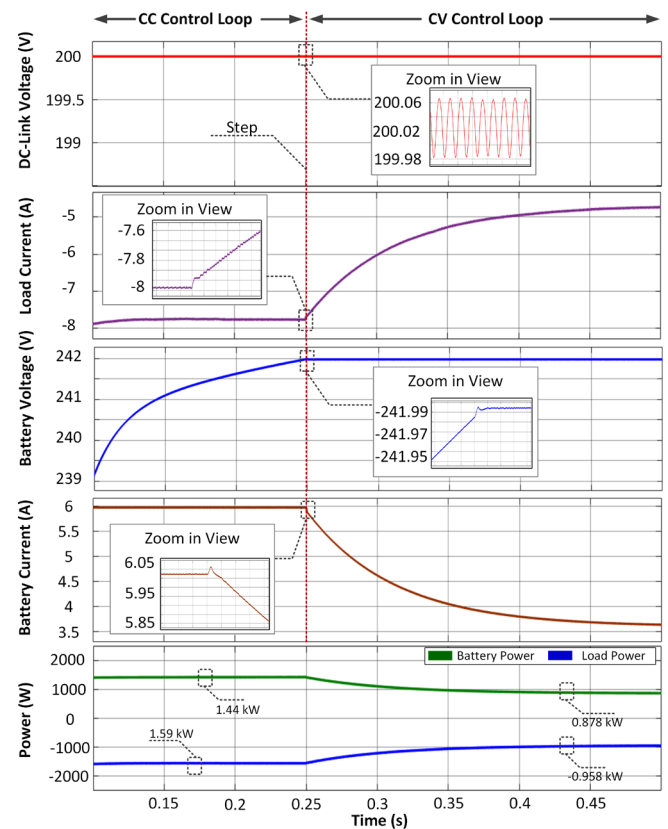


Figure 4. Performance results for case 2

9. CONCLUSION AND DISCUSSION

This study proposes a novel isolated bidirectional multi-port converter (MPC) based on a switched-capacitor converter and a half-bridge converter with an effective control scheme. The main advantages of the proposed converter are as follows: (i) low voltage PV integration with high voltage gain and high-efficiency switched-capacitor DC-DC converter, (ii) battery integration without an additional converter, (iii) reduced switch topology, (iv) cost-effectiveness (v) bidirectional power flow capability. The effectiveness of the propo-

sed MPC is evaluated under various operating conditions. The results show that the proposed MPC performs all the aforementioned functionalities. In addition to its satisfactory performance under steady-state conditions, it provides effective power transfer with smooth transitions between control loops during transient conditions.

REFERENCES

- [1] Das, M., Agarwal, V. (2016). Design and Analysis of a High-Efficiency DC-DC Converter With Soft Switching Capability for Renewable Energy Applications Requiring High Voltage Gain. *IEEE Transactions on Industrial Electronics*, 63: 2936-2944. doi:10.1109/TIE.2016.2515565.
- [2] Shen, D., Lim, C.-C., Shi, P. (2020). Robust fuzzy model predictive control for energy management systems in fuel cell vehicles. *Control Engineering Practice*, 98: 1-12. doi: 10.1016/j.conengprac.2020.104364.
- [3] Naidu, B. R., Panda, G., Siano, P. (2018). A Self-Reliant DC Microgrid: Sizing, Control, Adaptive Dynamic Power Management, and Experimental Analysis. *IEEE Transactions on Industrial Informatics*, 14: 3300-3313. doi: 10.1109/TII.2017.2780193.
- [4] Gangatharan, S., Rengasamy, M., Elavarasan, R. M., Das, N., Hossain, E., Sundaram, V. M. (2020). A Novel Battery Supported Energy Management System for the Effective Handling of Feeble Power in Hybrid Microgrid Environment. *IEEE Access*, 8: 217391-217415. doi: 10.1109/ACCESS.2020.3039403.
- [5] Prabhakaran P., Agarwal, V. (2020). Novel Four-Port DC-DC Converter for Interfacing Solar PV-Fuel Cell Hybrid Sources With Low-Voltage Bipolar DC Microgrids. *IEEE Journal of Emerging and Selected Topics in Power Electronics*, 8: 1330-1340. doi: 10.1109/JESTPE.2018.2885613.
- [6] Jiang, J., Gao, L., Jin, J., Luan, T. H., Yu, S., Xiang, Y. (2019). Sustainability Analysis for Fog Nodes With Renewable Energy Supplies. *IEEE Internet of Things Journal*, 6: 6725-6735. doi: 10.1109/JIOT.2019.2910875.
- [7] Savrun M. M., Atay, A. (2020). Multiport bidirectional DC-DC converter for PV powered electric vehicle equipped with battery and supercapacitor. *IET Power Electronics*, 13:3931-3939. doi: 10.1049/iet-pel.2020.0759.
- [8] Savrun M. M., Inci, M. (2021). Adaptive neuro-fuzzy inference system combined with genetic algorithm to improve power extraction capability in fuel cell applications. *Journal of Cleaner Production*, 299:1-11. doi: 10.1016/j.jclepro.2021.126944.
- [9] Sefa, I., Altin, N., Ozdemir, S., Kaplan, O. (2015). Fuzzy PI controlled inverter for grid interactive renewable energy systems. *IET Renewable Power Generation*, 9: 729-738. doi: 10.1049/iet-rpg.2014.0404.
- [10] Vettuparambil, A., Chatterjee, K., Fernandes, B. G. (2021). A Multiport Converter Interfacing Solar Photovoltaic Modules and Energy Storage With DC Microgrid. *IEEE Transactions on Industrial Electronics*, 68: 3113-3123. doi: 10.1109/TIE.2020.2978709.
- [11] Zhang, N., Sutanto, D., Muttaqi, K. M. (2016). A review of topologies of three-port DC-DC converters for the integration of renewable energy and energy storage system. *Renewable and Sustainable Energy Reviews*, 56: 388-401. doi: 10.1016/j.rser.2015.11.079.
- [12] Bhattacharjee, A. K., Kutkut, N., Batarseh, I. (2019). Review of Multiport Converters for Solar and Energy Storage Integration. *IEEE Transactions on Power Electronics*, 34: 1431-1445. doi: 10.1109/TPEL.2018.2830788.
- [13] Khosrorji, S., Ahmadian, M., Torkaman, H., Soori, S. (2016). Multi-input DC/DC converters in connection with distributed generation units – A review. *Renewable and Sustainable Energy Reviews*, 66: 360-379. doi: 10.1016/j.rser.2016.07.023.
- [14] Chaudhury T., Kastha, D. (2020). A High Gain Multiport DC-DC Converter for Integrating Energy Storage Devices to DC Microgrid. *IEEE Transactions on Power Electronics*, 35:10501-10514. doi: 10.1109/TPEL.2020.2977909.
- [15] Savrun, M. M., Koroğlu, T., Tan, A., Cuma, M. U., Bayindir, K. Ç., Tümay, M. (2020). Isolated H-bridge DC-DC converter integrated transformerless DVR for power quality improvement. *IET Power Electronics*, 13: 920-926. doi: 10.1049/iet-pel.2019.0687
- [16] Chakraborty S., Chattopadhyay, S. (2017). Minimum-RMS-Current Operation of Asymmetric Dual Active Half-Bridge Converters With and Without ZVS. *IEEE Transactions on Power Electronics*, 32: 5132-5145. doi: 10.1109/TPEL.2016.2613874.
- [17] Forouzesh, M., Siwakoti, Y. P., Gorji, S. A., Blaabjerg, F., Lehman, B. (2017). Step-Up DC-DC Converters: A Comprehensive Review of Voltage-Boosting Techniques, Topologies, and Applications. *IEEE Transactions on Power Electronics*, 32: 9143-9178. doi: 10.1109/TPEL.2017.2652318.
- [18] Wu, H., Zhang, J., Qin, X., Mu, T., Xing, Y. (2016). Secondary-Side-Regulated Soft-Switching Full-Bridge Three-Port Converter Based on Bridgeless Boost Rectifier and Bidirectional Converter for Multiple Energy Interface. *IEEE Transactions on Power Electronics*, 31: 4847-4860. doi: 10.1109/TPEL.2015.2473002.
- [19] Saadi, R., Hammoudi, M. Y., Kraa, O., Ayad, M. Y., Bahri, M. (2020). A robust control of a 4-leg floating interleaved boost converter for fuel cell electric vehicle application. *Mathematics and Computers in Simulation*, 167: 32-47. doi: 10.1016/j.matcom.2019.09.014.
- [20] Thounthong P., Davat, B. (2010). Study of a multiphase interleaved step-up converter for fuel cell high power applications. *Energy Conversion and Management*, 51: 826-832. doi: 10.1016/j.enconman.2009.11.018.
- [21] Bi, H., Wang, P., Che, Y. (2019). A Capacitor Clamped H-Type Boost DC-DC Converter With Wide Voltage-Gain Range for Fuel Cell Vehicles. *IEEE Transactions on Vehicular Technology*, 68: 276-290. doi: 10.1109/TVT.2018.2884890.
- [22] Kapat, S., Patra, A., Banerjee, S. (2009). A Current-Controlled Tristate Boost Converter With Improved Performance Through RHP Zero Elimination. *IEEE Transactions on Power Electronics*, 24: 776-786. doi: 10.1109/TPEL.2008.2008994.
- [23] Tang, Y., Fu, D., Wang, T., Xu, Z. (2015). Hybrid Switched-Inductor Converters for High Step-Up Conversion. *IEEE Transactions on Industrial Electronics*, 62: 1480-1490. doi: 10.1109/TIE.2014.2364797.
- [24] Ismail, E. H., Al-Saffar, M. A., Sabzali, A. J. (2008). High Conversion Ratio DC-DC Converters With Reduced Switch Stress. *IEEE Transactions on Circuits and Systems I: Regular Papers*, 55: 2139-2151. doi: 10.1109/TCSI.2008.918195.
- [25] İnci, M., Büyük, M., Savrun, M. M., Demir, M. H. (2021). Design and analysis of fuel cell vehicle-to-grid (FCV2G) system with high voltage conversion interface for sustainable energy production. *Sustainable Cities and Society*, 67: 1-12. doi: 10.1016/j.scs.2021.102753.



Effect of Fabric Structural Parameters on Various Comfort Properties of Automobile Seat Cover Fabrics

Mine Akgun^{1*} , Hayrünnisa Aydan Kamacı² 

^{1,2}Bursa Uludag University, Faculty of Engineering, Textile Engineering Department, Bursa, Turkey

Abstract

In this study, the effects of the structural parameters forming automobile seat cover fabrics on the comfort properties (such as water vapor permeability, air permeability, and thermal resistance properties of fabrics) that may affect the user's usage performance were examined. A special finishing process did not apply to the fabrics. It was aimed to evaluate the direct (without any special treatment) effect of the basic structural parameters that make up the fabric. Thus, it was considered that the fabrics used in the seat covers during the usage or after the treatments such as seat cleaning would create an important design input in terms of the breathability of the seat cover fabric and its sustainability throughout the lifetime of the car. As a result of this research, it was observed that thickness, weight per unit area, and weave structure of seat cover woven fabrics have an essential effect on the water vapor permeability, air permeability, and thermal resistivity properties.

Keywords: Automobile seat cover woven fabric, water vapor permeability, air permeability, thermal resistivity, comfort properties

10. INTRODUCTION

Besides the aesthetic and abrasion performance of the fabrics used in automobile seat cover, comfort features are also important. The breathability, permeability (air and water vapor permeability, etc.), and the fabric's thermal comfort properties to be used as seat cover are important for the sustainability of the face fabric's comfort properties used in the seat covers during use and after cleaning.

In determining the thermal comfort of seat cover fabrics used in the automotive industry, various parameters such as heat and moisture transfer, air permeability, thermal resistance, static electrical tendency, water vapor permeability, water absorbency should be taken into consideration in the design of seat cover fabrics. It is expected to have a fabric structure that minimizes sweating, especially in long-distance travel.

Automobile seat cover fabric structures are generally produced polyester, wool and wool/polyester mixture, polyamide, acrylic, leather structures [1]. Comfort in cars is closely related to the seat cover fabric structural properties and components of the seat that the user touches in the car [2]. High moisture transfer and air permeability increase comfort and decrease user fatigue [3]. For this reason, materials suitable for air, water vapor, and heat permeability are preferred in

seat cover fabric [4].

Factors affecting the thermal properties of textiles could be listed as follows [5,6]:

- thermal conductivity of fiber and air held in the fabric
- special heat of the fiber
- fabric thickness and number of layers
- volume density of the fabric (number, size, and distribution of air gaps in the fabric)
- fabric surface (type of fiber, structure of fabric, finishing processes in fabric)
- contact area between fabric and surface
- atmospheric conditions: temperature, relative humidity, movement of the surrounding air.

The thermal conductivity of the fabric structure depends on the number of air gaps in the fabric. The thermal conductivity of stagnant air is lower than that of all fibers. The ideal insulating material is stagnant air. Bulky materials are capable of holding excess air in them due to their structure. A high amount of air should be present in a textile material's inner structure with high thermal insulation. Fabric thickness is one of the most important factors determining the thermal and vapor conductivity of the structure. As the thickness of the material and therefore the amount of air it contains increases, the material's thermal and vapor resistance increa-

* Corresponding author
Email: akgunm@uludag.edu.tr



ses, and its permeability decreases [7,8].

The permeability of the fabrics depends on the raw material (such as fiber type, fineness, and cross-section, etc.), yarn properties (such as linear density, twist level, yarn hairiness, etc.), and fabric structural properties (such as geometrical properties, weave type, fabric thickness, porosity, etc.) as well as the finishing processes applied to those fabrics [9,10]. When the effect of fabric weave structure (considering the same density values and yarn type) on comfort properties was examined, it was observed that twill fabrics had higher air permeability, water vapor permeability, and heat resistance values compared to plain fabrics [11]. In fabrics with a knitted upper surface, it was found that the thickness value directly affects the water vapor permeability value, and the permeability decreases as the thickness increases [4].

Fabrics used as seat cover could be exposed to water and moisture effects (such as sweat, moisture, and cleaning, etc.) during usage. In this case, it was expected that the fabrics used as seat covers in terms of user comfort features had properties such as good water vapor and air permeability. These features are not only important in terms of user comfort but also affect automobile usage performance. It was expected that the seat cover fabric would dry out in a short time to prevent unwanted conditions such as smell, staining, and mold after cleaning or contact of the seat surfaces with liquid during usage. This situation was considered to be taken into account in terms of easy drying of seat cover fabrics with good air and water vapor permeability. For this purpose, it was aimed to evaluate the water vapor permeability, air permeability and thermal resistivity properties of automotive seat cover woven fabrics having with different structural parameters.

11. MATERIALS AND METHODS

11.1. Materials

In this study, 100 % polyester face woven fabrics were used.

A special finishing (coating etc.) process did not apply to the fabrics. The structural parameters of automotive seat cover fabrics were given in Table 1. Seat cover fabric samples and weave structures were presented in Figures 1 and 2, respectively.

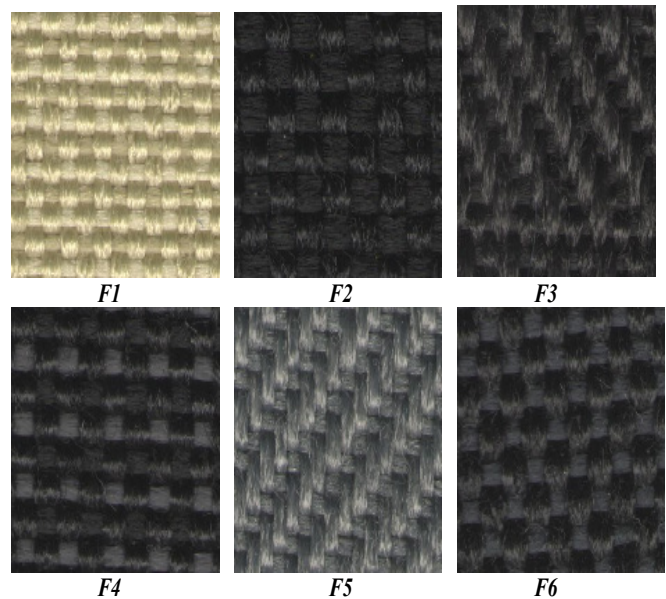


Figure 1. Images of seat cover fabric samples

F3 fabric had a dobby fabric pattern structure where twill 3/1 weave was dominant and basket 2/2 connections were formed in between.

11.2. Method

This study aimed to investigate the effect of fabric structural parameters on some comfort properties of the automotive seat cover woven fabrics. Fabric samples were conditioned at 65±2% relative humidity and 20±2°C for 24 hours by the ASTM D 1776-08 [12] standards before all mentioned tests.

Relative Water Vapor Permeability

Relative water vapor permeability is the ability of the fabric to transfer water vapor on a percentage scale. Among this

Table 1. Structural parameters of seat cover fabrics

| Fabric No | Yarn Count (Nm) | | Yarn Density (thread/cm) | | Fabric Thickness (mm) | Fabric Weight per Unit Area (g/m ²) | Weave |
|-----------|-----------------|------|--------------------------|------|-----------------------|---|--------------|
| | Warp | Weft | Warp | Weft | | | |
| F1 | 28 | 16 | 16 | 14 | 0.53 | 228.1 | Weft Rib 2/2 |
| F2 | 16 | 16 | 10 | 10 | 0.83 | 303.2 | Basket 3/2 |
| F3 | 12 | 12 | 16 | 14 | 0.94 | 310.1 | Dobby |
| F4 | 8 | 8 | 12 | 12 | 0.76 | 307.5 | Plain |
| F5 | 18 | 18 | 18 | 16 | 0.56 | 233.9 | Twill 3/1 |
| F6 | 12 | 12 | 12 | 10 | 0.78 | 324.4 | Weft Rib 2/2 |

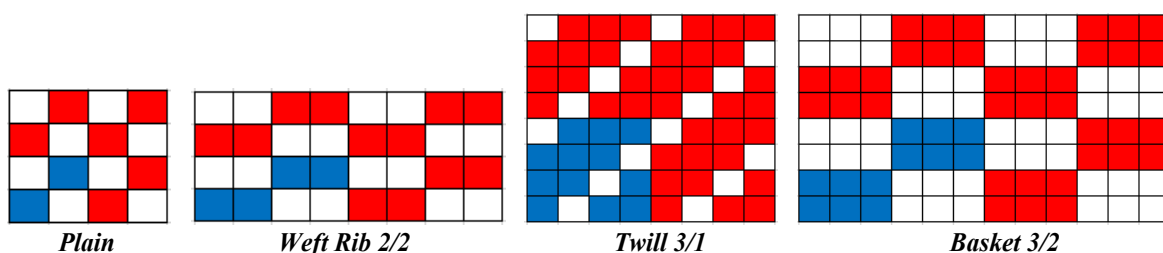


Figure 2. Weave structure of fabric samples

study, relative water vapor permeability was measured on ‘Permetest’ instrument according to EN ISO 11092 standard [13].

Air permeability

Air permeability of the fabrics was measured based on EN ISO 9237 [14] standard using SDL Atlas Digital Air Permeability Tester Model M 021A. Measurements were performed by application under 100 Pa air pressure per 25 cm² fabric surface.

Thermal Resistivity (r)

It is defined as the resistance of the structure against heat flow. Thermal resistance was measured by using Alambeta instrument. Thermal resistance is connected with fabric thickness and thermal conductivity coefficient by the Equation (1) [15].

$$r = \frac{h}{\lambda} \quad (m^2K / W) \quad (1)$$

where,

r: thermal resistance,

h: fabric thickness (m),

λ: thermal conductivity coefficient (W/mK)

12. RESULTS AND DISCUSSION

12.1. Analysis of the Water Vapor Permeability

Water vapor permeability values of the fabrics were given in Figure 3. In Fig.3, it was observed that the fabrics with low thickness and weight per unit area showed high water vapor permeability values. It was seen that the fabric thickness and weight values on the water vapor permeability of the fabrics were determinant according to the weave structure. Although F1 and F6 fabrics have the same weave structure, it was seen that the F1 fabric, which had a low thickness and weight, had a higher water vapor permeability value.

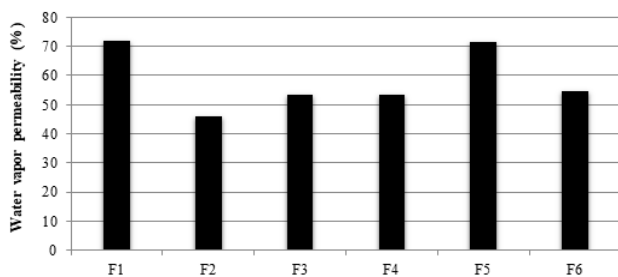


Figure 3. Water vapor permeability values of fabrics

12.2. 3.2 Analysis of the Air Permeability

In Fig. 4, air permeability values of the fabrics were given. When Figure 4 was examined, it was observed that the weave structure was a determining factor in the air permeability values of the fabrics. It was observed that plain and rib weave structures gave low air permeability values.

Higher air permeability values were obtained in weave structures (F2, F3, and F5) where the yarns made long floats. This was due to the increase in the air permeability between the yarns in the structures where the yarns have long floats.

When the weave structures of the fabrics were examined, it could be seen that the twill weave structure, such as F5, increased the air permeability value (Fig. 4). Similarly, it was seen that the regions with twill weave structure in the dobby pattern structure that forms the F3 fabric also increased the air permeability value. Besides, it was observed that high air permeability values were also obtained in the basket weave structure in which F2 fabric intersects by making long floats.

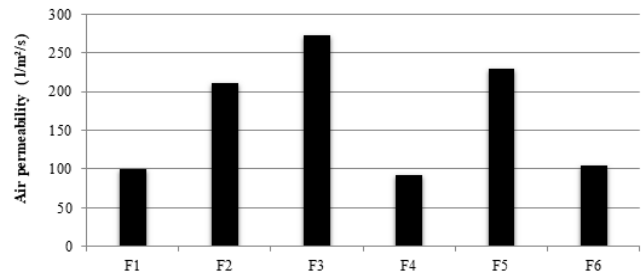


Figure 4. Air permeability values of fabrics

12.3. Analysis of the Thermal Resistivity

In Fig. 5, thermal resistivity values of the fabrics were given. In Fig. 5, it was observed that F1 and F5 fabric structures had lower thermal resistance values compared to other fabrics. It was observed that fabrics with low fabric thickness and weight per unit area values had lower thermal resistance values.

This result showed that the fabric thickness and weight values were more determinants of the fabrics' thermal resistance than the weave structure.

In the literature, it was stated that the parameters affecting fabric porosity affect the thermal transmittance of the fabric. It was stated that the parameter that most affects the thermal behavior of the fabric is the thickness of the fabric. An increase in fabric thickness affects fabric porosity by increasing fabric volume [16,17]. The high amount of stagnant air present in the structure in fabrics with high thickness values caused these structures to show high thermal resistance. Experimental results showed that the low amount of stagnant air present in the fabric structures with low thickness and weight per unit area values caused these structures to show low thermal resistance values.

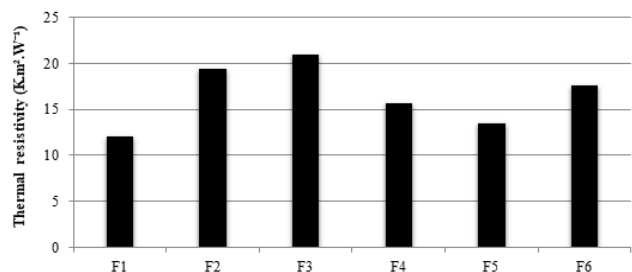


Figure 5. Thermal resistivity values of fabrics

13. CONCLUSION

In this study, the permeability and thermal resistance values of woven fabrics used in automobile seat cover woven fabrics were evaluated in terms of providing user and us-

age comfort. The effects of structural parameters forming the fabric on water vapor permeability, air permeability and thermal resistance values were investigated. A special finishing process did not apply to the fabrics and it was aimed to evaluate the natural effect of structural parameters in terms of high sustainable usage performance.

When the fabric structures used in automobile seat cover were evaluated in terms of user comfort, the breathability and hence permeability properties of the fabrics were expected to be high in terms of reducing user sweating. Similar expectations are important in terms of easy drying of seat cover fabrics wetted due to conditions such as cleaning or liquid spillage during use. Considering such usage expectations, fabric structures with high water vapor and air permeability should be preferred. In the experimental study, it was observed that fabrics with low thickness and weight per unit area values gave high water vapor permeability values. Experimental results showed that the weave structure was a determining factor in the air permeability values of fabrics. Higher air permeability values were obtained in weave structures where the yarns made long floats.

When the thermal resistance values of the fabrics used in the seat cover fabrics were evaluated, it was considered that it might be appropriate to prefer fabric structures that did not show high resistance to heat flow in terms of user comfort or usage comfort. Since the thermal conductivity of the materials with low thermal resistance was higher, it could easily transmit the user's body temperature, thus preventing sweating and providing comfort. Besides, since the car's interior temperature could easily balance the heat of the fabrics with low thermal resistance values, it would be ensured that the seat covers that get wet due to seat cleaning or external factors could be easily dried. In this case, the formations such as odor, stain, and moisture due to wetting would be prevented. It should be ensured that the heat did not keep within the fabric structure but that it could be transferred more easily, and thus it could be kept in balance with the surrounding temperature in a continuous manner. Therefore, automobile seat cover structures with low fabric thickness and weight values might be preferred in terms of showing low thermal resistance values.

5. REFERENCES

- [1] Fung, W., Hardcastle, M. (2001). *Textiles in Automotive Engineering*, Woodhead Publishing Limited, Cambridge, England.
- [2] Hoeval, B.T. (1999). *New Worldwide Trends in Automotive Textiles*. Technical Textiles, August, 42(37).
- [3] Powell, N.B. (2004). Design Driven: The Development of New Materials of Automotive Interiors. *Journal of Textile and Apparel, Technology and Management*, 3(4): 1-19.
- [4] Berber, R.Ö., Marmaralı, A., Ertekin, G. (2014). Otomobil Döşemeliklerinde Yüksek Isıl Konfor Sağlayacak Sünger ve Astar Özelliklerinin Belirlenmesi. XIII. Uluslararası İzmir Tekstil ve Hazır Giyim Sempozyumu, p.320-326.
- [5] Xiaoming, T. (2001). *Smart Fibres, Fabrics and Clothing*, 1st Edition, Woodhead Publishing, England.
- [6] Marmaralı, A., Kretzschmar, S.D., Özdil, N., Oğlakcioğlu, N.G. (2006). Parameters that Affect Thermal Comfort of Garment. *Tekstil ve Konfeksiyon*, 16(4): 241-246.
- [7] Havenith, G. (2002). Interaction of Clothing and Thermoregulation. *Exogenous Dermatology*, 1(5): 221-230. doi: 10.1159/000068802.
- [8] Özdil, N., Marmaralı, A., Kretzschmar, S. (2007). Effect of Yarn Properties on Thermal Comfort of Knitted Fabrics. In; *International Journal of Thermal Sciences*, 46(12):1318-1322. doi.org/10.1016/j.ijthermalsci.2006.12.002.
- [9] Öner, E. (2008). A Research about Comfort Properties of Woven Fabrics. Pamukkale University, Institute of Natural Applied Sciences, Textile Engineering Department, M.Sc. Thesis, 94 pages.
- [10] Yoon, H.N., Buckley, A. (1984). Thermal Transport of Textiles for Comfort. *Textile Research Journal*, 34(3): 54-58.
- [11] Kanat, Z.E. (2007). Farklı İpliklerden Dokunan Kumaşların Konfor Özelliklerinin Karşılaştırılması, Ege Üniversitesi, Mühendislik, Fakültesi, M. Sc. Thesis, 92 pages.
- [12] ASTM D1776, 2009, Standard Practice for Conditioning and Testing Textiles.
- [13] ISO 11092 Standard: 1993, Textiles Determination of physiological Properties-Measurement of thermal and water vapor resistance under steady-state conditions (sweating guarded-hotplate test).
- [14] EN ISO 9237, Textiles, determination of the permeability of fabrics to air, International Organization for Standardization, 1995, Geneva.
- [15] Frydrych, I., Dziworska, G., Bilska, J. (2002). Comparative Analysis of the Thermal Insulation Properties of fabrics made of Neutral and Man-Made Cellulose Fibres. In; *Fibres & Textiles in Eastern Europe*, October/December 2002: 40-44.
- [16] Das, A., Alagirusamy, R. (2010), *Science in Clothing Comfort*, Woodhead India, New Delhi, India.
- [17] Morgil, Y. (2015). Havlu Örme Çorapların Isıl Konfor Özellikleri, İstanbul Teknik Üniversitesi, Fen Bilimleri Enstitüsü, M. Sc. Thesis, 111 pages.



A preliminary Investigation of Surface Micro Modification Effects on the Biocompatibility of 316L Stainless Steel

Sıdıka Mine Toker¹ , Erdoğan Serhad Özbulut² , Zübeyir Kolçak³ , Esra Güner⁴ 

¹⁻⁴Eskişehir Osmangazi University (ESOGU), Metallurgical and Materials Engineering Department, Eskişehir, Turkey

Abstract

Effects of surface properties such as roughness and surface energy are critical for determining the biocompatibility of all types of biomaterials, as in the case of biomedical alloys. Recently, microstructure induced surface energy changes have started attracting attention in surface property related biocompatibility analysis of metals. The current study mainly aims to focus on the effects of surface micro modification on the biocompatibility of metallic biomaterials, in order to get an understanding of the underlying mechanisms that affect surface properties and biocompatibility. For this purpose, a preliminary biocompatibility analysis was conducted on a conventional biomedical alloy; 316L stainless steel, whose surface was modified by forming micro-deformation areas of different patterns. The results of this study indicated that, in addition to surface roughness, micro-deformation pattern characteristics are also very critical parameters in terms of determining cellular response.

Keywords: Biomedical alloys, microstructure, biocompatibility, surface, micro-deformation.

14. INTRODUCTION

Metallic biomaterials are widely used for biomedical purposes such as orthopedic implants, dental applications or cardiovascular devices. The main reason biomedical alloys are preferred for these applications despite the development of lighter and advanced materials is their mechanical properties [1,2]. Especially for orthopedic applications such as hip and knee implants, the mechanical durability and the ability to easily tailor mechanical properties of metals through altering their microstructure provide an important advantage for metallic biomaterials over other alternatives [1,2]. However, due to issues such as potential corrosion, toxic ion release, bacterial layer formation as well as mechanical mismatch with surrounding tissue or insufficient biomechanical fixation, their biocompatibility is yet to be improved [1-4].

For biocompatibility, as in all types of materials, material surface is of utmost importance for metals as well, as the first biomaterial-tissue interaction takes place at the surface [5,6]. Surface properties such as roughness, topographical features, wettability and surface energy are the important surface related parameters which determine initial biocompatibility response in terms of biomechanical fixation, osseointegration, corrosion and ion release [5-7]. Among these parameters, the effect of surface roughness is more commonly investigated in relation with surface energy [8,9]. As

opposed to the general understanding that increased surface roughness is expected to also increase cellular attachment due to increased surface energy, recent studies have shown that organization of the topographical features on the surface may more effectively determine cell response [8-12]

Moreover, some of the recent studies have started exploring the effect of microstructural properties of metallic materials on their biocompatibility [7, 10-12]. Commonly, effects of microstructural mechanisms on the material properties of metallic materials are usually explored with a focus on mechanical properties and deformation behavior. However, recent studies have shown that, microstructural properties of metallic materials can also be critical for determining their biocompatibility at different levels [7, 10-12]. For instance, ex situ biocompatibility was observed to be influenced by the presence of dislocations through localization of oxide particles around dislocation networks, which may affect ion release [7]. Surface topography and surface energy were also shown to be affected by microstructure at the micro and nanoscale, which in turn influenced cell attachment and proliferation behavior [10-12].

With this motivation, the current study aims to get a preliminary understanding of the effect of surface micro modification on the biocompatibility of metallic biomaterials. For this purpose, a conventional biomedical alloy; 316L stainless steel was investigated by forming controlled micro-defor-

* Corresponding author
Email: stoker@ogu.edu.tr



mation areas on the sample surfaces and the effect of each micro-deformation area on cell attachment was examined.

15. MATERIALS AND METHODS

The 316L steel samples, for which the chemical composition is given in Table 1, were cut in pieces of 3mm height from a 5mm radius cylindrical rod. The surfaces of each sample were then prepared for surface micro deformation via grinding and polishing.

Controlled micro-deformation areas with different patterns of micro-indentations were formed on 316L stainless steel samples by using a Vickers micro hardness testing device. Details of the formed micro-deformation areas in terms of the applied load, formed indent size and the length of the spacings between indent centers are given in Table 2. A control sample without any micro-deformation areas was also investigated for comparison, which is referred to as the 'reference' sample. The obtained surfaces were examined with

Hitachi Regulus 8230 Field Emission Scanning Electron Microscope (FESEM) and surface roughness measurements were performed with a Mitutoyo mechanical contact needle profilometer.

Table 2. Properties of the micro-deformation areas formed on 316L sample surface.

| Sample | Applied load and exposure period | Average indent size (µm) | Average spacing between indent centers (µm) |
|-----------|----------------------------------|--------------------------|---|
| Reference | - | - | - |
| 1 | 1KgF, 5 Seconds | 80 | 100 |
| 2 | 1KgF, 5 Seconds | 80 | 200 |
| 3 | 0.5KgF, 5 Seconds | 60 | 100 |
| 4 | 0.5KgF, 5 Seconds | 60 | 200 |

For the *in vitro* tests, Saos-2 cells (osteosarcoma cell line) were seeded on the reference sample surface and on the the micro-deformation areas of the patterned samples with a density of 5000 cells per sample. Cells were fixated on the sample surfaces with the use of a glutaraldehyde agent, fol-

Table 1. Chemical composition of the investigated 316L stainless steel in weight percent.

| Element | Fe | C | Mn | P | S | Cr | Ni | Mo | Cu | Si | N |
|--------------------|---------|-------|------|-------|-------|-------|-------|------|------|------|------|
| Weight percent (%) | Balance | 0,027 | 1,76 | 0,042 | 0,029 | 16,80 | 10,12 | 2,12 | 0,38 | 0,27 | 0,08 |

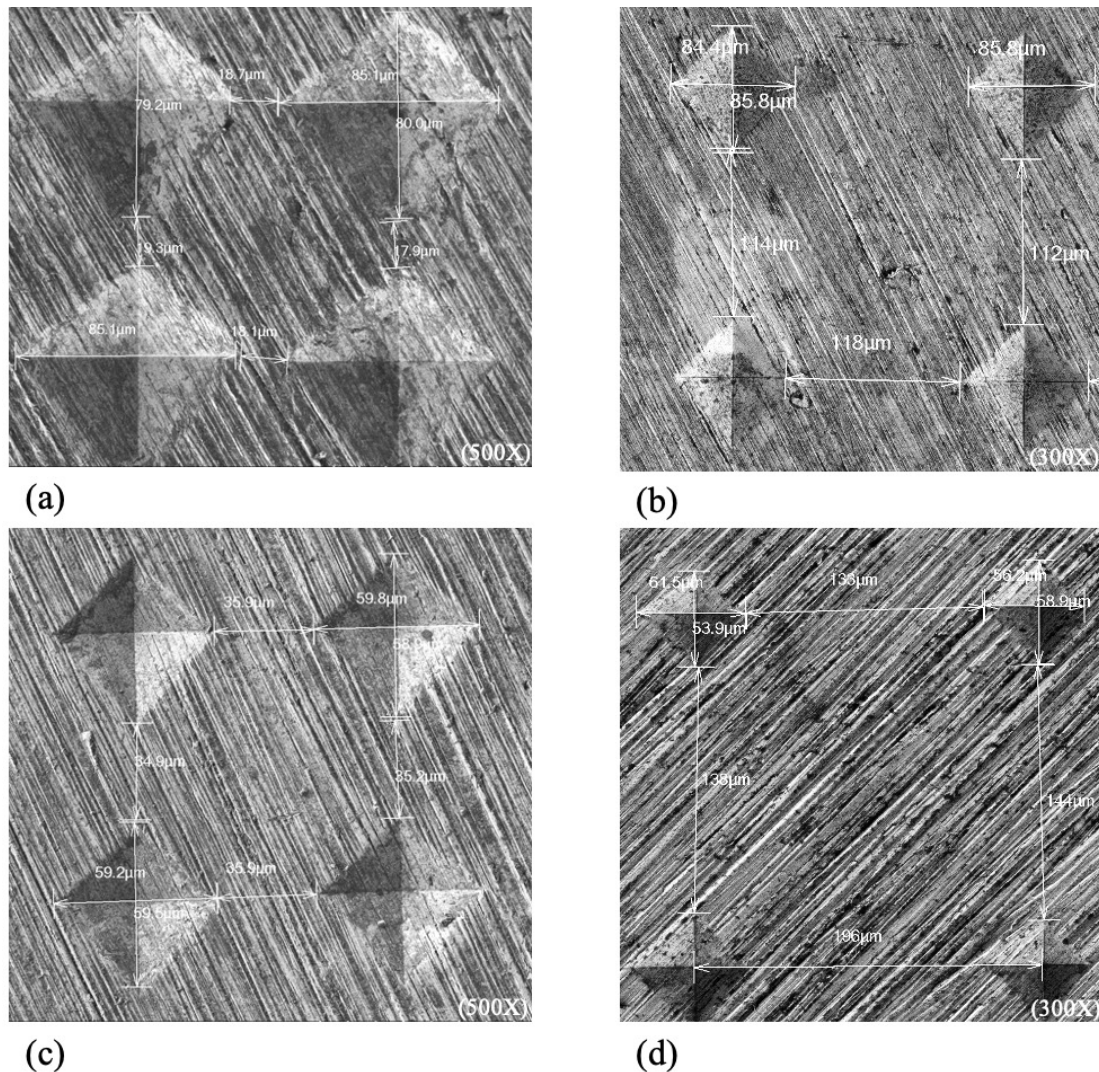


Figure 1. FESEM images from the initial microstructural characterization of the micro-deformation areas of; (a) Sample-1, (b) Sample-2, (c) Sample-3, (d) Sample-4.

lowing incubation periods of 5 and 10 days. Cell morphologies were then examined in detail via FESEM. With the use of the FESEM images, cell count on each micro-deformation area was performed and converted to number of cells per millimeter square (mm^2) area for comparison.

16. RESULTS AND DISCUSSION

Initial structural characterizations of the formed micro-deformation areas of the four patterned sample surfaces were performed via FESEM (Figure 1). These initial examinations evidenced that the indentation size and spacings were formed as planned and no unexpected structural irregularities were observed within or around the micro-deformation areas (Figure 1).

The results of the surface profilometry analysis of the formed patterns and the reference sample surface listing the average surface roughness (Ra) and the maximum depth (Rz) created by the indentations for each pattern are given in Table 3. (Since no indentations were formed on the reference sample, Rz value was not measured for this sample.)

Table 3. Results of surface profilometry analysis

| Sample | Average Ra (μm) | Maximum Rz (μm) |
|-----------|------------------------------|------------------------------|
| Reference | 0.32 | - |
| 1 | 1.19 | 9.96 |
| 2 | 0.99 | 9.74 |
| 3 | 0.79 | 7.37 |
| 4 | 0.49 | 5.81 |

The surface profilometry analysis results revealed all of the micro-deformation areas exhibit much higher average roughness values as compared to the reference sample. Moreover, comparing the deformed sample surfaces with each other, it was observed that average surface roughness increases with increasing indent size and the application of a larger amount of load results in deeper indents which translate to higher Rz values as observed in samples 1 and 2 in comparison to samples 3 and 4. On the other hand, comparing the effect of spacing length between the indentations, it can be argued that roughness increases as the space between indentation centers decrease, which can be observed for samples 1 and 3 as compared to samples 2 and 4.

In order to get an understanding of the effects of varying surface properties on cell attachment behavior as a function of time, the Saos-2 cells fixated on each sample were observed in detail via FESEM following incubation periods of 5 and 10 days. The cells localized on the patterned area were investigated at different magnifications, where the overall cellular behavior on the whole micro-deformation area (Figure 2 and Figure 4) and on individual indents (Figure 3 and Figure 5) were examined in detail. The cell attachment behavior on the reference sample surfaces following incubation periods of 5 and 10 days were also investigated and are given in Figure 6.

Comparing the micro-deformation areas to the reference surface, it was observed that all the samples with surface

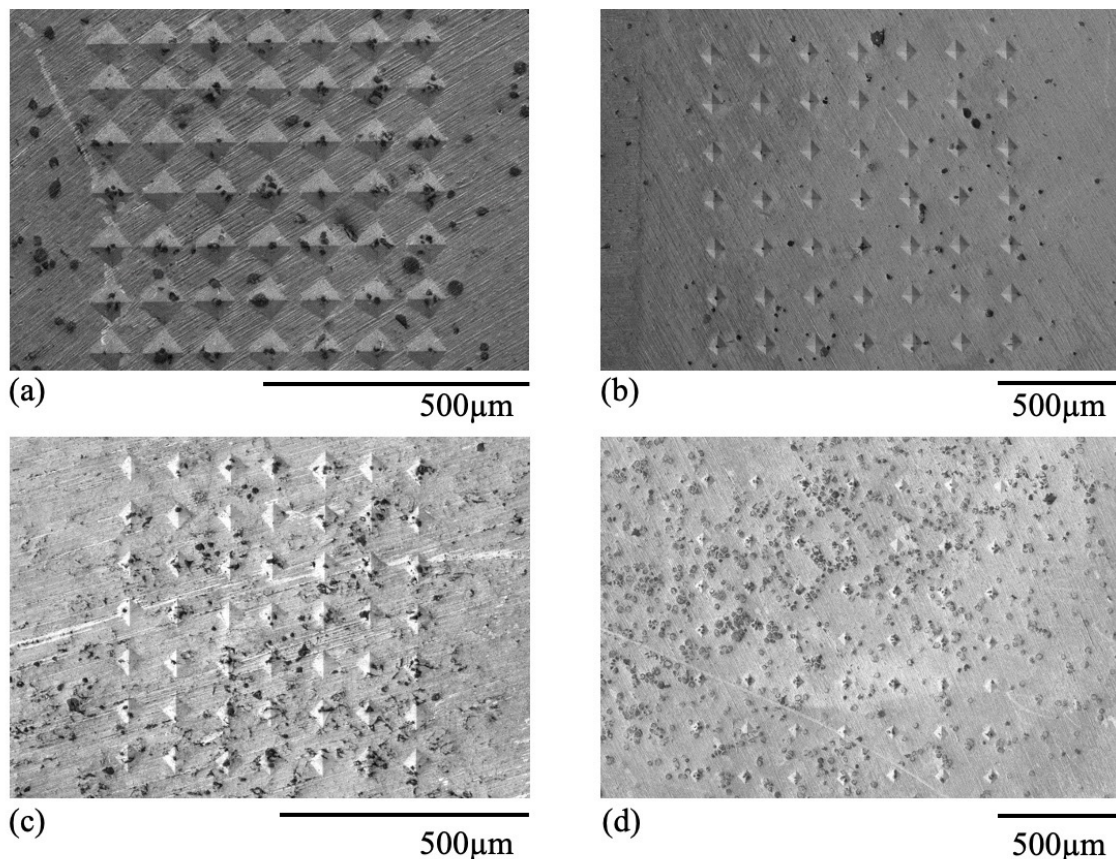


Figure 2. FESEM images of the Saos-2 cells fixated on the overall micro-deformation areas of (a) Sample-1, (b) Sample-2, (c) Sample-3, (d) Sample-4; following 5 days of incubation.

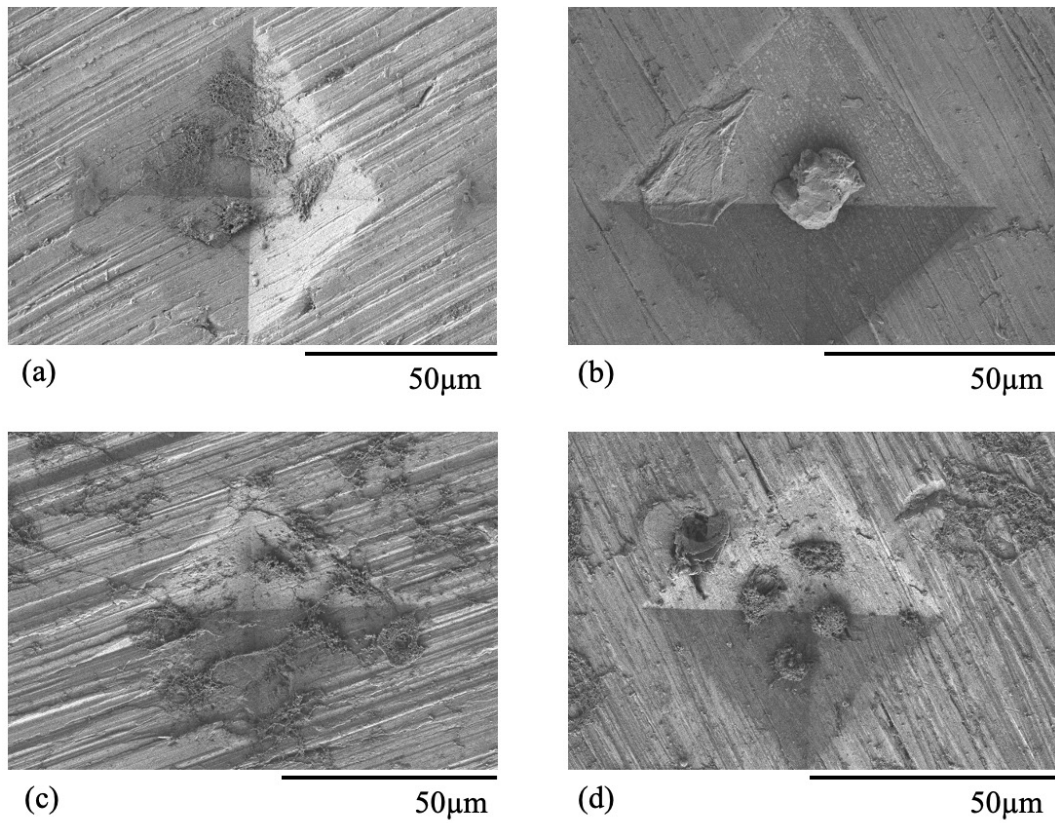


Figure 3. FESEM images of the Saos-2 cells around individual indents of (a) Sample-1, (b) Sample-2, (c) Sample-3, (d) Sample-4; following 5 days of incubation.

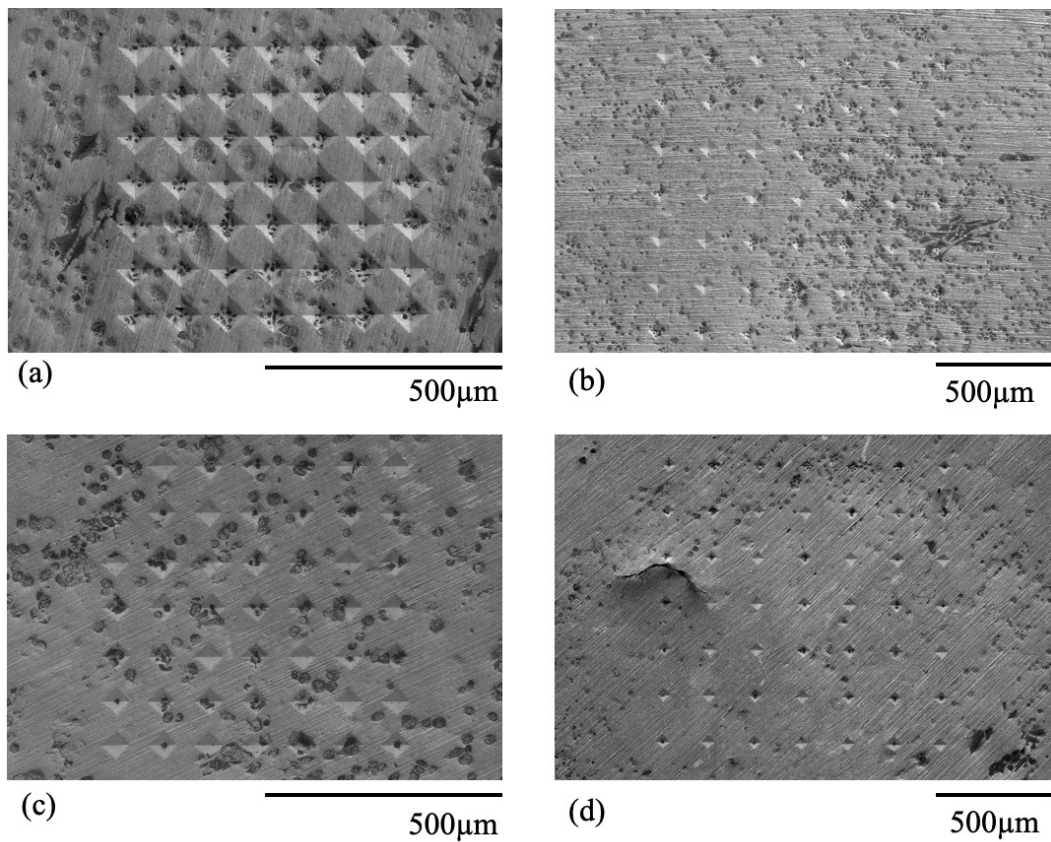


Figure 4. FESEM images of the Saos-2 cells fixated on the overall micro-deformation areas of (a) Sample-1, (b) Sample-2, (c) Sample-3, (d) Sample-4; following 10 days of incubation.

processing exhibited higher cell density on their micro-deformation areas as compared to the reference sample on the 5th day of incubation, suggesting a positive effect stemming

from micro-deformation (Figure 6 (a)). On the other hand, attachment behaviors of the Saos-2 cells fixated on patterned samples exhibited significant differences depending

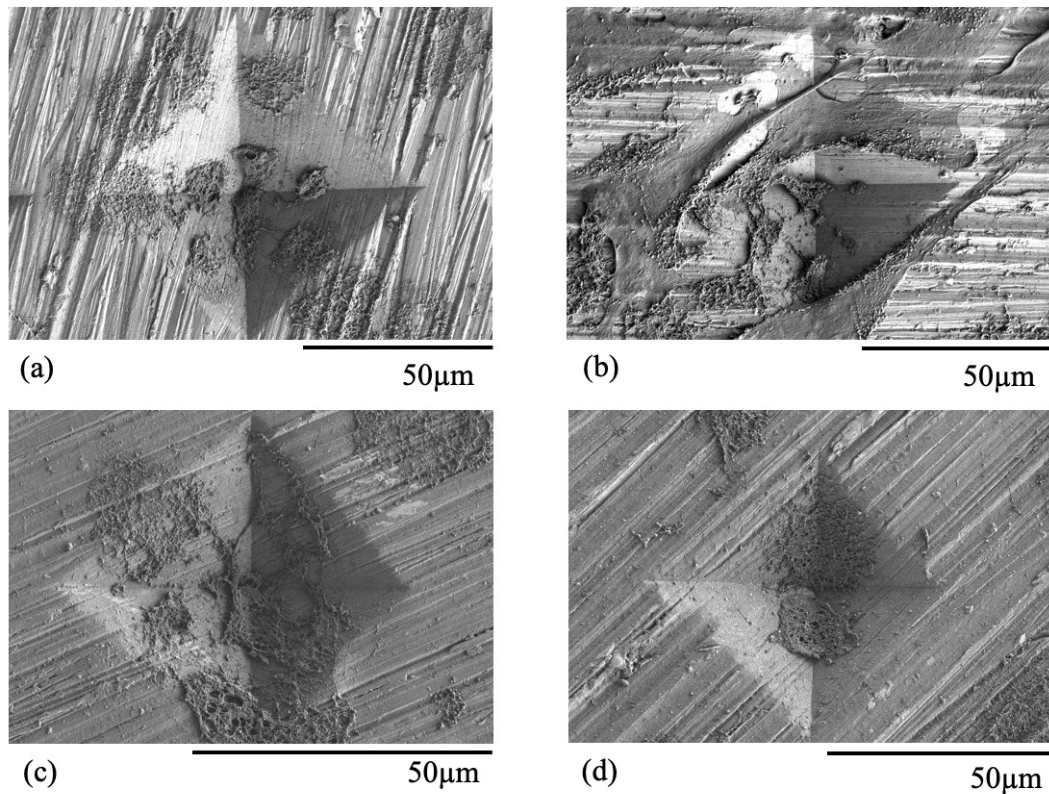


Figure 5. FESEM images of the Saos-2 cells around individual indents of (a) Sample-1, (b) Sample-2, (c) Sample-3, (d) Sample-4; following 10 days of incubation.

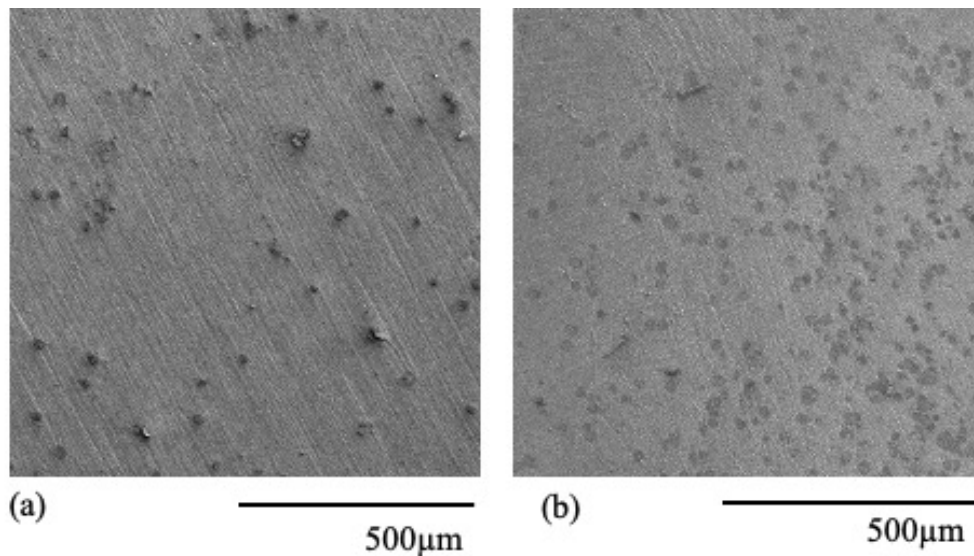


Figure 6. FESEM images of the Saos-2 cells on the reference sample surface (a) following 5 days of incubation, (b) following 10 days of incubation.

on the micro-deformation pattern and varying roughness values. (Figures 2-5). Specifically, according to Figure 2, on the 5th day of incubation; a higher number of cells were apparent on samples 3 and 4, which exhibit lower surface roughness and shallower indents as compared to samples 1 and 2. The closer look on individual indents also yielded a similar result with higher cell density located within and around the indents of samples 3 and 4. These results showed that, up to 5 days of incubation, increased surface roughness had a negative effect on cell attachment for the samples with micro-deformation.

However, on the 10th day of incubation, a completely dif-

ferent cellular behavior was observed. The general view of the patterned areas exhibited higher numbers of cells on samples 1 and 2 this time, as compared to samples 3 and 4 (Figure 4). Moreover, higher densities of cells were apparent within and around individual indents of samples 1 and 2 as well, in comparison to samples 3 and 4 (Figure 5). These findings indicated that increased surface roughness exhibited a positive effect on cell attachment on the 10th day of incubation, contradicting the observations from day 5 of incubation. Therefore, it can be argued that, in addition to surface roughness, another parameter affecting this behavior is indent characteristics. Specifically, the larger indent size of

samples 1 and 2 enabled localization of a higher number of cells over time, which also contributed to increased cellular attachment on these surfaces through 10th day of incubation. On the other hand, the cell density on the surface of the reference sample appeared to be lower as compared to the patterned surfaces, demonstrating the positive effect of surface micro-deformation on cell attachment behavior on the 10th day of incubation as well.

In order to make a quantitative evaluation in addition to visual observations, the number of cells on the patterned area of each sample on each incubation period were counted and presented as a bar graph comparing the numbers of cells per mm² area (Figure 7). These quantitative results support the observations from the FESEM images as well. Specifically, this graph also reveals an inverse correlation between surface roughness and cell attachment at the early stage of incubation, whereas at the later stage of incubation, increased surface roughness appears to promote cellular attachment and proliferation for the surfaces with micro-deformation. Also, the higher numbers of cells per mm² on all of the micro-deformation surfaces in comparison to the reference sample surface, support the FESEM observations where surface-micro-deformation processing in general appear to promote cellular attachment.

Moreover, this graph provides a basis for comparing the samples with the same indent size (namely sample 1 vs. 2 and sample 3 vs. 4) with each other. According to this comparison, initially at both incubation periods, the numbers of cells were higher on sample 1 than sample 2. Sample 1 exhibited the highest surface roughness and in many studies higher surface roughness was observed to positively influence cellular attachment due to the increased surface energy [8, 9]. However, comparing the percentage change in the number of cells over time, the number of cells increased by 174% on sample 1, while a significant increase of 380% was apparent on sample 2. This observation is an important indicator of how a direct correlation may not always be present between surface roughness and cell attachment. The cell count comparisons from the 5th day of incubation also evidence a similar finding where surfaces with lower roughness values resulted in higher numbers of cell attachment. On the other hand, from the comparison between samples 3 and 4, whose indent sizes are the same, it can be observed that this time the sample with the higher surface roughness, namely sample 3, appears to promote cellular attachment and proliferation more than sample 4, with similar percentage changes over time. Lastly, comparing samples 1 and 3 with samples 2 and 4 in order to get an understanding of the effect of indent spacing; it can be argued that closer indent spacing also exhibits a more positive effect on cell attachment.

Overall, these results indicate that, in addition to surface roughness, the indent size and the spacing are also important parameters affecting the surface energy and thus cell attachment behavior on the surface. Moreover, the surface energy changes stemming from micro-structural mecha-

nisms which are induced by the formation of these micro indents, are also expected to be effective in the observed results of cell attachment and proliferation behavior. Similar results where the effects of the structural features and micro-structural mechanisms were more prominent in terms of affecting cellular behavior as compared to surface roughness were reported in literature as well [10-12]. Therefore, it can be argued that surface energy changes stemming from microstructural mechanisms constitute another important factor affecting cellular response and should be investigated in detail in the future studies.

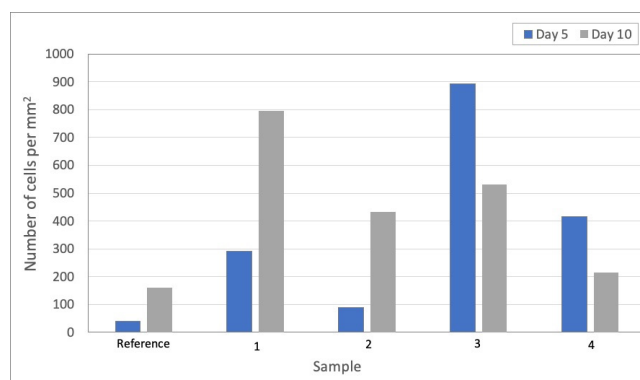


Figure 7. The number of cells per mm² area on the reference sample surface and micro-deformation area of each sample on the 5th and 10th days of incubation.

17. CONCLUSION

The findings of this study revealed that cell attachment and proliferation behaviors were not only influenced by surface roughness, but also by the specifics of the surface features of the different micro-deformation areas. Specifically, the indent size and spacings were also found to play a determining role on the cell attachment and proliferation behavior. Moreover, these results suggest that the effects of micro-structural mechanisms on surface energy, which were induced by micro-deformation, can also influence the cellular behavior and this effect should be investigated in detail in the future studies.

5. ACKNOWLEDGEMENTS

This work was financially supported by the ESOGU Bilimsel Araştırma Projeleri (BAP) Grant, Project # 2018/15038. The authors would also like to thank the members of ESOGU Cellular Therapy and Stem Cell Production, Application and Research Center (ESTEM) for their help through the *in vitro* experiments.

REFERENCES

- [1] Bauer, S., Schmuki, P., Mark, K.V.D., Park, J. (2013). Engineering Biocompatible Implant Surfaces Part I: Materials and Surfaces. *Progress in Materials Science*, 58(3):261-326, DOI: 10.1016/j.pmatsci.2012.09.001.
- [2] Manam, N.S., Harun, W.S.W., Shri, D.N.A., Ghani, S.A.C., Kurniawan, T., Ismail, M.H., Ibrahim, M.H.I. (2017). Study of Corrosion in Biocompatible Metals for Implants: A Review. *Journal of Alloys and Compounds*, 701: 698-715, DOI: 10.1016/j.jallcom.2017.01.196.
- [3] Toker, S.M., Canadinc, D., Maier, H.J., Birer, O. (2014). Evaluation of

Passive Oxide Layer Formation- Biocompatibility Relationship in NiTi Shape Memory Alloys: Geometry and Body Location Dependency. *Materials Science and Engineering C*, 36:118-129, DOI: doi.org/10.1016/j.msec.2013.11.040.

- [4] Lu, T., Wen, J., Qian, S., Cao, H., Ning, C., Pan, X., Jiang, X., Liu, X., Chu, P. K. (2015). Enhanced Osteointegration on Tantalum- Implanted Polyetheretherketone Surface with Bone-Like Elastic Modulus. *Biomaterials*, 51: 173-183, DOI: 10.1016/j.biomaterials.2015.02.018.
- [5] Keyf, F., Uzun, G. (2007). Surface Characteristics of the Implant Systems and Osseointegration. *Journal of Atatürk University Faculty of Dentistry*, 2: 43-50.
- [6] Sahin, C., Korkmaz, C., Uzun, G. (2015). Osseointegration, Surface Porosity and Nanotechnology. *Journal of Atatürk University Faculty of Dentistry*, 25(13): 174-181, DOI: 10.17567/dfd.90462.
- [7] Toker, S.M., Gerstein, G., Maier, H.J., Canadinc, D. (2018). Effects of Microstructural Mechanisms on The Localized Oxidation Behavior of NiTi Shape Memory Alloys in Simulated Body fluid. *Journal of Materials Science*, 53: 948-958, DOI:10.1007/s10853-017-1586-4.
- [8] Venkatsurya, P.K.C., Thein, W.W., Misra, R.D.K., Somani, M.C., Karjalainen, L.P. (2010). Advancing Nanograined/Ultrafine-grained Structures for Metal Implant Technology: Interplay Between Grooving of Nano/Ultrafine Grains and Cellular Response. *Materials Science and Engineering C*, 30(7):1050-1059, DOI: 10.1016/j.msec.2010.05.008.
- [9] Liang, C., Wang, H., Yang, J., Li B., Yang, Y., Li, H. (2012). Biocompatibility of The Micro-Patterned NiTi Surface Produced by Femtosecond Laser. *Applied Surface Science*, 261: 337-342, DOI: 10.1016/j.apsusc.2012.08.011.
- [10] Uzer, B., Toker, S.M., Cingoz, A., Bagci-Onder, T., Gerstein, G., Maier, H.J., Canadinc, D. (2016). An Exploration of Plastic Deformation Dependence of Cell Viability and Adhesion in Metallic Implant Materials. *Journal of the Mechanical Behavior of Biomedical Materials*, 60: 177-186. DOI: 10.1016/j.jmbbm.2016.01.001.
- [11] Toker, S.M., Sugerman, G., Frey, E.C. (2019). Effects of Surface Characteristics on the in vitro Biocompatibility Response of NiTi Shape Memory Alloys. *Academic Platform Journal of Engineering and Science*, 7(2): 112-116. DOI: 10.21541/apjes.461169.
- [12] Uzer, B. (2020) Modulating the Surface Properties of Metallic Implants and the Response of Breast Cancer Cells by Surface Relief Induced via Bulk Plastic Deformation. *Frontiers in Materials*, 7: 1-10. DOI:10.3389/fmats.2020.00099.



Effect of Build Orientation on Mechanical Behaviour and Build Time of FDM 3D-Printed PLA Parts: An Experimental Investigation

Meltem Eryildiz^{1*} 

¹Department of Mechanical Engineering, Faculty of Engineering and Architecture, Beykent University, Istanbul, 34398, Turkey

Abstract

One of the important process parameters affecting the tensile strength and build time of the part is the build orientation. Therefore, in this study, FDM 3D-printed PLA parts were fabricated at different build orientations to examine the effects of build orientation on the tensile properties and build time of material. In this regard, three build orientations and three print angles were examined. According to results, tensile strength decreased when the build orientation of the parts was aligned from flat to upright direction and 0° to 90° printing angle. For upright build orientation, 36% less tensile strength was obtained compared to the flat ones because of the fracture mode and the loading direction. In terms of build time, build time increased as the build orientation changed from flat to upright. Therefore, the build orientation had a big impact on the tensile properties and build time of the parts produced using FDM. The findings of this study will contribute to the literature on proper build orientations and print angles.

Keywords: Fused deposition modeling, 3D printing, build orientation, build time, tensile strength, PLA

18. INTRODUCTION

Additive manufacturing (AM) creates 3D parts by adding layer-upon-layer of material for a wide variety of industrial and other applications. Contrary to the traditional production technique in which the material is removed until the desired part is obtained, AM is used in variety applications in defense, aircraft, medical, automobile industries etc. There are many different AM techniques, including Stereolithography (SLA), Selective Laser Sintering (SLS) or Laminated Object Manufacturing (LOM), etc. Among these AM techniques, Fused Deposition Modeling (FDM) stands out and is frequently used around the world [1-3]. A wide variety of materials are available in the FDM technique which has low maintenance cost, low fabrication cost even for complex parts and is environmentally friendly [4]. G-codes files are generated directly from CAD files, usually in STL format. In this technique, parts are produced by adding layer upon layer of material until the shape of the part is formed. Filament is heated to a semi-liquid state and G-code controls the movement of the nozzle as shown in Figure 1 [5,6].

Many process parameters in FDM have great influence on the component properties and production efficiencies. Layer thickness, raster angle, build orientation, infill density, printing speed, infill pattern, raster width, etc. can be listed

as some of the important process parameters. Researchers are still working hard to obtain the best parameter settings. Therefore, in order to improve the mechanical properties of the printed parts by setting optimal process parameters, the FDM process needs to be studied more intensively [1,6]. Build orientation shows how the part is positioned relative to the three major axes of the 3D printer [6]. For instance, Feng et al. [7] fabricated PA12 (polyamide 12), and Corapi et al. [8] fabricated FDM 3D-printed PLA ((polylactide acid) parts in different directions. Moreover, Ashtankar et al. [9] showed the effect of build orientation of FDM 3D-printed ABS (Acrylonitrile Butadiene Styrene) parts and their result indicated that the compressive strength and tensile strength decreased when the orientation of the samples was aligned from 0° to 90°. Thrimurthulu et al. [10] studied optimum build orientation in FDM. Durgun and Ertan [11] demonstrated that the samples built with 0° raster angle in the horizontal direction had best mechanical properties and surface roughness with the optimal build time and cost. Thus, it has been observed that, the build orientation for the parts produced using the FDM method has a great effect on the mechanical properties of the part [12]. Also, the printing angle affects the mechanical properties of the FDM 3D-printed parts because it affects the anisotropy [13].

* Corresponding author
Email: meltemeryildiz@beykent.edu.tr



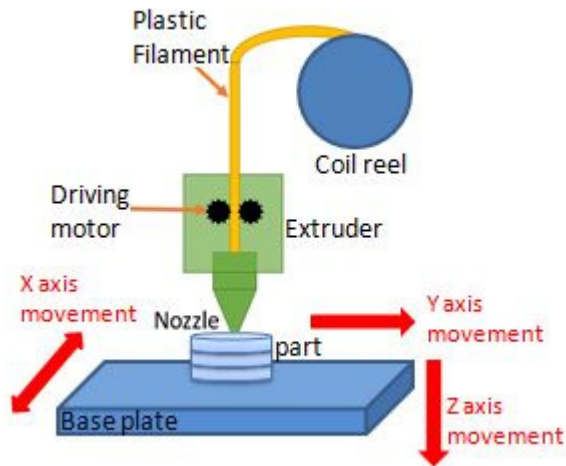


Figure 1. FDM process schematic [6]

Aim of this study is to investigate the influence of build orientation on the tensile properties and build time. The effects of flat and upright build orientations and flat printing angles on the tensile strength and build time of FDM parts were examined in this context. In this study, PLA (polylactide acid) was used due to its interesting properties in terms of non-toxicity, biodegradability and ease of processing. In order to analyze the impacts of build orientation on the tensile behavior and build time of the material, three build orientations and three print angles were examined.

19. EXPERIMENTAL METHODS

Commercial Poly(lactide acid) (PLA) filament with a 1.75 mm diameter was used on a 3D Printing machine, Creality ender

3d pro (Figure 2). The nozzle diameter was 0.4 mm. The data of the specimens were all in STL format and then translated into G-code sliced with slic3r. Slic3r is an open source slicer software. In this study, specimens for each direction (flat, on edge, upright, and flat-0°, 45°, 90° angle-, Figure 3) and have been printed for the tensile test. The process parameters not only affect the mechanical strength of the parts but also the build time.

The parts were fabricated under the American Society



Figure 2. Ender 3 pro 3D printer

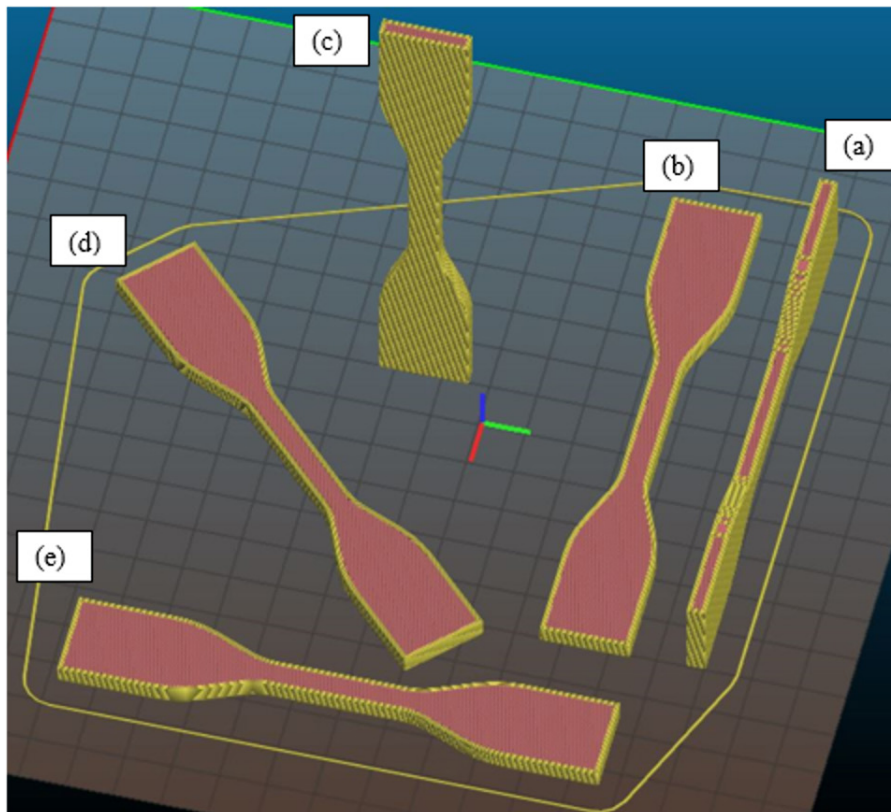


Figure 3. Tensile specimen oriented in various build orientations (a) on edge, (b) flat 0°, (c) upright, (d) flat 45°, (e) flat 90°

for Testing and Materials (ASTM) standard D638 type IV shown in the Figure 4. The dog bone type parts were built according to the process parameters given in Table 1.

Table 1. Parameters of printer settings.

| Items | Value |
|-----------------------------|-------|
| Nozzle diameter [mm] | 0.4 |
| Wall thickness [mm] | 0.8 |
| Layer height [mm] | 0.2 |
| Wall line count | 3 |
| Infill Density [%] | 30 |
| Printing Temperature [C] | 200 |
| Build Plate Temperature [C] | 60 |
| Print Speed [mm/s] | 60 |

The tensile tests are performed on universal testing machines (Instron 8872) with a load cell of 25 kN at room temperature (Figure 5). The test speed was 1 mm/min.

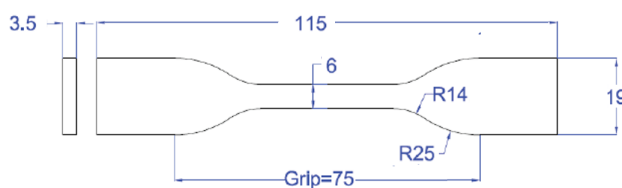


Figure 4. CAD model of the specimen, dimensions in mm

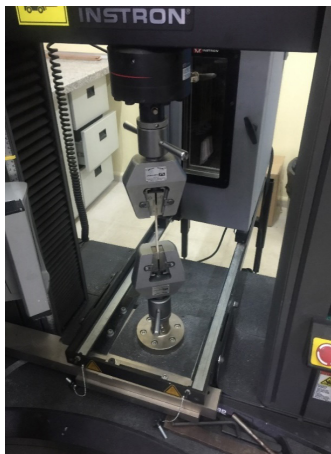


Figure 5. Tensile test setup

20. RESULTS AND DISCUSSION

The tensile strength, filament spent and build time of the samples are listed in Table 2. The stress-strain curves of samples printed in different orientations are plotted in Figure 6. Build time was taken by the machine to fabricate the parts.

Table 2. The tensile strength, filament spent and build time of the samples

| | Build Time [min] | Filament Spent [mm] | Tensile Strength [MPa] |
|--------------|------------------|---------------------|------------------------|
| (a) on edge | 59 | 1846.5 | 48.18 |
| (b) flat 0° | 29 | 1231.4 | 55.49 |
| (c) upright | 231 | 2037.2 | 35.52 |
| (d) flat 45° | 29 | 1207.9 | 53.47 |
| (e) flat 90° | 29 | 1231.4 | 51.77 |

In terms of mechanical properties, it can be seen from Figure 6 and Table 2 that the flat 0° orientation reaches maximum tensile strength (55.49 MPa), while the upright orientation reaches the minimum (35.52 MPa). Because the tensile

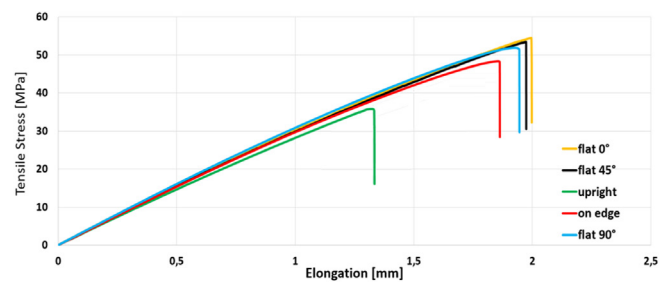


Figure 6. The stress-strain curves of the samples at different building orientations

strength of FDM 3D-printed PLA parts becomes optimal if the parts are fully oriented along the direction of loading stress [14]. As shown in Figure 7a, the parts that can transfer the stress at the highest level are the parts oriented along the loading stress direction. And, as shown in Figure 7b, fracture mode of the upright build orientation differs from the flat build orientation. There are two types of fracture modes which are the interlayer fracture and the intra-layer fracture and the fracture mode affects the mechanical strength of the FDM 3D-printed PLA parts. The interlayer fracture strength mainly depends on the interlayer bonding strength, and the intra-layer fracture mainly depends on the strength of the extruded material [13]. Obviously, the loading direction of the upright build oriented part is totally perpendicular to the direction of the extruded lines, indicating that the bond between line and line is weak and that interlayer fracture occurs easily during the tensile test [8,14]. According to the tensile results listed in Table 2, samples printed in horizontal directions exhibited higher tensile strength, while samples printed in vertical (upright) direction exhibited 36% lower tensile strength.

In terms of print angles, it was seen that the mechanical properties and build time of the flat 0°, flat 45°, flat 90° parts were not much different (Figure 6 and Table 2). The print

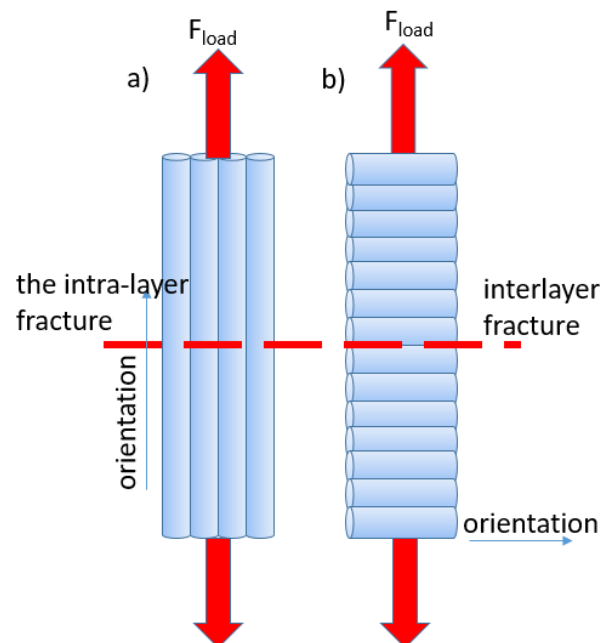


Figure 7. Tensile failure mechanism at (a) flat (horizontal), (b) upright (vertical) orientation

angles can be seen in Figure 8. It has been observed that, the 0° angle had the maximum tensile strength, followed by the 45°, and 90° printing angles, respectively. The tensile strength for the 0°, 45°, and 90° printing angles were 55.49 MPa, 53.47 MPa, and 51.77 MPa, respectively. The reason the 0° printing angle had the highest mechanical properties was that the orientation of the structure aligned with the direction of the loading force in a single slice of the original filament. Thus, the direction of the loading should be considered when designing and applying the FDM 3D-printed PLA parts [15].

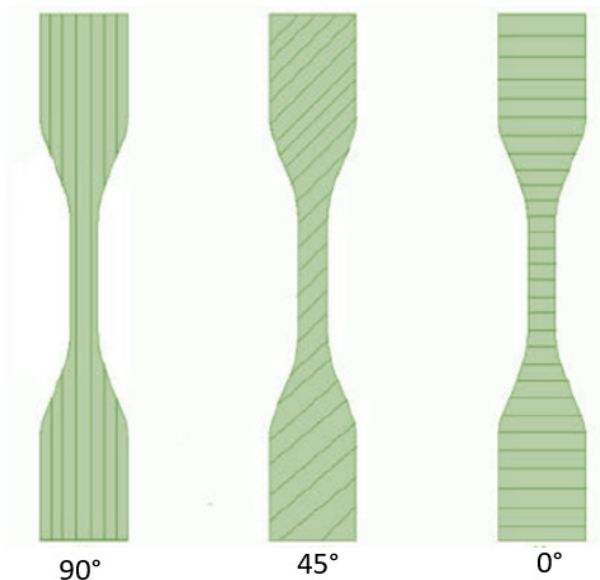


Figure 8. Schematic representation of the printed direction in each slice

From the standpoint of build time, as the build orientation changed from flat to upright, the build time increased. At the upright build orientation, the required build time increased because the number of layers for this build orientation was much higher. Furthermore, it has been known that when the build time becomes longer and higher amount of material is used, energy usage increases and this leads to higher energy costs [16]. Thus, FDM 3D-printed PLA parts can be manufactured with good mechanical properties with minimal build time at the flat build orientation.

21. CONCLUSIONS

FDM 3D-printed PLA parts were fabricated at different build orientations to examine the effects of build orientation on the tensile properties and build time of the material. In this regard, three build orientations and three print angles were examined. According to results, tensile strength decreased when the build orientation of the parts was aligned from flat to upright direction and 0° to 90° printing angle. For upright build orientation, 36% less tensile strength was obtained compared to the flat ones because of the fracture mode and the loading direction. It is thus revealed that the build orientation had a big impact on the mechanical properties and build time of the FDM 3D-printed PLA parts. The build orientation and the direction of the loading must be considered in terms of mechanical properties and man-

ufacturing cost, when designing and applying the FDM 3D-printed PLA parts.

RERERENCES

- [1] Altan, M., Eryildiz, M., Gumus, B., Kahraman, Y. (2018). Effects of process parameters on the quality of PLA products fabricated by fused deposition modeling (FDM): surface roughness and tensile strength. *Materials Testing*, 60(5): 471-477, DOI: 10.3139/120.111178
- [2] Srinivasan, R., Ruban, W., Deepanraj, A., Bhuvanesh, R., Bhuvanesh, T. (2020). Effect on infill density on mechanical properties of PETG part fabricated by fused deposition modelling. *Materials Today: Proceedings*, 27(2):1838-1842, DOI: 10.1016/j.matpr.2020.03.797
- [3] Bardiya, S., Jerald, J., Satheeshkumar, V. (2020). Effect of process parameters on the impact strength of fused filament fabricated (FFF) polylactic acid (PLA) parts. *Materials Today: Proceedings*, DOI: 10.1016/j.matpr.2020.08.066
- [4] Garg, A., Bhattacharya, A., Batish, A. (2015). On Surface Finish and Dimensional Accuracy of FDM Parts after Cold Vapor Treatment. *Materials and Manufacturing Processes*, 31(4): 522-529, DOI: 10.1080/10426914.2015.1070425
- [5] Alafaghani, A., Qattawi, A., Alrawi, B., Guzman, A. (2017). Experimental Optimization of Fused Deposition Modelling Processing Parameters: A Design-for-Manufacturing Approach. *Procedia Manufacturing*, 10: 791-803, DOI: 10.1016/j.promfg.2017.07.079
- [6] Solomon, I.J., Sevel, P., Gunasekaran, J. (in press). A review on the various processing parameters in FDM. *Materials Today: Proceedings*, DOI: 10.1016/j.matpr.2020.05.484
- [7] Feng, L., Wang, Y., Wei, Q. (2019). PA12 Powder Recycled from SLS for FDM. *Polymers*, 11: 727-729, DOI: 10.3390/polym11040727
- [8] Corapi, D., Morettini, G., Pascoletti, G., Zitelli, C. (2019). Characterization of a Polylactic acid (PLA) produced by Fused Deposition Modeling (FDM) technology. *Procedia Structural Integrity*, 24: 289-295, DOI: 10.1016/j.prostr.2020.02.026
- [9] Ashtankar, K.M., Kuthe, A.M., Rathour, B.S. (2013). Effect of build orientation on mechanical properties of rapid prototyping (Fused Deposition Modeling) made Acrylonitrile Butadiene Styrene (ABS) Parts. *ASME 2013 International Mechanical Engineering Congress and Exposition*, 11: 1-7, DOI: 10.1115/IMECE2013-63146
- [10] Thrimurthulu, K., Pandey, P., Reddy, N.V. (2004). Optimum Part Deposition Orientation in Fused Deposition Modelling. *International Journal of Machine Tools*, 44: 585-594, DOI: 10.1016/j.ijmachtools.2003.12.004
- [11] Durgun, I., Ertan, R. (2014). Experimental Investigation of FDM Process for Improvement of Mechanical Properties and Production Cost. *Rapid prototyping*, 20(3): 228-235, DOI: 10.1108/RPJ-10-2012-0091
- [12] Chaudhari, M., Jogi, B.F., Pawade, R.S. (2018). Comparative Study of Part Characteristics Built Using Additive Manufacturing (FDM). *Procedia Manuf*, 20: 73-78, DOI: 10.1016/j.promfg.2018.02.010.
- [13] Wang, S., Ma, Y., Deng, Z., Zhang, S., Cai, J. (2020). Effects of fused deposition modeling process parameters on tensile, dynamic mechanical properties of 3D printed polylactic acid materials. *Polymer testing*, 86: 106483, DOI: 10.1016/j.polymer.2020.106483
- [14] Liu, H., He, H., Peng, X., Huang, B., Li, J. (2019). Three-dimensional printing of poly(lactic acid) bio-based composites with sugarcane bagasse fiber: Effect of printing orientation on tensile performance. *Advances in Polymer Technology*, 30: 910- 922, DOI: 10.1002/pat.4524

- [15] Cai, L., Byrd, P., Zhang, H., Schlarman, K., Zhang, Y., Golub, M., Zhang, J. (2016). Effect of Printing Orientation on Strength of 3D Printed ABS Plastics. The Minerals, Metals & Materials Society. (Eds.), TMS 2016 145th Annual Meeting & Exhibition. Springer, Cham, p. 199-204.
- [16] Jiang, J., Xu, X., Stringer, X. (2018). Support Structures for Additive Manufacturing: A Review, *Journal of Manufacturing and Materials Processing*, 2(64): 1-23, DOI: 10.3390/jmmp2040064



Characterization of Mechanical of CTBN Liquid Rubber-Modified Epoxy Cured by Anhydride- and Amine-Based Agent

Harun Sepetcioglu^{1*} 

¹Selçuk University, Faculty of Technology, Metallurgical and Materials Engineering Department, Konya, 42030, Turkey

Abstract

The main purpose of this work is to reveal the effects of carboxyl-terminated butadiene–acrylonitrile (CTBN) rubber particles on the tensile and fracture behavior of CTBN/epoxy blends cured with anhydride- and amine-based agents. In this study, 1 wt.%, 3 wt.%, 5 wt.%, 7 wt.%, 10 wt.% and 15 wt.% CTBN were added to two different epoxy systems. The CTBN/epoxy blends were prepared by ultrasonic mixing device, and curing processes were determined by DSC analysis. As CTBN fraction by weight increased in both epoxy systems, a decrease in tensile strength and modulus was detected, but deformation ability improved. The fracture toughness of CTBN/epoxy blends cured with the amine-based agent increased up to 10 wt.% CTBN addition. However, fracture toughness decreased when 15% by weight of CTBN was added to the epoxy matrix. The average rubber particle size was found to have a significant effect on the fracture toughness of CTBN/epoxy blends. Compared to pure epoxy, fracture toughness was increased approximately 3.5-fold in 10 wt.% CTBN/epoxy blend cured with the amine-based agent. In CTBN/epoxy blends cured with the amine-based agent, CTBN shifted the reaction rate and thus it was provided better control over CTBN particle size in the CTBN/epoxy cured. The toughening mechanisms induced by CTBN, such as rubber cavitation and matrix shear banding, contributed to the enhanced fracture toughness of the CTBN/epoxy cured with the amine-based agent.

Keywords: Epoxy, CTBN, fracture toughness, tensile properties, curing agent type.

22. INTRODUCTION

Epoxy resins, a member of the thermoset group, have widely used as matrix materials in the production of polymer matrix composite materials [1]. The high-performance protective coatings, structural adhesives, structural materials are other areas of use. Among polymer matrices, epoxy resins are preferred over other thermoset matrices in terms of their thermal stability, mechanical properties and processability [2]. They are commonly cured with amine-based agents to form rigid network polymers [3]. However, other hardener groups such as acids and anhydrides are also used for curing epoxy resins [4]. When epoxy resins are subjected to a curing process, they form a high cross-linking rate and turn into an amorphous thermoset material. These cross-linked structures are majorly brittle. In addition, they are very poorly resistant to crack formation and growth [5]. This behavior limits their use in aerospace, defense, and automotive applications. It is a common effort to add any rubber type to the matrix to increase the toughness of the epoxy. On this topic, controlling the curing reactions to induce phase separation of the rubber has been extensively studied in the literature [4, 6-14]. Carboxy-terminated butadiene acrylo-

nitrile (CTBN) was used in most of these studies to modify the epoxy. Modification methods of the epoxy matrix traditionally involve two main steps. Firstly, CTBN and epoxy are mixed, and a pre-polymer blend is obtained. Secondly, the curing agent is added to this pre-blend and then carried out to the curing process. When the toughening rigid CTBN/epoxy network is examined under a microscope, a distribution and dispersed rubber phase in the epoxy matrix is seen. The fracture behavior of final products produced by CTBN/epoxy blends depends on the size of the rubber particles [12, 15-17].

The Chemical bond formation is required for an efficient stress transfer between CTBN and epoxy [18]. This bond formation may occur at low and high temperatures depending on the type of curing agent. During the curing of the CTBN/epoxy blend, the separation of the rubber phase from the epoxy matrix occurs. The molecular weight of the epoxy increases with the decrease of the configurational entropy in the curing process [19-23]. It leads to a decrease in the solubility of CTBN with the increase of the molecular weight of the epoxy. Chemical reactions controlling cross-link density between epoxy and curing agent are effective

* Corresponding author
Email: harunsepet@selcuk.edu.tr



in the precipitation of rubber particles. In addition, the particle size and distribution of rubbers formed in the epoxy matrix depend on the curing procedure and the interaction between the rubber and epoxy resin [24–26].

The epoxy systems are used in the polymer industry. The mechanical properties of the final product produced with these systems depend on the nature of the curing agent used, and anhydride- and amine-based curing agents are widely used in the composite industry. The aim of the study is to investigate the tensile and fracture properties of CTBN/epoxy cured with anhydride- and amine-based curing agents. The mechanical properties of the blends depend on the homogeneous dispersion of CTBN in epoxy and the curing and post-curing processes. The fracture tests by using linear fracture mechanics (LEFM), and tensile tests were carried out on the blends. Relationships between fracture toughness and the average rubber particle size have been reported.

23. MATERIALS AND METHODS

23.1. Materials

For this study, diglycidyl ether of bisphenol A resins with low viscosity in the two different standards (trade name; EPIKOTE™ 828 LVEL and Laminating resin MGS L285) were preferred. Hexahydrophthalic anhydride (trade name; EPIKURE™ H866) and 3-aminomethyl-3,5,5-trimethylcyclohexylamine (trade name; L285) are curing agents of these epoxy resins.

Table 1. The properties of the CTBN liquid rubber

| Properties | Values |
|--------------------------|-----------|
| Viscosity, (40 °C) Pa.s | 7-12 |
| Carboxyl content, mmol/g | 0.58~0.65 |
| Nitrile group content, % | 8.0~12.0 |
| Water content, % ≤ | 0.05 |
| Volatile content, % ≤ | 2.0 |

To modify the epoxy, the liquid rubber used is carboxyl-terminated butadiene–acrylonitrile copolymer (CTBN) purchased from Zibo Qilong, China. The properties of CTBN liquid rubber given in Table 1.

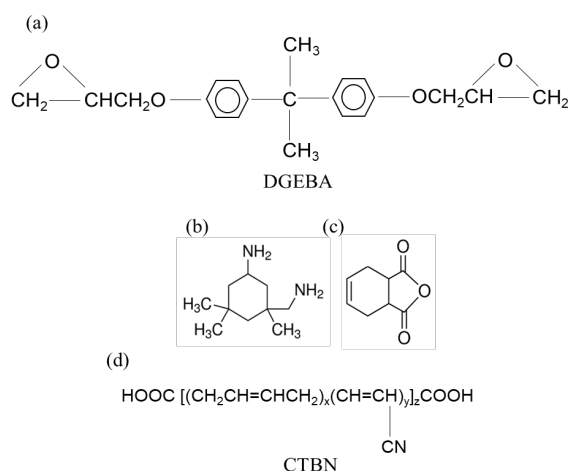


Figure 1. The chemical structure of components (a) diglycidyl ether of bisphenol A (DGEBA), (b) 3-aminomethyl-3,5,5-trimethylcyclohexylamine, (c) hexahydrophthalic anhydride and (d) carboxyl terminated butadiene acrylonitrile (CTBN) used in this study.

23.2. Production of epoxy/CTBN blends

0, 1, 3, 5, 7, 10, and 15 wt.% CTBN was added to the MGS LR285 and the 828 LVEL epoxy resins. The CTBN/MGS LR285 and CTBN/828 LVEL blends were heated up to 25 °C and 60 °C, respectively. Afterward, both blends were mixed together continuously until a clear blend was obtained, then the blends were degassed at 25 °C by vacuum for about 10 minutes. After, it was used curing processes, offering the high mechanical properties provided by the resin manufacturers for both the blends. A stoichiometric amount of amine-based L285 and anhydride-based H866 curing agents were added to CTBN/MGS LR285 and CTBN/828 LVEL blends, respectively. Both blends containing curing agents were stirred slowly. The CTBN/MGS LR285/L285 blends were cured at 60 °C for 1 hour, and then post-cured for 3 hours at 90 °C. Then, the other CTBN/828 LVEL/H866 blends were cured at 120 °C for 3 hours, and then post-cured for 3 hours at 150 °C. The ratios of components in CTBN/epoxy blends cured by anhydride- and amine-based were given in Table 2 and Table 3, respectively.

Table 2. The ratios of CTBN/epoxy blends cured by anhydride-based

| Sample Codes | Trade name of resin | Trade name of curing agent | Bisphenol-A Epoxy resin, wt.% | CTBN*, wt.% | Anhydride-based curing agent wt.% |
|--------------|---------------------|----------------------------|-------------------------------|-------------|-----------------------------------|
| 8H0 | 828 LVEL | H866 | 80 | 0 | 20 |
| 8H1 | | | | 1 | |
| 8H3 | | | | 3 | |
| 8H5 | | | | 5 | |
| 8H7 | | | | 7 | |
| 8H10 | | | | 10 | |
| 8H15 | | | | 15 | |

* 0-15 wt.% CTBN was added onto the combination of the curing agent/epoxy in stoichiometric amount (20/80).

Table 3. The ratios of CTBN/epoxy blends cured by amine-based

| Sample Codes | Trade name of resin | Trade name of curing agent | Bisphenol-A Epoxy resin, wt.% | CTBN*, wt.% | Amine-based curing agent wt.% |
|--------------|---------------------|----------------------------|-------------------------------|-------------|-------------------------------|
| ML0 | MGS LR285 | L285 | 60 | 0 | 40 |
| ML1 | | | | 1 | |
| ML3 | | | | 3 | |
| ML5 | | | | 5 | |
| ML7 | | | | 7 | |
| ML10 | | | | 10 | |
| ML15 | | | | 15 | |

* 0-15 wt.% CTBN was added onto the combination of the curing agent/epoxy in stoichiometric amount (40/60).

23.3. Mechanical characterization

The static tensile properties of the composites were determined at room temperature (24 °C) using a Shimadzu tester (AGS-X Series) with a crosshead speed of 2 mm/min, according to ASTM D638. Three samples of each composition were tested, and the average value and standard deviation were reported. The Mode-I critical stress intensity factor (K_{Ic}) was measured using single edge notched bend (SENB) samples of 10×20×88 mm³, which ensures the plane

strain condition according to ASTM D5045. Dimensions of tensile and fracture test samples used in mechanical characterization were given in Figure 2. The SENB sample and three-point flexural test fixture used in the fracture toughness measurements were shown in Figure 3.

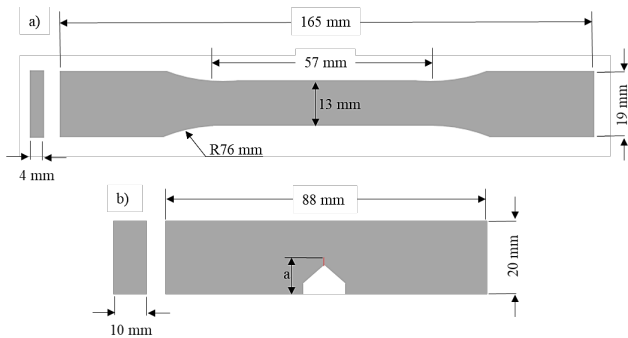


Figure 2. Dimensions of tensile (a) and fracture (b) test samples used in mechanical characterization

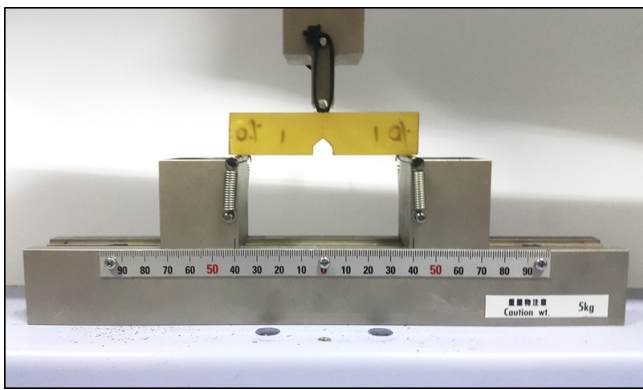


Figure 3. Fracture toughness measurements on SENB sample

The sharp crack was generated by a fresh razor blade, which was fixed to tool holder of universal milling machine, on the notch in the middle of the rectangular bar. The fracture tests were conducted on the same Shimadzu tester at a crosshead speed of 10 mm/min. The K_{IC} values were calculated using the following relationship:

$$K_Q = \left(\frac{P_Q}{BW^{3/2}} \right) f(x) \tag{1}$$

$$f(x) = 6x^{1/2} \left[\frac{1.99 - x(1-x)(2.15 - 3.93x + 2.7x^2)}{(1+2x)(1-x)^{3/2}} \right] \tag{2}$$

$$x = a / W \tag{3}$$

$$B, a, W - a \geq 2.5 \left(\frac{K_Q}{\sigma_{YS}} \right)^2 \tag{4}$$

where, K_Q is a provisional fracture toughness, $f(x)$ the shape factor, P_Q the peak load, B the sample thickness, W the sample width, a the crack length, σ_{YS} the yield strength. Eq. (4) was satisfied for the dimensions of produced SENB samples. The SENB samples were loaded up to break on a Shimadzu tester (AGS-X Series) under a crosshead speed of 10 mm/min. The value of the strain energy release rate (G_{IC}) was calculated from the knowledge of the values of K_{IC} and E , using the relationship:

$$K_{IC}^2 = \left(\frac{EG_{IC}}{(1-\nu^2)} \right) \tag{5}$$

where ν is the Poisson's ratio and was taken to be 0.35 in value [27, 28].

23.4. Differential scanning calorimetry analysis

Differential scanning calorimetric (DSC) analysis was employed to study the curing processes of the pure epoxy and 10 wt.% CTBN/epoxy blend. The DSC measurements were performed with a METTLER TOLEDO DSC 1-STAR System calorimeter by using a computer for data acquisition. Isothermal heating measurements were carried out in a nitrogen flow of 50 ml/min. The heating was made from 25 °C to the temperature of the isotherm at a heating rate of 5 °C/min. The curing process of the pure epoxy and CTBN/epoxy blends govern the mechanical and thermal properties that are crucial in applications.

23.5. Examination of Fracture Surfaces

Dispersion and distribution of rubber particles in the fracture surfaces of CTBN/epoxy blends was studied with a Nikon optical microscope. To obtain microstructures showing the dispersion and distribution of particles, TSView that is a modular software specialized for image acquisition, processing and analysis was used. The fracture surface scrutiny of samples was achieved with image acquisition and image processing modules of the software. The average particle size was defined by measuring the sizes of 20 randomly chosen the rubber particles from acquired the microstructure images.

24. RESULTS AND DISCUSSION

24.1. Tensile Properties

The stress-strain curves of pure epoxy and CTBN/epoxy blends cured with anhydride-and amine-based curing agents are shown in Figure 4 and Figure 5, respectively. The significant tensile properties calculated from these curves are presented in Table 4 and Table 5. It is well known from the literature [10, 13, 15, 29, 30] that modification of epoxy with rubber decreases the tensile strength and elasticity modulus. Generally, this reduction is attributed to the low modulus of elasticity of the rubber phase and the reduction of the crosslink density of the epoxy during curing. As expected, the tensile strength and modulus of elasticity of pure epoxy and CTBN/epoxy blends cured with both curing agents decreased as the rate of CTBN addition by weight increased. As seen from Figure 4, the strain of epoxy increased with the addition of 7 wt.% and 10 wt.% CTBN/epoxy cured by anhydride-based agent.

The inclusion of 1 wt.% and 3 wt.% CTBN in the epoxy cured by amine-based agent led to increases in the strain, as shown in Figure 5. Moreover, the tensile strength and elasticity modulus of the CTBN/epoxy matrix slightly decreases with the addition of 1 wt.% and 3 wt.% CTBN, whereas a major increase in the strain was observed at the same sam-

ples. The ductility of the epoxy matrix can be achieved by reducing the crosslink density [31]. In addition, the crosslink density is affected by the epoxy equivalent weights of the epoxies. Pearson and Yee [32] examined the effect of the epoxy equivalent by varying the crosslink density of CTBN/epoxy blends cured with different DDS. They reported greater ductility with low cross-linked epoxies.

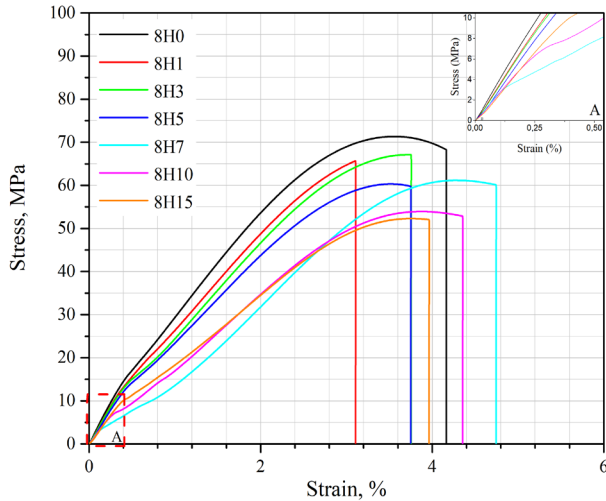


Figure 4. The stress-strain curves of pure epoxy and CTBN/epoxy blends cured by anhydride-based agent

Table 4. Tensile test results of CTBN/epoxy blends cured by anhydride-based agent

| Sample Codes | Tensile Strength (σ), MPa | Strain (ϵ), % | Modulus (E), GPa |
|--------------|------------------------------------|--------------------------|------------------|
| 8H0 | 72.58 \pm 3.21 | 4.06 \pm 0.58 | 3.00 \pm 0.05 |
| 8H1 | 66.80 \pm 2.98 | 3.16 \pm 0.34 | 2.92 \pm 0.04 |
| 8H3 | 64.23 \pm 4.08 | 3.93 \pm 0.22 | 2.88 \pm 0.01 |
| 8H5 | 63.08 \pm 2.87 | 3.84 \pm 0.17 | 2.69 \pm 0.05 |
| 8H7 | 63.77 \pm 1.26 | 4.37 \pm 0.97 | 2.52 \pm 0.03 |
| 8H10 | 54.13 \pm 5.33 | 4.26 \pm 0.55 | 2.33 \pm 0.05 |
| 8H15 | 52.99 \pm 2.29 | 3.88 \pm 0.15 | 2.08 \pm 0.05 |

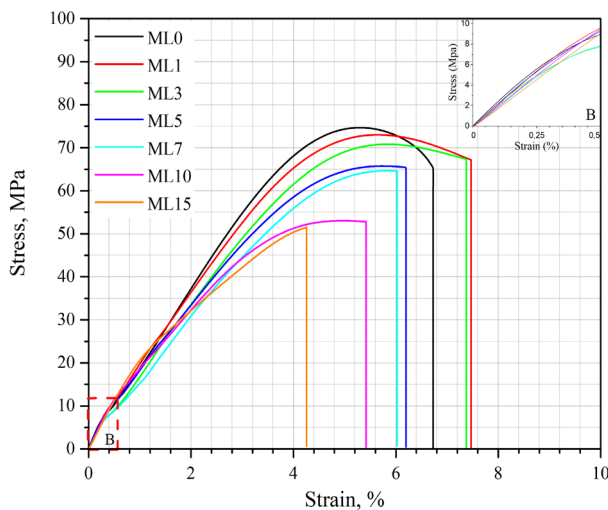


Figure 5. The stress-strain curves of pure epoxy and CTBN/epoxy blends cured by amine-based agent

Table 5. Tensile test results of CTBN/epoxy blends cured by amine-based agent

| Sample Codes | Tensile Strength (σ), MPa | Strain (ϵ), % | Modulus (E), GPa |
|--------------|------------------------------------|--------------------------|------------------|
| ML0 | 76.89 \pm 3.21 | 6.78 \pm 0.78 | 3.20 \pm 0.05 |
| ML1 | 75.91 \pm 1.09 | 7.54 \pm 1.99 | 3.05 \pm 0.01 |
| ML3 | 69.31 \pm 1.30 | 7.43 \pm 1.28 | 3.01 \pm 0.04 |
| ML5 | 64.99 \pm 0.69 | 6.28 \pm 1.77 | 2.97 \pm 0.02 |
| ML7 | 64.63 \pm 0.62 | 5.93 \pm 1.02 | 2.96 \pm 0.03 |
| ML10 | 52.86 \pm 1.36 | 5.57 \pm 0.75 | 2.94 \pm 0.05 |
| ML15 | 50.85 \pm 0.95 | 4.33 \pm 0.21 | 2.86 \pm 0.02 |

The ductility value increased more in ML1 and ML3 samples with lower CTBN content than the 8H7 and 8H10 samples with high CTBN content. It can be said that less crosslink density occurs at low rubber content in CTBN/epoxies produced with the amine-based agent. Compared to the CTBN/epoxy blends cured by anhydride- and amine-based agent, the blends cured by amine-based agent presents higher tensile strength, strain at break and elasticity modulus. The mechanical properties of the CTBN/epoxy blends cured by amine-based agent were found to be more consistent and higher compared to using an anhydride-based agents.

24.2. Fracture toughness

For pure epoxy and CTBN/epoxy blends cured with anhydride- and amine-based agents, fracture toughness (K_{IC}) and critical strain energy release rate (G_{IC}) are given in Figure 6 and Figure 7, respectively. The 8H0 and ML0 samples show low fracture toughness of 1.24 \pm 0.05 MPam^{1/2} and 0.80 \pm 0.30 MPam^{1/2} respectively. The addition of CTBN to the epoxy cured with the amine-based agent significantly increased the K_{IC} to 2.66 \pm 0.78 MPam^{1/2}, approximately 3.5 times. However, the enhancement in fracture toughness could not be achieved with CTBN/epoxy blends cured by the anhydride-based agent. The K_{IC} and G_{IC} values gradually decreased as CTBN was added to the anhydride/epoxy system. The presence of CTBN in the amine/epoxy system progressively increased fracture toughness but a decrease in K_{IC} was observed with the addition of more than 10% by weight of CTBN. The improvement in fracture toughness has been attributed to matrix shear banding [33], cavitation [34], and rubber fractures [35]. In addition, the stress dissipation between the rubber phase and polymer chains is improved due to the percolation of rubber particles in the epoxy matrix. This improvement restricts crack growth leading to increased fracture toughness [30]. As shown in Table 5, the improvements in fracture toughness of CTBN/epoxy blends were within 70-300% in literature studies [13, 14, 24, 26, 30, 36, 37].

The CTBN modification at rates ranging from 5-15% by weight has shown remarkable results in terms of increased toughness. When more than 15 wt.% CTBN is added to pure epoxy, it was seen a trend for a decrease in the toughness of the epoxy due to rubber agglomeration and phase inversion [38]. This demonstrates that the CTBN curing effect reveals its saturation and reactive rubber types as a liquid rubber

modifier are a useful method for obtaining polymer blends with high fracture toughness. The effects of rubber particle size on the toughness of both epoxy systems modified with CTBN were analyzed over fracture surface studies and toughening mechanisms and discussed in the subsequent section.

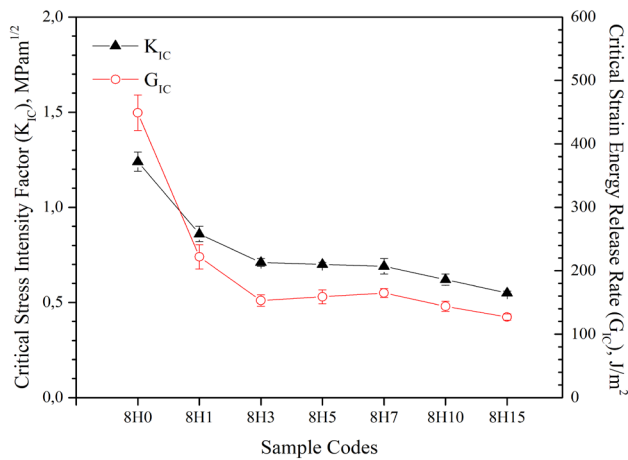


Figure 6. Fracture toughness (K_{IC}) and critical strain energy release rate (G_{IC}) of pure epoxy and its CTBN blends cured by anhydride-based agent

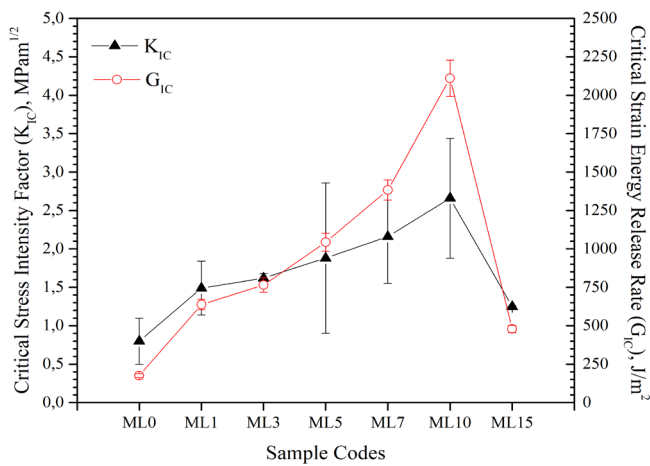


Figure 7. Fracture toughness (K_{IC}) and critical strain energy release rate (G_{IC}) of pure epoxy and its CTBN blends cured by amine-based agent

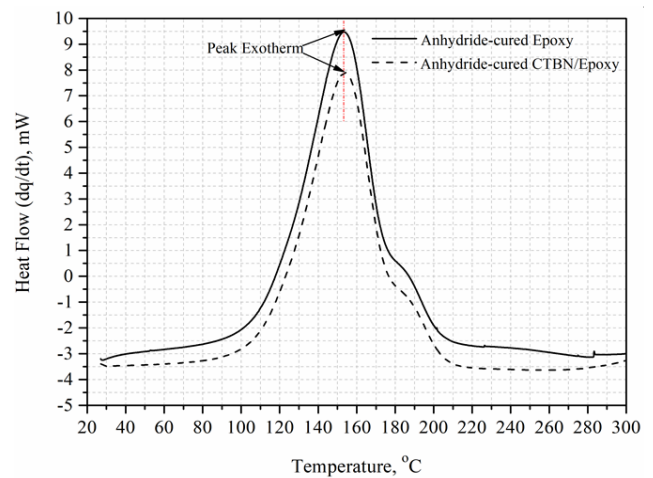
Table 5. The increases in fracture toughness of CTBN epoxy blends according to related literature

| References | Rubber Types | Rubber Content | Fracture toughness of pure epoxy, (K_{IC}), MPa $m^{1/2}$ | Fracture toughness of CTBN/epoxy blend, (K_{IC}), MPa $m^{1/2}$ | Increase, % |
|---------------------|--------------|----------------|---|---|-------------|
| Wang et al [13] | CTBN | 10 wt.% | 0.75 | 1.28 | 70.7 |
| Zhang et al [14] | CTBN | 10 wt.% | 0.77 | 1.47 | 90.8 |
| Tripathi et al [30] | CTBN | 15 wt.% | 0.90 | 3.6 | 300 |
| Chikhi et al [24] | ATBN* | 12.5 phr | 0.90 | 1.5 | 66.7 |
| Thomas et al [26] | HTPB* | 10 wt.% | 0.90 | 2.5 | 178 |
| Yahyaie et al [37] | ETPB* | 7.5 wt.% | 0.65 | 1.80 | 176 |
| Saleh et al [36] | LENR* | 5 wt.% | 0.80 | 3.1 | 288 |
| This study | CTBN | 10 wt.% | 0.80±0.30 | 2.66±0.78 | 202 |

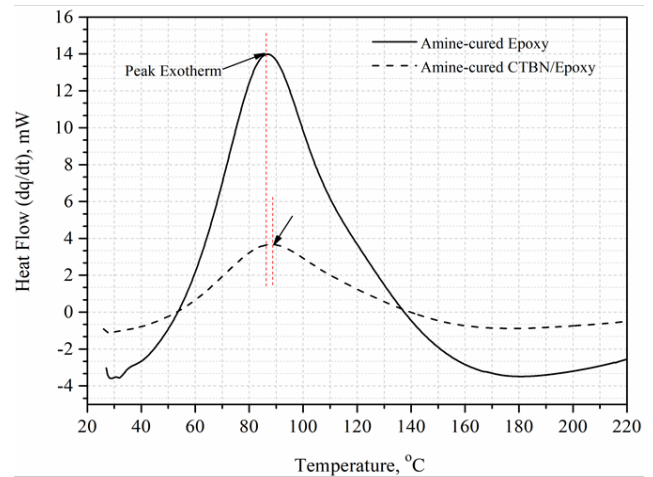
*Amine-terminated butadiene acrylonitrile (ATBN), Hydroxyl-terminated polybutadiene (HTPB), Epoxy-terminated polybutadiene (ETPB), Epoxidized natural rubber (LENR)

24.3. Effect of Rubber Particle Size

The growth of rubber particles in the epoxy matrix is affected by the curing reaction rate of the epoxy [23]. 10 wt.% CTBN modified epoxy blend were cured with both amine-based and anhydride-based agents and analyzed by DSC. Figure 8 shows the accelerating effect of 10 wt.% CTBN carboxyl groups on the curing of amine/epoxy and anhydride/epoxy. The presence of CTBN in the epoxy matrix shifts the peak exotherm. With the increased reaction rate, these peaks are shifted to lower temperatures, while are shifted to higher temperatures with decreasing reaction rates. It was found that the peak exotherm did not change in the CTBN/epoxy blend cured by anhydride-based agent.



(a)



(b)

Figure 8. DSC scanning of 10 wt.% CTBN modified and unmodified anhydride/epoxy (a) and amine/epoxy (b) systems

It was concluded that the reaction rate in the anhydride/epoxy system was not affected by the presence of CTBN. In the CTBN/epoxy blend cured by amine-based agent, the peak exotherm was shifted to a higher temperature. The presence of CTBN reduced the curing reaction rate in the amine-epoxy system. In the anhydride/epoxy system, the heat of polymerization slightly decreased. This confirms that the final reaction status for CTBN is not significantly affected by

the presence of CTBN. It was observed that the heat of polymerization was reduced dramatically with the addition of CTBN in the amine/epoxy system.

In CTBN/epoxy blends cured with anhydride- and amine-based agents, the average size (APS) of rubber particles formed by the phase separation mechanism [22] in the epoxy matrix was affected by the CTBN ratio by weight. Figure 9 shows the change of fracture toughness with APS according to the curing agent type. The APS of 8H1, 8H3 8H5, 8H7, 8H10 and 8H15 samples was obtained in about 0.10, 0.32, 0.53, 0.67, 0.95 and 0.37 micron, respectively. The APS increased up to 10 wt.% CTBN rate but decreased after this rate. Figure 10 shows that the rubber particle is homogeneously distributed in the matrix in the 8H1 and 8H5 samples compared to the 8H10 and 8H15 samples. The APS in 8H1 and 8H5 samples are close to each other. However, in the 8H10 and 8H15 samples, the rubber particles were dispersed in the matrix with different APS. The CTBN ratio in the samples cured by anhydride-based agent affected the size and distribution of the particles. However, it did not contribute to increasing the fracture toughness of the epoxy. As the weight of the CTBN ratio increased in anhydride/epoxy systems, fracture toughness gradually decreased.

The average particle sizes of ML1, ML3, ML5, ML7, ML10 and ML15 samples were obtained in about 0.12, 0.37, 0.61, 2.7, 7.3 and 4.5 micron, respectively. As with the samples cured by anhydride-based agent, APS first increased up to 10 wt.% CTBN, but a decrease was detected after this rate. Figure 11 shows that the rubber particles in ML1, ML5 and ML10 samples are homogeneously distributed into the matrix, except for the ML15 sample. The CTBN ratio in the samples cured by amine-based agent affected the size and distribution of the particles. In contrast to the samples cured by anhydride-based agent, the rise of the CTBN ratio contributed to increasing the fracture toughness of the epoxy. As the weight of the CTBN ratio increased in amine/epoxy systems except for the 15 wt.% CTBN ratio, fracture toughness gradually increased.

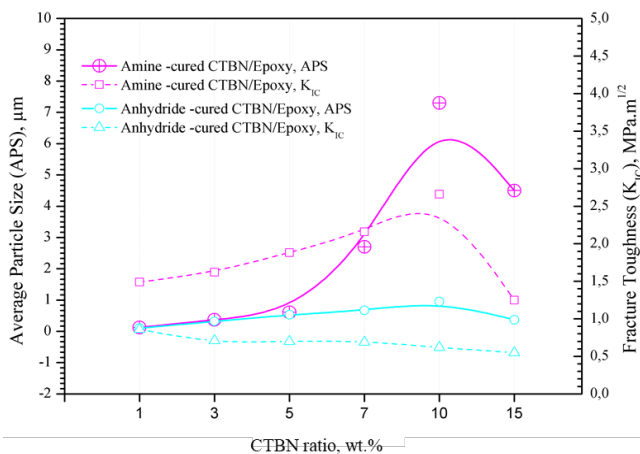


Figure 9. Comparison of average rubber particle size versus and fracture toughness versus CTBN ratios

The effect of CTBN modification had different results on

fracture toughness of anhydride/epoxy and amine/epoxy systems. The morphology of CTBN/epoxy blends cured at different temperatures is shown in Figure 10 and Figure 11. The APS of rubbers formed in CTBN/epoxy blends decreased as the isothermal curing temperature increased, and larger APS of rubber was observed in optical micrographs of epoxy mixtures cured at a lower temperature. The phase separation in epoxy/rubber blends occurs at a constant temperature. The rubber phase separation is initiated by the reaction caused curing agent. The phase separation has been reported to progress through the mechanism of nucleation and growth in the epoxy matrix [39, 40]. The curing rate in epoxy systems cured by anhydride-based agent is extremely high at elevated temperatures. A high curing temperature leads to a higher viscosity at the initiating of rubber phase separation. This leads to the diffusion difficulty required for the growth of rubber particles [41]. Therefore, in the anhydride/epoxy system, under the effect of a high curing temperature, the degree of phase separation was low, resulting in a low APS of the rubber formed. The rubber APS in epoxy/rubber blends is determined by the reaction kinetics in which the curing agent is involved. Therefore, the fracture behavior of epoxy/rubber blends depending on APS should be investigated experimentally.

25. CONCLUSIONS

The CTBN modification effect on the tensile and fracture properties of CTBN/epoxy blends cured by anhydride- and amine-based agent was investigated, and the results obtained from the study were summarized below:

1. The curing temperature is a necessary procedure for obtaining the optimal toughening effect of rubber, particularly in epoxies cured by anhydride-based agent. The anhydride/epoxy systems cured at high temperatures of 120 °C cause smaller rubber particle sizes compared to amine/epoxy systems cured at low curing temperatures of 90 °C. Therefore, the presence of the rubber phase, which has relatively small particle sizes in the epoxy matrix, decreases the fracture toughness.
2. The fracture toughness is dependent on CTBN rubber particle size and distribution.
3. The fracture toughness of CTBN/epoxy blends cured by anhydride-based agent decreased as CTBN addition increased in the epoxy matrix.
4. In fracture surfaces examination, large rubber particles have been found to be more effective than small particles in producing an enriched toughness effect.
5. The microstructure of the dispersed particles in the CTBN modified anhydride/epoxy system was not found to be significantly changed by different CTBN content.
6. In amine/epoxy systems cured at low curing temperatures, CTBN decreased the cross-linking reaction rate by shifting the exotherm peak to high temperature. This situa-

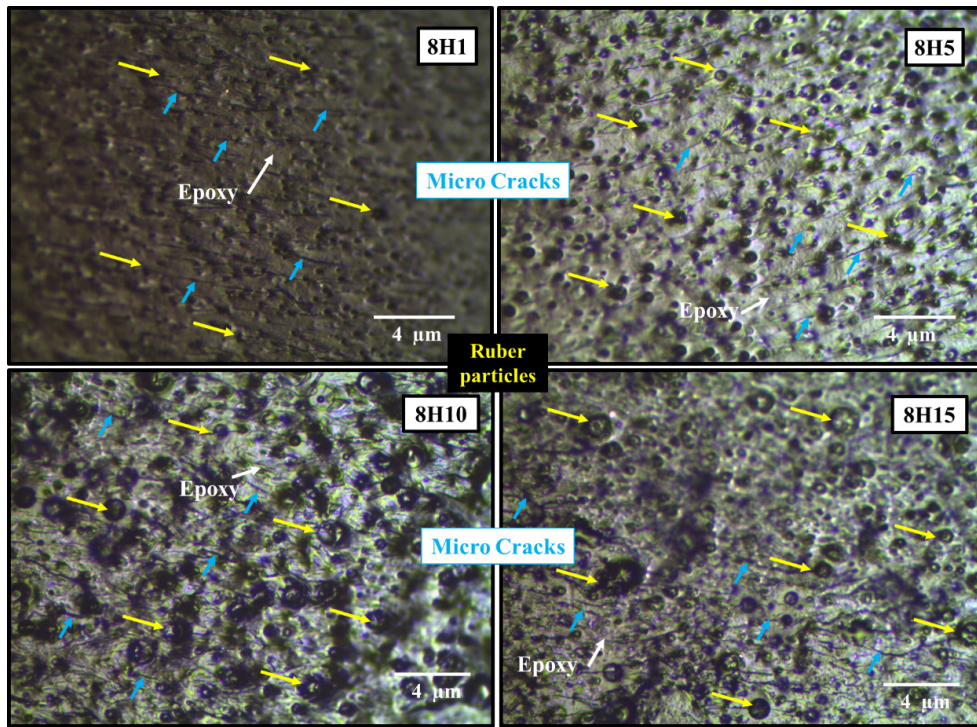


Figure 10. The optical microscope images of the fracture surfaces of CTBN/epoxy blends cured by anhydride-based agent.

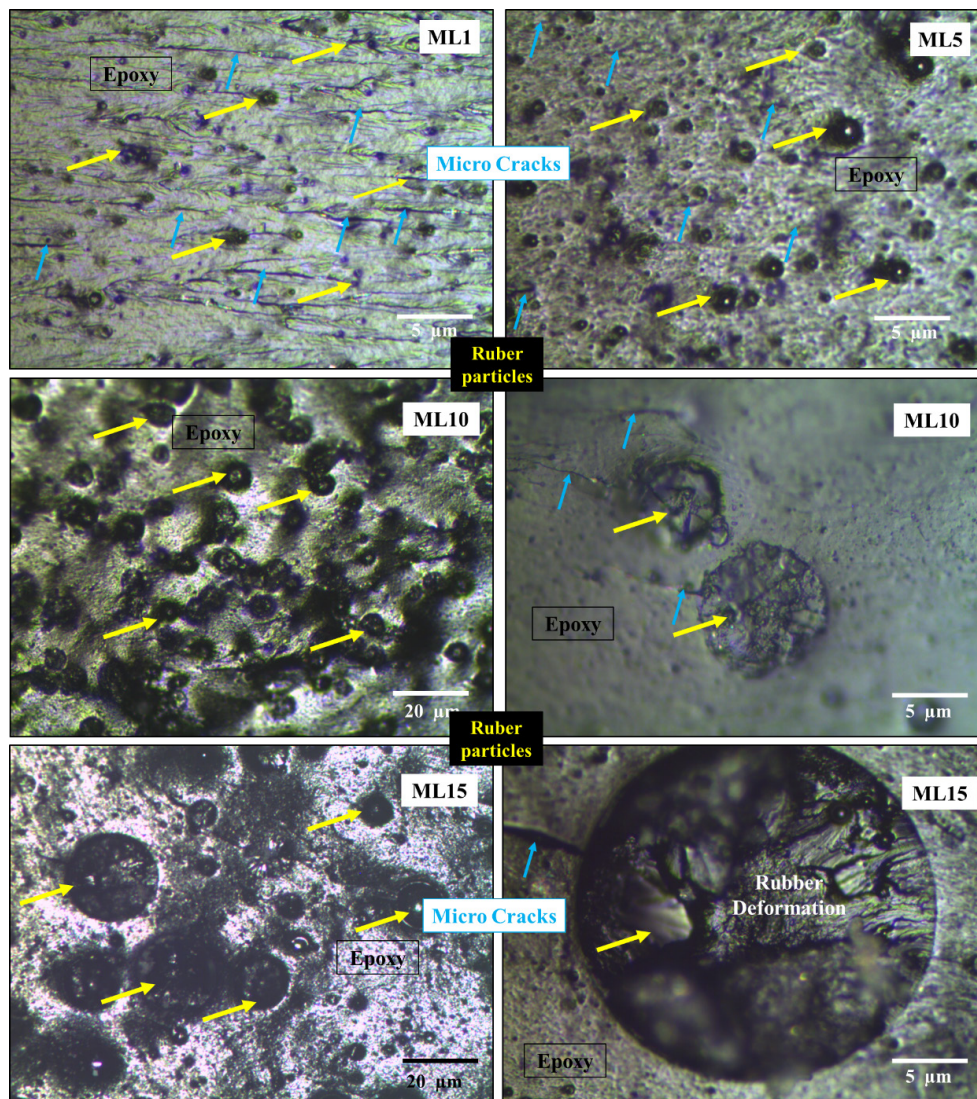


Figure 11. The optical microscope images of the fracture surfaces of CTBN/epoxy blends cured by amine-based agent.

tion had a positive effect on the growth of rubber particles. However, the exotherm peak did not shift in anhydride/epoxy systems, so this effect was not observed.

7. It was found from optic micrographs that the average size of rubber particles in the 10 wt% CTBN modified anhydride/epoxy system was 0.95 μm , which is smaller than the average size of rubber particles for the 10 wt.% CTBN modified amine/epoxy system (7.3 μm).

8. As the CTBN rate increased in anhydride/epoxy and amine/epoxy systems, a decrease in tensile strength and elasticity modulus was found. The deformation abilities of both epoxy systems were improved by the optimized addition of CTBN.

REFERENCES

- [1] Aslan, A., Salur, E. (2021). Düzcükoğlu H, Şahin ÖS, Ekrem M. The effects of harsh aging environments on the properties of neat and MWCNT reinforced epoxy resins. *Construction and Building Materials*. 272:121929.
- [2] Lee, H., Neville, K. (1967). *Handbook of epoxy resins*.
- [3] Lee, L.J. (1989). Modeling and computer simulation of reactive processing.
- [4] Thomas, R., Durix S, Sinturel C, Omonov T, Goossens S, Groeninckx G, et al. (2007). Cure kinetics, morphology and miscibility of modified DGEBA-based epoxy resin—Effects of a liquid rubber inclusion. *Polymer*;48(6):1695-710.
- [5] Gibson, R.F. (2016). *Principles of composite material mechanics*: CRC press.
- [6] Ebrahimabadi Y, Mehrshad M, Mokhtary M, Abdollahi M. (2021). Studies of thermal, mechanical properties, and kinetic cure reaction of carboxyl-terminated polybutadiene acrylonitrile liquid rubber with diepoxy octane. *Journal of Applied Polymer Science*. 38(9):49932.
- [7] Guild F, Kinloch A. (1995). Modelling the properties of rubber-modified epoxy polymers. *Journal of materials science*. 30(7):1689-97.
- [8] Huang Y, Kinloch A. (1992) Modelling of the toughening mechanisms in rubber-modified epoxy polymers. *Journal of materials science*. 27(10):2753-62.
- [9] Jung H-S, Park Y, Nah C-W, Lee J-C, Kim K-Y, Lee CS. Evaluation of the Mechanical Properties of Polyether Sulfone-Toughened Epoxy Resin for Carbon Fiber Composites. *Fibers and Polymers*.1-12.
- [10] Kinloch AJ, Guild FJ. (1996). Predictive modeling of the properties and toughness of rubber-toughened epoxies. ACS Publications.
- [11] Ramos VD, da Costa HM, Soares VL, Nascimento RS. (2005). Hybrid composites of epoxy resin modified with carboxyl terminated butadiene acrylonitrile copolymer and fly ash microspheres. *Polymer Testing*. 24(2):219-26.
- [12] Riew CK, Siebert A, Smith R, Fernando M, Kinloch A. (1996) Toughened epoxy resins: preformed particles as tougheners for adhesives and matrices. ACS Publications.
- [13] Wang F, Drzal LT, Qin Y, Huang Z. (2016). Enhancement of fracture toughness, mechanical and thermal properties of rubber/epoxy composites by incorporation of graphene nanoplatelets. *Composites Part A: Applied Science and Manufacturing*. 87:10-22.
- [14] Zhang J, Deng S, Wang Y, Ye L. (2016). Role of rigid nanoparticles and CTBN rubber in the toughening of epoxies with different cross-linking densities. *Composites Part A: Applied Science and Manufacturing*. 80:82-94.
- [15] Pearson R, Yee A. (1989). Toughening mechanisms in elastomer-modified epoxies. *Journal of materials science*. 24(7):2571-80.
- [16] Pearson RA, Yee AF. (1986). Toughening mechanisms in elastomer-modified epoxies. *Journal of materials science*. 21(7):2475-88.
- [17] Yee AF, Pearson RA. (1986). Toughening mechanisms in elastomer-modified epoxies. *Journal of materials science*. 21(7):2462-74.
- [18] Riew CK. (1989). *Rubber-toughened plastics*: American chemical society.
- [19] Ignatova T, Kosyanchuk L, Todosiychuk T, Nesterov A. (2011). Reaction-induced phase separation and structure formation in polymer blends. *Composite interfaces*. 18(3):185-236.
- [20] Mathew VS, Sinturel C, George SC, Thomas S. (2010). Epoxy resin/liquid natural rubber system: secondary phase separation and its impact on mechanical properties. *Journal of materials science*. 45(7):1769-81.
- [21] Moschiar S, Riccardi C, Williams R, Verchere D, Sautereau H, Pascault J. (1991). Rubber-modified epoxies. III. Analysis of experimental trends through a phase separation model. *Journal of applied polymer science*. 42(3):717-35.
- [22] Verchere D, Sautereau H, Pascault J, Moschiar S, Riccardi C, Williams R. (1990). Rubber-modified epoxies. I. Influence of carboxyl-terminated butadiene-acrylonitrile random copolymers (CTBN) on the polymerization and phase separation processes. *Journal of Applied Polymer Science*. 41(3-4):467-85.
- [23] Wise C, Cook WD, Goodwin AA. (2000). CTBN rubber phase precipitation in model epoxy resins. *Polymer*. 41(12):4625-33.
- [24] Chikhi N, Fellahi S, Bakar M. (2002) Modification of epoxy resin using reactive liquid (ATBN) rubber. *European Polymer Journal*. 38(2):251-64.
- [25] Ratna D. (2001). Phase separation in liquid rubber modified epoxy mixture. Relationship between curing conditions, morphology and ultimate behavior. *Polymer*. 42(9):4209-18.
- [26] Thomas R, Yumei D, Yuelong H, Le Y, Moldenaers P, Weimin Y, et al. (2008). Miscibility, morphology, thermal, and mechanical properties of a DGEBA based epoxy resin toughened with a liquid rubber. *Polymer*. 49(1):278-94.
- [27] Gledhill R, Kinloch A, Yamini S, Young R. (1978). Relationship between mechanical properties of and crack propagation in epoxy resin adhesives. *Polymer*. 19(5):574-82.
- [28] Shan H-Z, Chou T-W. (1995). Transverse elastic moduli of unidirectional fiber composites with fiber/matrix interfacial debonding. *Composites Science and Technology*. 53(4):383-91.
- [29] Dadian A, Rahnama S, Zolfaghari A. (2020). Experimental study of the CTBN effect on mechanical properties and mode I and II fracture toughness of a new epoxy resin. *Journal of Adhesion Science and Technology*. 34(22):2389-404.
- [30] Tripathi G, Srivastava D. (2008). Studies on the physico-mechanical and thermal characteristics of blends of DGEBA epoxy, 3, 4 epoxy cyclohexylmethyl, 3', 4'-epoxycyclohexane carboxylate and carboxyl terminated butadiene co-acrylonitrile (CTBN). *Materials Science and Engineering: A*. 496(1-2):483-93.
- [31] Deb P, Ratna D, Chakraborty B. (1997). Carboxyl terminated poly(ethylene glycol) adipate modified epoxy network. I. Synthesis and thermal characterization. *Journal of Polymer Materials(Netherlands)*. 14(2):189-94.

- [32] Pearson R, Yee Y. (1983). *Polymer Materials Sci. Preprints*, Amer Chemical Soc.186:316.
- [33] Kim JK, Datta S. (2013). Rubber-thermoset blends: micro and nano structured. *Advances in elastomers I*: Springer. p. 229-62.
- [34] Ratna D. (2007). *Epoxy composites: impact resistance and flame retardancy*: iSmithers Rapra Publishing.
- [35] Najjipoor M, Haroonabadi L, Dashti A. (2018). Assessment of failures of nitrile rubber vulcanizates in rapid gas decompression (RGD) testing: Effect of physico-mechanical properties. *Polymer Testing*. 72:377-85.
- [36] Yahyaie H, Ebrahimi M, Tahami HV, Mafi ER. (2013). Toughening mechanisms of rubber modified thin film epoxy resins. *Progress in Organic Coatings*. 76(1):286-92.
- [37] Saleh AB, Ishak ZM, Hashim A, Kamil W, Ishiaku U. (2014). Synthesis and characterization of liquid natural rubber as impact modifier for epoxy resin. *Physics Procedia*. 55:129-37.
- [38] Kinloch A, Hunston D. (1987). Effect of volume fraction of dispersed rubbery phase on the toughness of rubber-toughened epoxy polymers. *Journal of materials science letters*. 6(2):137-9.
- [39] Chen J-P, Lee Y-D. (1995). A real-time study of the phase-separation process during polymerization of rubber-modified epoxy. *Polymer*. 36(1):55-65.
- [40] Kiefer J, Hilborn J, Hedrick J. (1996). Chemically induced phase separation: a new technique for the synthesis of macroporous epoxy networks. *Polymer*. 37(25):5715-25.
- [41] Kim DS, Kim SC. (1994). Rubber modified epoxy resin. II: Phase separation behavior. *Polymer Engineering & Science*. 34(21):1598-604.



Static Analysis of Trailers with Demountable Chassis

Tuğba Gedik¹ , Mehmet Vurgun² , Banu Özkeser^{3*} , Erhan Biçer⁴ 

¹Koluman Otomotiv Endüstri A.Ş. Ar-Ge Merkezi Mersin, Turkey

Abstract

Today, trailers are the most used vehicles in intercity and international road transport. There are serious difficulties in the production processes and post-production shipments of these vehicles. Trailer chassis are generally produced in welded structures. In this study, the trailer chassis produced in welded structure was transformed into a bolted structure. A nonlinear finite element model was created and static analyzes of the demountable chassis trailer have been made. In these analyzes, stress and deformation data on the chassis part of the trailer were observed. It is concluded that the deformation of the chassis under these loads is at an acceptable level. As a result, it has been shown that welded structures in trailer chassis can be transformed into bolted structures and there is no problem in terms of safety.

Keywords: Trailer, Finite Element Method, Demountable Chassis, Traverse

26. INTRODUCTION

Road transport constitutes an important part of the logistics industry in the world. Although different vehicles are used, trailers are generally used in road transport. Trailer; It is a road vehicle that is pulled by the truck and connected with a connection device designed according to the characteristics of the load to be transported. It is commonly used for the transport of goods and materials. The most important component of these vehicles carrying the load is the chassis consisting of a steel construction structure. The production process of the trailer chassis, which involves a large amount of welding, poses difficulties for trailer manufacturers in terms of both cost and time. Besides, manufacturers have problems in delivering the trailer chassis produced as a result of the welding process to the customer. In addition, damage to the structure caused by possible accidents in the welded structure increases the costs of maintenance repair and spare parts. Considering the disadvantages of the welded structure, it is thought that a modular chassis can solve these problems.

Bolted connections occupy the most important place in fasteners due to their removable or interchangeable features[1,2]. In terms of mechanical elements, considerable studies have been carried out on the subject in the post-2000s period[3–8], as many academic resources have come to the present day[9–14]. Since bolt safety is extremely important, especially when exposed to static and dynamic loads, the work in this area should be adequately examined.

In the study of Jianhua Liu et al., The dynamics of a bolted connection under torsion were examined both experimentally and numerically[15]. In these studies, it has been revealed that there are relative shifts between the clamped parts and between the contact thread.

The stiffness of the connection, which is one of the most important issues in the design of bolted connections, was studied by M. Özkan and K. Dündar[2]. They presented a general solution for element stiffness and pressure propagation angles for bolting the same type of materials and bolting different types of materials and developed an artificial neural network model in this regard. In this study of M. Özkan and K. Dündar, the notch factor required for the strength calculations of bolted connections exposed to variable loadings was taught to the artificial neural network and it was stated that the notch factor value was determined by the user without the need for any table or equation.

On the other hand, in the study on the forces coming to the fasteners in automotive chassis assemblies and the effects of these forces[16], the tightening torque values that form the basis of the joining processes in the chassis joints and the lower and upper limits expressing the tolerances to be addressed in the application of these values were determined within a calculation method. In order to see the accuracy of the method and calculated values, critical connections on a vehicle that was sent to a 30,000 km long-distance test on all road conditions and the route were examined. As a result of the study, it was stated that an approximate calculation was

* Corresponding author
Email: banuozkeser@gmail.com



put forward in which road test costs were eliminated.

The contact stresses occurring in the bolt-nut connection system were studied by Kubilay Aslantaş et al[17]. A 3D model was developed for the contact stresses occurring in the bolt-nut system exposed to axial load and the study was detailed with the finite element analysis method. It is concluded that the stress values occurring at the thread bottoms of the bolt under the same loading conditions are higher for the nut model and the maximum stresses occur at the thread bottoms where the nut and bolt contact occurs first.

In another study, the behavior of multiple bolt connections under shear and bending loads were determined by Filiz İ.H. and Kanber B.[18]. In the study, a symmetrical connection with 6 bolts was considered and subjected to shear and bending loads. In analytical solutions, the elements tightened by the bolts were assumed to be rigid and their effect on bolt deformations was considered to be zero. Two different solutions are made in finite element solutions. In the first, as in analytical solutions, all the elements tightened by the bolts were accepted as rigid and their compatibility with analytical solutions was checked. In the second solution, bolts and connected elements are considered elastic and the differences with the previous solutions have been investigated. Thus, the effect of the rigid assumption in analytical solutions on the results is shown. Infinite element solutions, the preloading effect in connections is also investigated. It has been shown that assuming the elements in analytical solutions to be rigid causes an error of 20% in the results. Also, it has been reported that the tightening of the bolts shifts the center of rotation upwards.

In a study on the risk of loosening of bolts under vibration[19], the loosening mechanism was modeled with numerical simulation method, an experiment set was prepared within the parameters that were seen to affect the process, and simulations were run. In this study, in which regression analysis and genetic programming were compared, it was reported that the genetic programming method gave more effective results.

Since the transition from welded structure to the bolted structure is in question in demountable chassis studies, a literature study is given on the issues that should be considered in the use of bolts in this section. In the trailer area, there are of course studies such as the use of composite materials and ultra-strong steel to lighten[20]. Besides, life tests are also available, especially in welded structures[21].

Within the scope of the demountable chassis trailer manufacturing, it is essential to transform a welded structure into a bolted structure. On this occasion, the most fundamental content of the study is to reduce the assembly times arising from the welding process, eliminate structural disadvantages arising from the stresses, and most importantly, the transportation of more than one product at a time in terms of logistics. Considering their mounting capabilities, weld-

ed and bolted structures have advantages and disadvantages compared to each other. The especially bolted assembly stands out as a fastening technique that does not require qualified personnel, is fast, easier to control and repair, and is not affected by environmental weather conditions during assembly.

In this study, the trailer chassis produced in welded structure was transformed into a bolted structure. A nonlinear finite element model was created and static analyzes of the demountable chassis trailer were made. In these analyzes, stress and deformation data on the chassis part of the trailer were observed. It was concluded that the deformation of the chassis under these loads was at an acceptable level. As a result, it has been revealed that the welded structures on the trailer chassis can be transformed into bolted structures and there are no problems in terms of safety.

27. MATERIAL AND METHODS

In Trailer Research & Development processes, design and design verification capabilities are required. Vehicles are constantly under dynamic and static loads and the transportation time of this load is very long. For this purpose, the structure should be examined in detail using the finite element method in the development processes. Static analysis, dynamic analysis, fatigue analysis, thermal analysis, and modal analysis are at the top of the analysis performed by applying the finite element method. In this study, static and analyzes of the demountable chassis trailer under different loading conditions were run to examine and simulate large deformations, high-stress rates, and complex contact interactions that occur in a short time. The commercial finite element program ANSYS Workbench / Static Structural and Modal analysis programs were used for these analyzes.

27.1. Numerical Model

The model used in the study was created by converting the already existing welded trailer chassis into a demountable chassis. The demountable chassis was designed by the Koluman Automotive Industry R&D department. The detailed model is shown in Figure 1. The analysis model is modeled as symmetrical (half) because the geometry and loading have a symmetrical structure (both physically and geometrically symmetrical). Thus, the solution time was gained. The analysis model was prepared by simplifying it with SpaceClaim Direct Modeler (SCDM) included in the ANSYS software. The detailed model is shown in Figure 2.

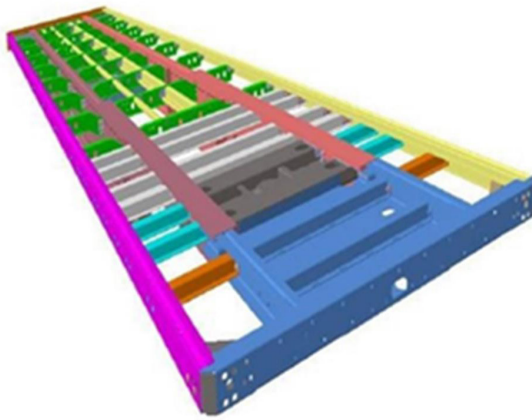


Figure 1. Demountable trailer chassis model



Figure 2. Demountable trailer chassis analysis model (half)

The simplification process is the deletion of parts, sharp corner chamfers and relatively small fillets, fasteners such as bolts and nuts that have no effect on the analysis or are negligible, and the negligible thin sheet metal parts are transformed into 2-dimensional surface elements. This process is done to obtain fast solutions by creating a small number of numerical solution elements. Instead of the deleted bolts in the system, one-dimensional beam elements were placed to represent the bolts. With these elements, shear and axial forces can be read on the analysis result. In this context, various modifications have been made to the holes where the bolts are connected. In order to obtain a more realistic solution, the surfaces of the shell elements are divided to the required size (twice the diameter) to create the cone effect that the bolts create. The same geometry was used in all analyzes.

27.2. Material Selection

The raw material generally used in the trailer chassis is S355J2. The number in the name of the structural steel, namely 355 yield strength. It shows the maximum load in MPa that does not end with plastic deformation. S355J2 (St-52) steel is a readily weldable low carbon manganese steel with good impact resistance (including in sub-zero temperatures). This material is commonly supplied in untreated or normalized conditions. The machinability of this material is similar to that of mild steel. The chemical composition and mechanical features of S355J2 (St-52) material are shown in Tables 1 and 2.

Table 1. S355J2 (St-52) Mechanical Features

| S355J2 (St-52) Mechanical Features | | | | |
|------------------------------------|------------------------------|-------------------|-----------------------|----------------------|
| Material | Density [kg/m ³] | Poisson Ratio [-] | Elastic Modulus [GPa] | Yield Strength [MPa] |
| St-52 / S355 | 7850 | 0.3 | 210 | 355 |

Table 2. S355J2 (St-52) Mechanical Features

| S355J2 (St-52) Chemical Composition | | | | | | | |
|-------------------------------------|--------------|--------|--------|---------|-------------|------------|------------|
| C | Si | Mn | P | S | Ni | Cr | Fe |
| 0.2 % (max) | 0.55 % (max) | 1.60 % | 0.02 % | 0.025 % | 0.3 % (max) | 0.3% (max) | remain-der |

27.3. Meshing Model

In order to obtain accurate results in analysis, it is necessary to choose the appropriate mesh method. A suitable mesh structure was created in the simplified and ready-for-analysis model. A total of 688,266 nodes and 667,636 items were used in the created solution network. This network structure is shown in Figure 3.



Figure 3. The mesh structure of the analyses model

28. RESULTS AND DISCUSSION

Since the part exposed to the greatest load on the demountable chassis is the I-profile, the analysis was applied to this profile. The analysis results are given in detail below. In the analysis, 15000 N loads were applied to both sides of the connections. In addition to these loads, standard gravity is also included in the analysis. These boundary conditions are shown in Figures 1 and 2.

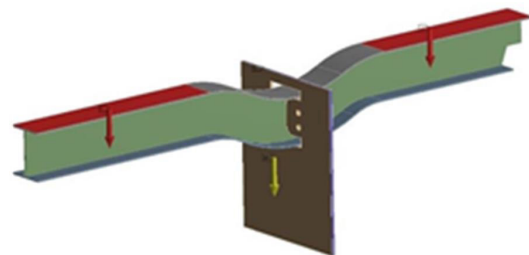


Figure 4. The welding boundary conditions

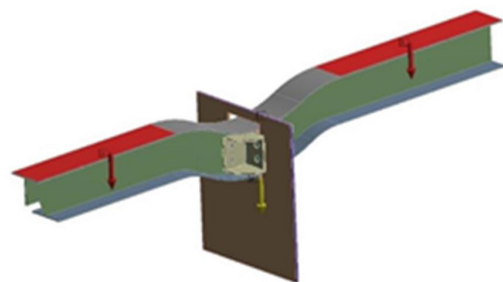


Figure 5. The assembly boundary conditions

As a result of the loads applied in the analysis, the stress in the welded structure I-profile traverse is 404 MPa and the deformation is 20 mm. The stress resulting from the loads applied on the demountable I-profile traverse is 420 MPa and the deformation is 10 mm. According to the results of this analysis, while the stress at the connection points increased by 3.96%, the amount of deformation decreased by 50 %. Stresses and deformations of structures are shown in Figures 6, 7, 8, and 9.

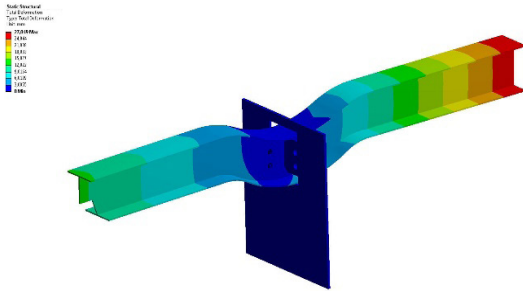


Figure 4. The welding boundary conditions

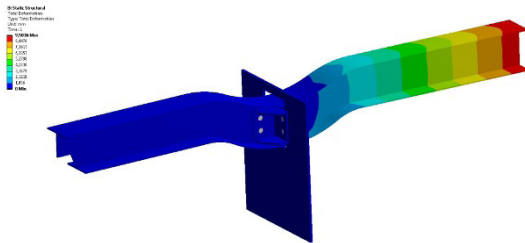


Figure 7. The assembly deformation

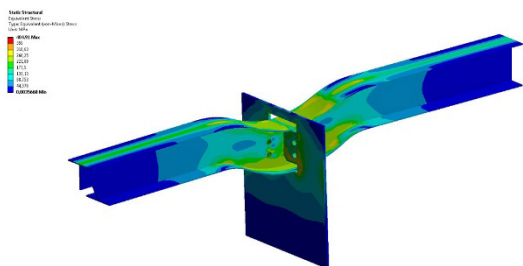


Figure 8. The welding stress

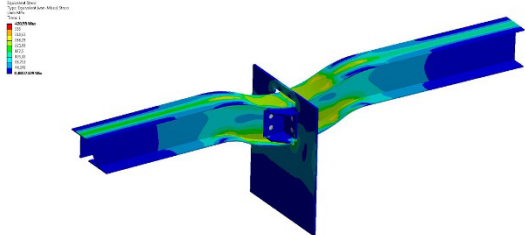


Figure 9. The assembly stress

In addition to the comparisons of the I-profile traverses given above, the U-profile traverse analyzes, which are the main form, were also performed. In the following table, the stress and deformation comparisons of welded structure U-profile traverse, welded structure I-profile traverse, and assembled structure I-profile traverse are given.

As can be seen in Table 3, as a result of the transformation of the welded structure U-profile traverse to the assembled structure I-profile traverse, the deformation decreased by approximately 52% and the stresses increased by 18%. It is

evaluated within the framework of the safety factor that this increase in stress will not cause any problems in terms of safety.

Table 3: Stress and Deformation According to Travers Type

| Types of Traverse Structure | Stress | Deformation |
|--|---------|-------------|
| The Welded Structure U-profile Traverse | 355 MPa | 19 mm |
| Welded Structure I-profile Traverse | 404 MPa | 20 mm |
| The Assembled Structure I-profile Traverse | 420 MPa | 10 mm |

When the data obtained are evaluated in terms of production;

- It has been observed that the assembly time of the trailer chassis produced with the assembled I-profile traverse structure is 10% less than the assembly time of the chassis produced with the welded U-profile traverse structure.
- Due to the use of traditional production methods, it has been observed that the cost of the chassis produced with the assembled I-profile traverse structure is lower than the cost of the chassis produced with the welded U-profile traverse structure.
- While the chassis produced with welded U-profile traverse structure is a single piece, there is a problem in transportation, it has been observed that the chassis produced with the assembled I-profile traverse structure provides ease of transportation since it has three parts by demountability.

29. CONCLUSION

In this study, the welded U-profile traverse structure was transformed into an assembled I-profile traverse structure. As a result of the study, it was seen that the assembled structure has a 51% advantage over the welded structure in terms of deformation. However, it was observed that the assembled structure did not cause any problems in terms of safety in the stress data obtained. It is predicted that it will be widely used in the coming years due to its advantages such as short assembly time, low production cost, ease of transportation, and demountability.

REFERENCES

- [1] Al, T.F.L. et., (1992). Member Stiffness and Bolt Spacing of Bolted Joints. Winter Annual Meeting of the American Society of Mechanical Engineers, Anaheim: Winter Annual Meeting of the American Society of Mechanical Engineers p. 63–72.
- [2] Dunder, K., Ozkan, M.T., (2005). Civatalı Bağlantıların Eleman Dirençliliğinin Sonlu Elemanlar Yöntemi Ve Yapay Sinir Ağları Sistemi İle Belirlenmesi. Teknoloji. 8(1): 33–41.
- [3] Shigley, J.E., Mitchell, L.D., (1983). "Bolted Joint", Mechanical engineering design. Newyork: McGraw Hill Inc.
- [4] Lehnhoff, T.F., Ko, K. II., McKay, M.L., (1994). Member Stiffness and Contact Pressure Distribution of Bolted Joints. Journal of Mechanical Design. 116(2): 550–7. doi: 10.1115/1.2919413.
- [5] Wileman, J., Choudhury, M., Green, I., (1991). Computation of member stiffness in bolted connections. Journal of Mechanical Design, Transactions of the ASME. 113(4): 432–7. doi: 10.1115/1.2912801.

- [6] Akkurt, M., (1986). "Civata bağlantıları", Makina elemanları". İstanbul: Birsen Kitabevi.
- [7] Filiz, İ., H., Akbolat, A., Güzelbey, İ.H., (1996). Stiffness of bolted members. Turkish Journal of Engineering and Environmental Sciences. 20: 273–9.
- [8] Englund, R.B., Johnson, D.H., (1997). Finite element analysis of a threaded connection compared to experimental and theoretical research. Journal of Engineering Technology. 14(2): 42–7.
- [9] Ibrahim, R.A., Pettit, C.L., (2005). Uncertainties and dynamic problems of bolted joints and other fasteners. Journal of Sound and Vibration. 279(3–5): 857–936. doi: 10.1016/j.jsv.2003.11.064.
- [10] Olsson, J., Sandlund, P., (2008). Form the Design Basis for Screw Joints. The Lulea University of Technology, (2008).
- [11] Oldfield, M., Ouyang, H., Mottershead, J.E., (2005). Simplified models of bolted joints under harmonic loading. Computers and Structures. 84(1–2): 25–33. doi: 10.1016/j.compstruc.2005.09.007.
- [12] Ouyang, H., Oldfield, M.J., Mottershead, J.E., (2006). Experimental and theoretical studies of a bolted joint excited by a torsional dynamic load. International Journal of Mechanical Sciences. 48(12): 1447–55. doi: 10.1016/j.ijmecsci.2006.07.015.
- [13] Jiang, Y., Zhang, M., Lee, C.H., (2003). A study of early stage self-loosening of bolted joints. Journal of Mechanical Design, Transactions of the ASME. 125(3): 518–26. doi: 10.1115/1.1586936.
- [14] Karim, Y., Blanzé, C., (2014). Vibration reduction of a structure by design and control of a bolted joint. Computers and Structures. 138: 73–85. doi: 10.1016/j.compstruc.2014.02.009.
- [15] Liu, J., Ouyang, H., Feng, Z., Cai, Z., Mo, J., Peng, J., et al., (2019). Dynamic behaviour of a bolted joint subjected to torsional excitation. Tribology International. 140: 105877. doi: 10.1016/j.triboint.2019.105877.
- [16] Gürsel, K.T., Yarkin, T., (2014). Otomobillerin Şasi Montajlarında Civata Sıkma Limitlerinin Saptanması. Journal of Polytechnic. 17(4): 193–202.
- [17] Aslantas, K., I., U., Tasgetiren, S., (2004). Civata-Somun bağlantı sistemlerinde temas gerilmelerinin üç boyutlu analizi. Makine Teknolojileri Elektronik Dergisi. (2): 50–5.
- [18] Filiz, İ., H., Kanber, B., (2007). Çoklu Civatalı Bağlantıların Kesme Ve Eğme Yükleri Altında İncelenmesi. Çoklu Civatalı Bağlantıların Kesme Ve Eğme Yükleri Altında İncelenmesi, ISPARTA: XV. Ulusal Mekanik Kongresi, 03-07 Eylül 2007.
- [19] Bıyık, A., Baykasoglu, A., Erbil, E., Ince, U., (2016). Civatalı Bağlantıların Titreşim Altında Gevşemesinin Genetik Programlama Ve Regresyon Analizi İle Tahmini. Bursa: 8. Otomotiv Teknolojileri Kongresi.
- [20] Bhushan, V., Yadav, S.D., (2018). Design and analysis of 30 ton trailer chassis frame to reduce pollution by decreasing the emission through weight reduction using advanced lightweight material. International Journal of Mechanical Engineering and Technology. 9(6): 705–22.
- [21] Tello, L., Castejon, L., Malon, H., Valladares, D., Luque, P., Mantaras, D.A., et al., (2020). Development of a fatigue life prediction methodology for welded steel semi-trailer components based on a new criterion. Engineering Failure Analysis. 108: 104268. doi: 10.1016/j.engfailanal.2019.104268.



Estimating Global Solar Radiation from Empirical Models: An Application

Özgür Ballı^{1,2*} 

¹Ministry of National Defence (MND), Aeronautical Engineer at 1st Air Maintenance Factory Directorate (1.HBFM), Eskisehir, Turkey

²Eskisehir Osmangazi University, Graduate School of Natural and Applied Sciences, Batı Meselik Campus, Eskisehir, Turkey

Abstract

Many applications and regions of observe require information on solar radiation. Several mathematical models were proposed to forecast worldwide sun radiation in Turkey and different international locations to do this. Some of meteorological information, along with worldwide sun radiation, sunshine period, temperature, air pressure, wind speed, and relative humidity, among January 1, 2011 and December 31, 2014 were measured. These outcomes have been used to create mathematical models to degree the monthly mean daily global solar radiation at the horizontal surface over Eskisehir. The new analytical models have been tested the usage of 9 generally used statistical techniques, along with the relative percentage error (E), the mean percentage error (MPE), the mean absolute percentage error (MAPE), the sum of squares of relative errors (SSRE), the relative standard error (RSE), the mean bias error (MBE), the root mean square error (RMSE), the t-statistic method (t-stat) and coefficient of determination (R^2). The new version is predicted to advantage all people concerned or interested by the layout and observe of sun strength packages which include sun furnaces, timber drying, stoves, concentrating collectors, indoors illumination, and thermal load reading of buildings, along with sun engineers, architects, agriculturists, hydrologists., photovoltaics, and meteorological forecasting.

Keywords: Global solar radiation, empirical models, statistical analysis, Eskisehir city.

30. INTRODUCTION

In this period, the increased decline of power supplies, growing power consumption, and lack of ecological values necessitate a direct response. As the maximum important power fuel, sun power has been part of the answer to the world's power problems. Solar radiation information is wanted for the use, preparation, and creation of sun strength plant life as it tells us how a good deal power moves the earth. Owing to the complexity of sun radiation calculations in phrases of preliminary and restore costs, information on sun radiation is handiest to be had in some geographic locations. As a result, sun power modeling strategies have become an increasing number of applicable because the marketplace for sun power software design, overall performance assessment, and enhancement increases [1-2]. For the improvement and operation of the inexperienced power program, excessive high-satisfactory sun radiation information is wanted to reduce monetary risks. To now, the maximum dependable information have come from a combination of information from ground solar measurement stations and information extracted from satellite TV for PC images [3, 4].

For correct evaluation of sun energy capacity, the use of empirical models is vital for the improvement of sun energy generation and the long-time period survival of natural resources [5]. Long-time period worldwide sun radiation records and different meteorological parameters are regularly used to set up mathematical models for month-to-month implies every day worldwide sun at the horizontal surface prediction. The models are categorized into 3 categories: (1) Only function of sunshine duration; (2) Function of sunshine duration as well as relative humidity and ambient temperature; (3) Independent of sunshine duration and function of relative humidity, ambient temperature and its maximum and minimum.

Several empirical models have been suggested to predict the global solar radiation over Turkey and other countries. Khorasanizadeh and Mohammadi [6] used the eleven empirical models to test for prediction of monthly mean daily global solar radiation over six major cities of Iran, named Isfahan, Karaj, Mashhad, Shiraz, Tabriz and Tehran. Yaiche et al. [7] have used the hourly sunshine duration to develop a global solar irradiation map for all types' of the sky. Robaa [8] reviewed and tested the validity of the existing models

* Corresponding author
Email: balli07balli@yahoo.com



available for computing the monthly average daily global radiation on a horizontal surface over Egypt. Manzano et al. [9] investigated the performance of Angstrom-Prescott linear equation models to estimate the global solar radiation on horizontal surface at daily and monthly mean daily time over Spain. The existing solar radiation models were analyzed with hourly global solar radiation data measured from January 2009 to December 2011 on Jiading Campus, Tongji University by Yao et al. [10]. The results of this study showed that the existing models established in the form of a Gaussian equation were comparatively accurate, followed by models adjusted or modified from the Whillier – Liu & Jordan models, and the Newell model was of the lowest accuracy.

On the other hand, Mesri [11] showed and evaluated the performance of the most appropriate models used to recover solar components at ground level, via confronting meteorological techniques to selected semi empirical methods. An innovative approach was tested by the numerical simulation. An adaptive neuro-fuzzy inference system (ANFIS) was applied to develop a model for estimation of daily horizontal global solar radiation by Mohammadi et al. [12]. Long-term measured data for Iranian city of Tabass was used to train and test the ANFIS model. The statistical results verified that the ANFIS model provides accurate and reliable predictions.

The artificial neural network (ANN) techniques have been used in diverse applications in control, robotics, pattern recognition, forecasting, medicine, power systems, manufacturing, optimization, signal processing, and social/ psychological sciences. In the last years, neural network methods have been employed for the prediction of global solar radiation both in time and space. Linares-Rodriguez et al [13] predicted the solar radiation values in locations without ground measurements, by using the reanalysis data as an alternative to the use of satellite imagery. The model was validated in Andalusia (Spain), using measured data for nine years from 83 ground stations spread over the region. The geographical location (latitude, longitude), the day of the year, the daily clear sky global radiation, and the four meteorological variables was used as input data while the daily global solar radiation was the only output of the ANN in this study. Benghanem et al. [14] used the ANN methods models to estimate and model of daily global solar radiation in their study. The available data such as the global irradiation, diffuse irradiation, air temperature and relative humidity available from 1998 to 2002 at the National Renewable Energy Laboratory (NREL) website were used. It was found that the model using sunshine duration and air temperature as inputs, presented the good accurate results since the correlation coefficient is 97.65%. Sahin et al. [15] tested the estimation capacities of ANN techniques to predict monthly-average daily solar radiation over Turkey. According to results of the study, the satellite-based solar radiation map for Turkey was generated. On the other hand, Koca et al.

[16] suggested the ANN model to estimate the solar radiation parameters for seven cities from Mediterranean region of Anatolia in Turkey. The obtained results indicated that the method could be used by researchers or scientists to design high efficiency solar devices. Additionally, the ANN techniques were employed for designing solar systems and predicting solar radiations by Qazi et al. [17]. This study indicated that ANN network gave good accuracy in terms of prediction error of less than 20%. Therefore, ANN method as compared to other empirical models was capable to deal with many input meteorological parameters, which made it more accurate and reliable.

Spatial variation of incoming radiation is mainly influenced by topographical and atmospheric features whereas latitudinal gradient is almost insignificant. Park et al. [18] investigated the spatial distribution of solar radiation using topographic factor and sunshine duration in South Korea. Hassan et al. [19] suggested the new ambient-temperature-based models for estimating global solar radiation as alternatives to the widely used sunshine-based models owing to the unavailability of sunshine data at all locations around the world. Seventeen new temperature-based models were established, validated and compared with other three models proposed in the literature (the Annandale, Allen and Goodin models) to estimate the monthly average daily global solar radiation on a horizontal surface.

In this study, several empirical correlation models for estimating the monthly average daily global solar radiation on the horizontal surface were developed in connection with the measured solar radiation, sunshine duration and ambient temperature. These models were applied to Eskişehir City of Turkey. The results of empirical models were compared using the statistical evaluation methods as the relative percentage error (E), the mean percentage error (MPE), the mean absolute percentage error ($MAPE$), the sum of the squares of relative errors ($SSRE$), the relative standard error (RSE), the mean bias error (MBE), the root square error ($RMSE$), and correlation coefficient (R^2).

31. DATA AND METHODOLOGY

31.1. Data set

The data set of the solar radiation, the wind velocity, the wind direction, the ambient temperature and pressure, and the relative humidity were measured by the measuring station at Eskişehir City of Turkey. The measuring data had been collected between 01 January 2011 and 31 December 2014. The latitude, the longitude, and the elevation of measuring station location is $39^{\circ} 44' 49''$ -N, $30^{\circ} 28' 49''$ -E, and 853 meters, respectively. The photographs of the measuring station [20] are illustrated in Fig.1 and Fig.2.

31.2. Astronomical parameters

2.2.1. Declination angle (δ)

The angle between the earth-sun line and the equatorial

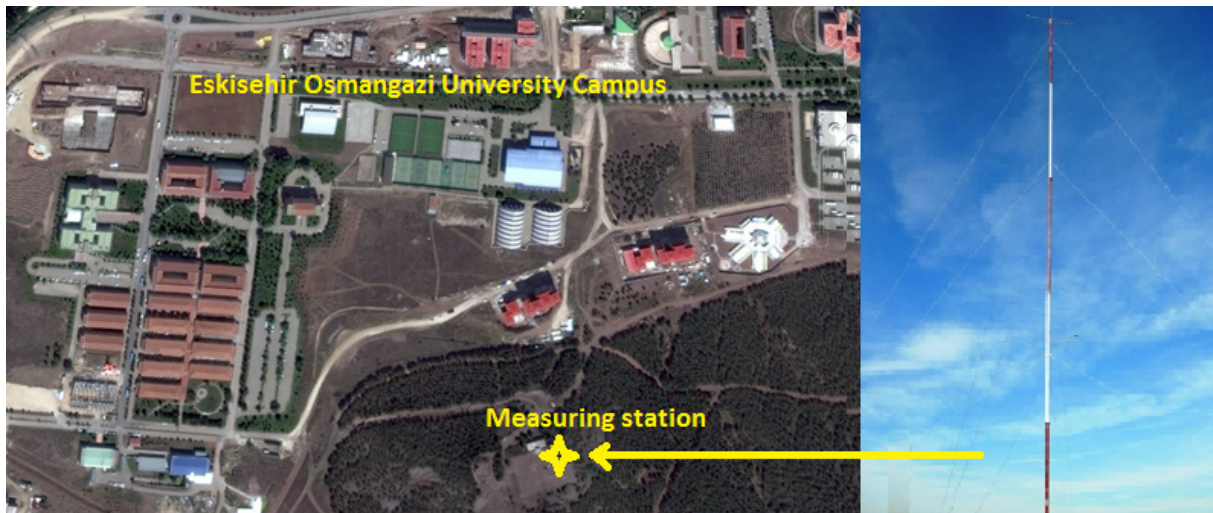


Figure 1. The measuring station at Eskisehir of Turkey [20].

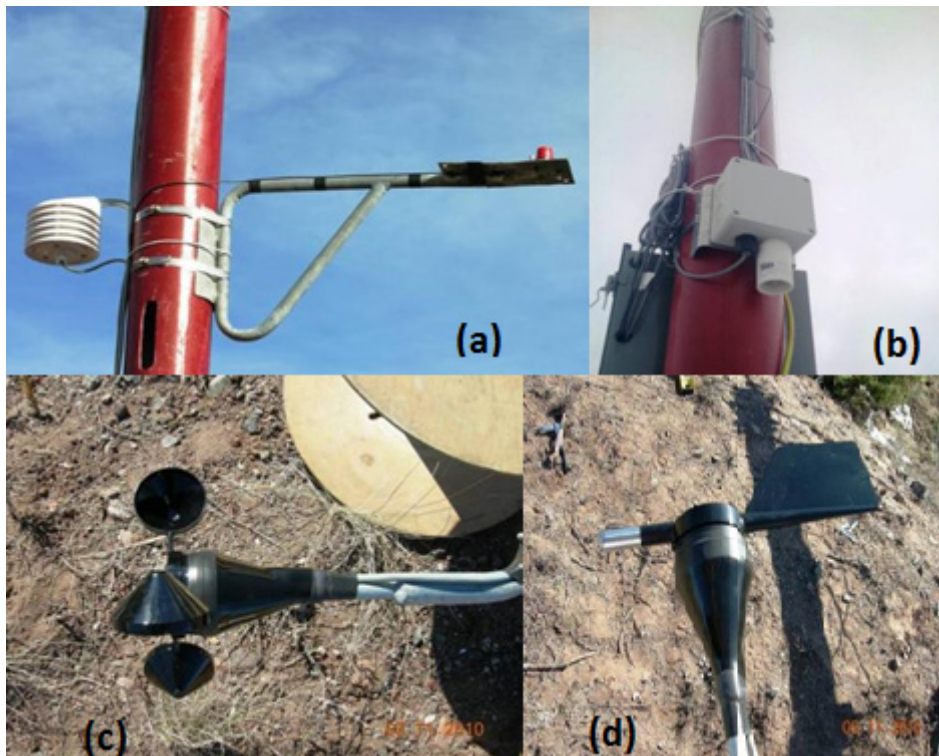


Figure 2. Measurement system parts (a) 110S Temperature sensor with radiation shield for temperature measurement and Li-Cor Li-200R Pyrometer for solar radiation measurement. (b) relative humidity sensor (c) RNRG 40 Anemometer for wind velocity measurement . (d) RNRG 200P Wind vane for wind direction measurement [20].

plane is named the declination angle. It varies over the year from -23.45° at the winter solstice to $+23.45^\circ$ at summer solstice. The declination angle can be estimated the following equation [21-24];

$$\delta = 23.45 \sin\left(\frac{360}{365}(284 + n_{day})\right) \quad (1)$$

where n_{day} is the number of the day corresponding to a given date starting from 1 on 1 January to 365 on 31 December.

2.2.2. Sunset hour angle (ω_s)

The sunset hour angle in degrees can be calculated from [21-24];

$$\omega_s = \cos^{-1}(-\tan \phi \tan \delta) \quad (2)$$

2.2.3. Number of daylight hours (daylight duration)

The number of daylight hours (daylight duration) is based on the hour angle and obtained the following equation [21-24];

$$S_o = \frac{2}{15} \omega_s \quad (3)$$

2.2.4. Extraterrestrial radiation (G_o)

The amount of solar energy that would be received in the absence of the atmosphere is called the extraterrestrial radiation. The change in the extraterrestrial radiation is caused by two sources, i.e., variation in radiation emitted by the sun and variation of earth–sun distance. This change is considered taking into account the astronomical factors according to the following relation [21, 23-24];

$$G_{on} = G_{sc} \left(1 + 0.034 \cos \left(\frac{360 n_{day}}{365.25} \right) \right) \quad (4)$$

The monthly average daily extraterrestrial radiation on a horizontal surface (H_o) was obtained from the following equations [8, 21-24],

$$H_o = \frac{24}{\pi} G_{on} \left(\cos \phi \cos \delta \cdot \sin \omega_s + \frac{\pi}{180} \omega_s \cdot \sin \phi \cdot \sin \delta \right) \quad (5)$$

2.3. Global solar radiation models

The most well-known models, Angström-Prescott model, express the monthly average daily global solar radiation as a function of the monthly average daily measure sunshine duration as the following [25- 26];

$$\frac{H}{H_o} \approx f \left(\frac{S}{S_o} \right) \quad (6)$$

where H is the monthly average daily global solar radiation (MJm^{-2}), H_o is the monthly average daily extraterrestrial radiation (MJm^{-2}), S is the monthly average daily measured sunshine duration (h) and S_o is the monthly average daily daylight duration (h).

The first mathematical expression of this type was the linear regression equation developed by Angstrom and modified by Page, and was between the global solar radiation and the sunshine duration, which is the most convenient and widely used as given by [27]:

$$\frac{H}{H_o} = a + b \frac{S}{S_o} \quad (7)$$

In the course of time, the nonlinear polynomial relation models derived from Angstrom linear regression equation were suggested for increasing the accuracy of models at extreme points [22, 28]. After that, many researchers have done a large number of modifications on this model to improve accuracy. Several typical models based on sunshine duration are given below [18, 29–36],

$$\frac{H}{H_o} = a + b \frac{S}{S_o} + c \left(\frac{S}{S_o} \right)^2 \quad (8)$$

$$\frac{H}{H_o} = a + b \frac{S}{S_o} + c \left(\frac{S}{S_o} \right)^2 + d \left(\frac{S}{S_o} \right)^3 \quad (9)$$

$$\frac{H}{H_o} = a + b \log \left(\frac{S}{S_o} \right) \quad (10)$$

$$\frac{H}{H_o} = a + b \left(\frac{S}{S_o} \right) + c \log \left(\frac{S}{S_o} \right) \quad (11)$$

$$\frac{H}{H_o} = a + \exp \left(\frac{S}{S_o} \right) \quad (12)$$

$$\frac{H}{H_o} = a + b \left(\frac{S}{S_o} \right) + c \exp \left(\frac{S}{S_o} \right) \quad (13)$$

$$\frac{H}{H_o} = a + b \left(\frac{S}{S_o} \right)^c \quad (14)$$

$$\frac{H}{H_o} = a + b \cos \left(c \frac{S}{S_o} \right) + d \sin \left(c \frac{S}{S_o} \right) + e \cos \left(2c \frac{S}{S_o} \right) + f \sin \left(2c \frac{S}{S_o} \right) \quad (15)$$

where a, b, c, d, e, f are the correlation coefficients.

The strong relation between solar radiation and ambient temperature can be explained by the behavior of the earth's

surface towards the radiation received from the sun. The solar energy that reaches the atmosphere in the form of short-wave electromagnetic radiation is absorbed by the earth's surface, causing the earth to warm up. The warm earth's surface reemits a part of the absorbed energy in the form of long wave radiation to heat up the surrounding ambient air. The ambient air is not directly heated by the solar radiation but is heated by the contact with the hot earth's surface. In general, the fluctuation in air temperature can be affected by radiation balance and air mass advection. The local ambient air temperature and radiation balance are affected by cloud cover and the nature of surface coverage as well as the time of day and day of the year. The systematic variation in incoming solar radiation over the course of a year can be reflected in the annual temperature cycle in which a strong relation between solar radiation and ambient temperature is noticed [36]. Several typical models based on ambient temperature from are given as following [19, 29, 37-41];

$$\frac{H}{H_o} = a + bT \quad (16)$$

$$\frac{H}{H_o} = a + bT + cT^2 \quad (17)$$

$$\frac{H}{H_o} = a + bT + cT^2 + cT^3 \quad (18)$$

$$H = a + \exp(bT^c) \quad (19)$$

$$\frac{H}{H_o} = a + bT + cT^2 + cT^3 \quad (20)$$

$$\frac{H}{H_o} = a\Delta T^b + c \quad (21)$$

$$\frac{H}{H_o} = aT^b H_o \quad (22)$$

$$\frac{H}{H_o} = aT^b H_o + c \quad (23)$$

$$\frac{H}{H_o} = (a + b\Delta T)\Delta T^c \quad (24)$$

$$\frac{H}{H_o} = (a + b\Delta T + c\Delta T^2)\Delta T^d \quad (25)$$

$$\frac{H}{H_o} = (a + b\Delta T + c\Delta T^2)\Delta T^{0.5} + d \quad (26)$$

$$\frac{H}{H_o} = (a + b\Delta T + c\Delta T^2)\Delta T^d + e \quad (27)$$

$$\frac{H}{H_o} = (a + b\Delta T + c\Delta T^2 + d\Delta T^3)\Delta T^e + f \quad (28)$$

$$\frac{H}{H_o} = (a + bT)\Delta T^c + d \quad (29)$$

$$\frac{H}{H_o} = (a + bT)\Delta T^c \quad (30)$$

$$\frac{H}{H_o} = (a + bT + cT^2)\Delta T^d + e \quad (31)$$

$$\frac{H}{H_o} = (a + bT + cT^2)\Delta T^d \quad (32)$$

$$\frac{H}{H_o} = (a + bT + cT^2 + dT^3)\Delta T^e \quad (33)$$

$$\frac{H}{H_o} = a(1 + 2.7 \times 10^{-5} Z) \Delta T^{0.5} \tag{34}$$

$$\frac{H}{H_o} = a \left(1 - \exp \left[-b \frac{\Delta T^c}{H_o} \right] \right) \tag{35}$$

where Z is the elevation of site from the sea level.

While the solar radiation (H), sunshine duration (S) and the ambient temperature (T) are measured by the measuring station, the daylight duration (S_o) and the extraterrestrial radiation (H_o) are calculated from the eqn. (3) and (eqn. (5), respectively.

32. STATISTICAL ANALYSIS METHODS

A number of statistical analysis methods have been used to evaluate the accuracy of the models of solar radiation estimations. Some of these, the relative percentage error (E), the mean percentage error (MPE), the mean absolute percentage error ($MAPE$), the sum of the squares of relative errors ($SSRE$), the relative standard error (RSE), the mean bias error (MBE), the root square error ($RMSE$), and correlation coefficient (R^2) are the most commonly used to compare the results [5, 8-10, 18, 22, 28, 42-45]. In all the above statistical tests of accuracy, except R^2 , the smaller the value, the better is the model performance. The statistical performance metrics are given in Table 1.

33. RESULTS AND DISCUSSION

The monthly average daily values of the global solar radiation (H), sunshine duration (S), wind velocity (V), ambient temperature (T), ambient pressure (P), relative humidity (RH), the extraterrestrial radiation (H_o), daylight duration (S_o), solar radiation fraction ($\frac{H}{H_o}$) and sunshine duration fraction ($\frac{S}{S_o}$) were calculated from the 10-secondly measuring data and given in Table 2. The monthly average daily values of the solar radiation and the sunshine duration were illustrated in Fig. 3 and Fig.4. Using the data in Table 1 and Minitab™ program; the variations between ($\frac{H}{H_o}$) and ($\frac{S}{S_o}$), between ($\frac{H}{H_o}$) and (T), between ($\frac{H}{H_o}$) and (V), between ($\frac{H}{H_o}$) and (RH), and between ($\frac{H}{H_o}$) and (P) were analyzed and indicated in Fig.5. Minitab™ is a statistical package that provides

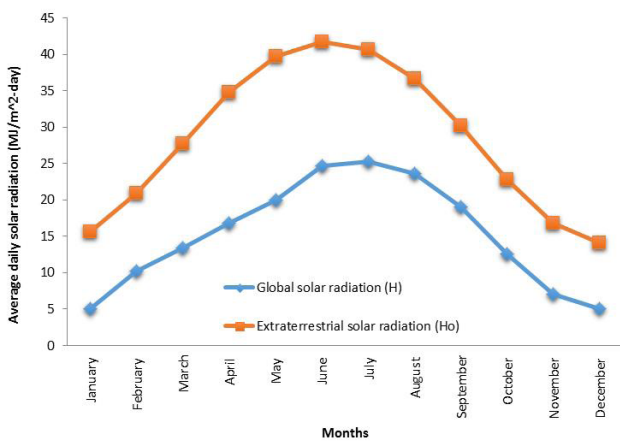


Figure 3. The annually distributions of the monthly average daily global and extraterrestrial solar radiations

a broad range of basic and advanced data analysis techniques. It includes regression techniques, analysis of variance experimental design and control charts, quality tools, survival analysis, multivariate analyses, time series, descriptive and non-parametric statistics exploratory data analysis, power and sample-size calculation. The results of analysis, the sunshine duration fraction ($\frac{S}{S_o}$) and the ambient temperature (T) were determined to be more impressive on the solar radiation fraction ($\frac{H}{H_o}$). After that, the new twelve empirical models relating to H , $\frac{H}{H_o}$, $\frac{S}{S_o}$, and T were suggested as fitted to experimental data. The regression graphs, the correlation coefficients (a, b, c, d, \dots) and coefficient of determination (R^2) obtained from Minitab™ were demonstrated in Fig.6-17. The obtained equations for new models are given as the following;

Model-1:

$$\frac{H}{H_o} = 0.1761 + 0.6021 \frac{S}{S_o}, \quad (R^2 = 0.935) \tag{45}$$

Model-2:

$$\frac{H}{H_o} = 0.1640 + 0.6529 \frac{S}{S_o} - 0.0482 \left(\frac{S}{S_o} \right)^2, \quad (R^2 = 0.935) \tag{46}$$

Model-3:

$$\frac{H}{H_o} = 0.0315 + 1.528 \frac{S}{S_o} - 1.835 \left(\frac{S}{S_o} \right)^2 + 1.144 \left(\frac{S}{S_o} \right)^3, \quad (R^2 = 0.936) \tag{47}$$

Model-4:

$$\frac{H}{H_o} = 0.3721 + 0.01178T, \quad (R^2 = 0.814) \tag{48}$$

Model-5:

$$\frac{H}{H_o} = 0.3620 + 0.01478T - 0.000128T^2, \quad (R^2 = 0.817) \tag{49}$$

Model-6:

$$\frac{H}{H_o} = 0.3364 + 0.02911T - 0.001668T^2 + 0.000043T^3, \quad (R^2 = 0.827) \tag{50}$$

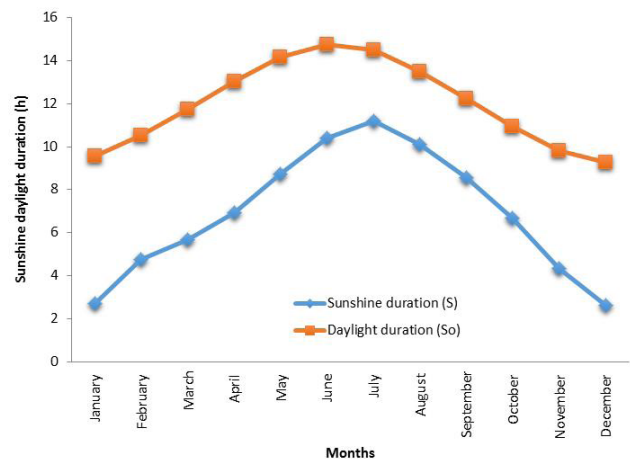


Figure 4. The annually distributions of the monthly average daily sunshine duration and daylight duration.

Table 1. The performance tools for statistical analysis

| Metrics | Relations | Explanation | Eqn. No. |
|--|--|--|----------|
| Relative percentage error (E) | $E = \left(\frac{C_i - m_i}{m_i} \right) 100$ | The E provides the percentage deviation data between the calculated and measured. The ideal value of E equals to zero. here C_i is the ith calculated value, m_i is the ith measured value | (36) |
| Mean percentage error (MPE) | $MPE = \frac{\sum_{i=1}^n E}{n}$ | The mean percentage error is explained as the average value of percentage deviation between estimated and measured solar radiations. Where n is the number of measured and estimated values | (37) |
| Mean absolute percentage error (MAPE) | $MAPE = ABS \left(\frac{\sum_{i=1}^n E}{n} \right)$ | The mean absolute percentage error is expressed as the absolute average value of percentage deviation between estimated and measured solar radiations | (38) |
| Sum of the squares of relative error (SSRE) | $SSRE = \sum_{i=1}^n \left(\frac{C_i - m_i}{m_i} \right)^2$ | The SSRE give us the positive value of sum of squares of relative deviations throughout the year. The ideal value of SSRE equals to zero. | (39) |
| Relative standard error (RSE) | $RSE = \sqrt{\frac{SSRE}{n}}$ | The RSE provides the degree of accuracy of estimation correlations. | (40) |
| Mean bias error (MBE) | $MBE = \frac{1}{n} \sum_{i=1}^n (C_i - m_i)$ | The mean bias error is the average difference between measured and estimated values. The MBE gives some information on the long-term performance of correlations. The positive MBE indicates an overestimation, while a negative MBE shows an underestimation. The ideal value of MBE is zero. | (41) |
| Root mean square error (RMSE) | $RMSE = \sqrt{\frac{1}{n} \sum_{i=1}^n (C_i - m_i)^2}$ | The RMSE provides a general indicator about on the short-term performance of correlations. The RMSE is always positive. Because the lower of RMSE values shows the more accurate model, the ideal value of RMSE equals to zero and is always positive | (42) |
| Correlation coefficient (R²) | $R^2 = \frac{\sum_{i=1}^n (C_i - C_a)(m_i - m_a)}{\sqrt{\left[\sum_{i=1}^n (C_i - C_a)^2 \right] \left[\sum_{i=1}^n (m_i - m_a)^2 \right]}}$ | The correlation coefficient is used to analyze for determining the relation between estimated and measured values. Where C_a and m_a expressed the average of the calculated and measured values, respectively. | (43) |
| t-statistic method (t-stat) | $t - stat = \sqrt{\frac{(n-1)MBE^2}{RMSE^2 - MBE^2}}$ | To determine whether or not the equation estimates are statistically significant, i.e., not significantly different from their actual counterparts, at a particular confidence level, it is proposed the t-statistic as the correlation. | (44) |

Model-7:

$$H = -1.981 + 2.496S, (R^2 = 0.979) \tag{51}$$

Model-8:

$$H = -1.717 + 2.402S + 0.00683S^2, (R^2 = 0.979) \tag{52}$$

Model-9:

$$H = 2.086 + 0.238S + 0.3616S^2 - 0.01744S^3, (R^2 = 0.98) \tag{53}$$

Model-10:

$$H = 4.959 + 0.8847T, (R^2 = 0.910) \tag{54}$$

Model-11:

$$H = 5.018 + 0.8669T + 0.00076T^2, (R^2 = 0.910) \tag{55}$$

Model-12:

$$H = 54.617 + 1.091T - 0.0234T^2 + 0.00068T^3, (R^2 = 0.910) \tag{56}$$

The measured and estimated values of H were given in Table 3 and shown in Fig.18-21. By using the statistical analysis methods, the values of H in Table 3 estimated from new models were compared with the measured values and tabulated in Table 4. The main remarkable statistical results are given as the following;

- (i) Between the new models, Model 1(eqn.(45)) has the best MAPE value with 4.52 between the new models.
- (ii) Model-3 (eqn.(47)) has the best MPE, SSRE, RSE, RMSE and R² values with 0.22, SSRE= 0.00257, RSE= 0.01463, RMSE=0.77312 and 0.99457.
- (iii) Model-11 has the best MBE and t-stat values with 0.00022 and 0.00034 between the new models.

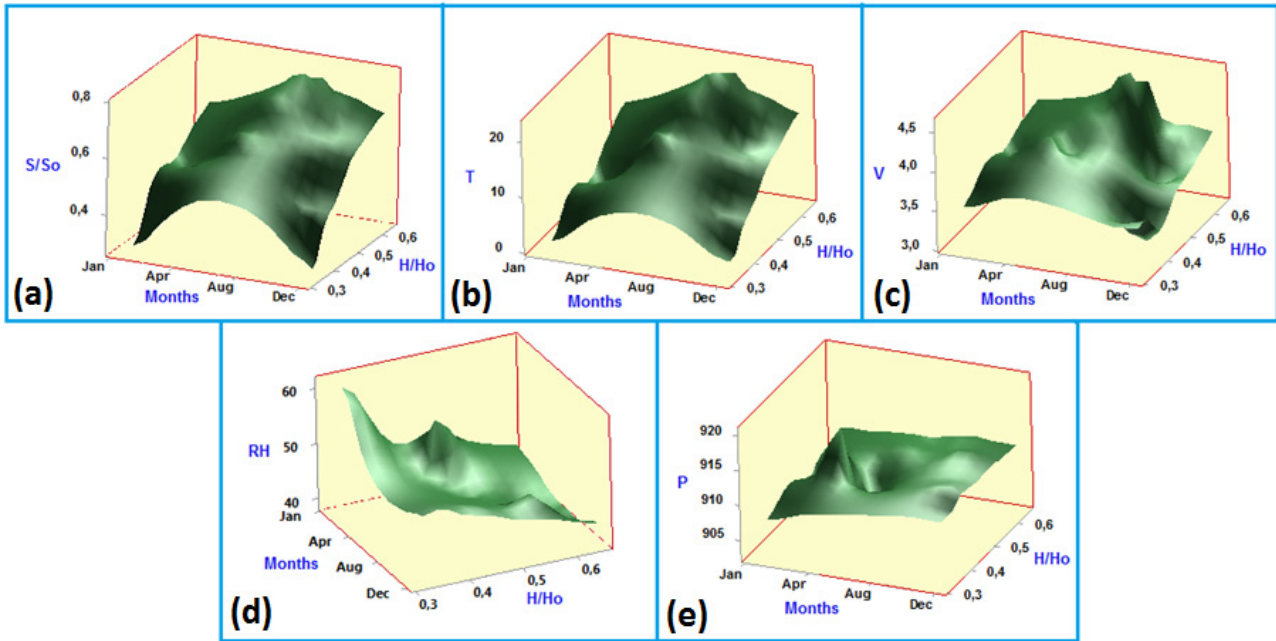


Figure 5. The variations (a) between $(\frac{H}{H_o})$ and $(\frac{S}{S_o})$, (b) between $(\frac{H}{H_o})$ and (T) , (c) between $(\frac{H}{H_o})$ and (V) , (d) between $(\frac{H}{H_o})$ and (RH) , (e) between $(\frac{H}{H_o})$ and (P) .

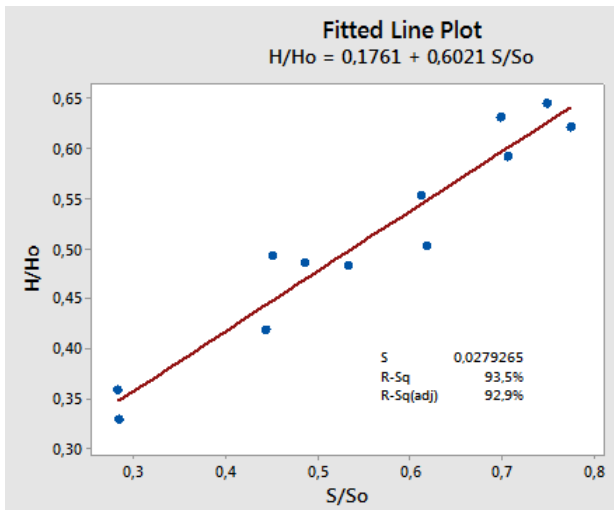


Figure 6. Linear regression between $(\frac{H}{H_o})$ and $(\frac{S}{S_o})$

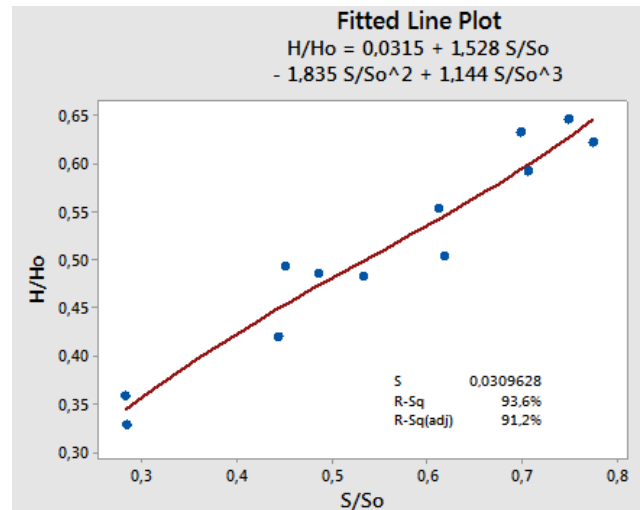


Figure 8. Third order polynomial regression line between $(\frac{H}{H_o})$ and $(\frac{S}{S_o})$

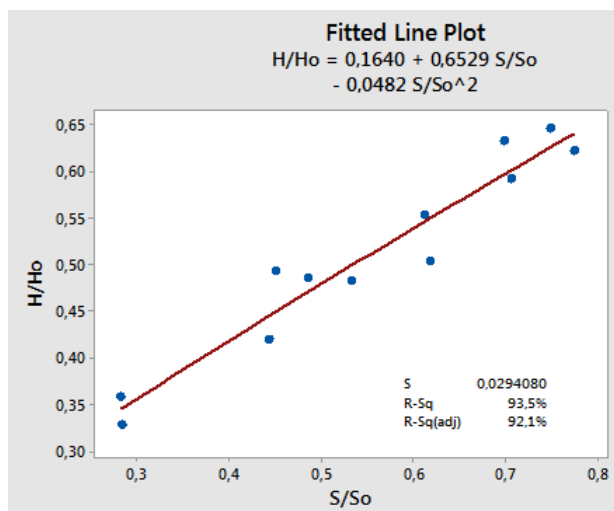


Figure 7. Second order polynomial regression line between $(\frac{H}{H_o})$ and $(\frac{S}{S_o})$

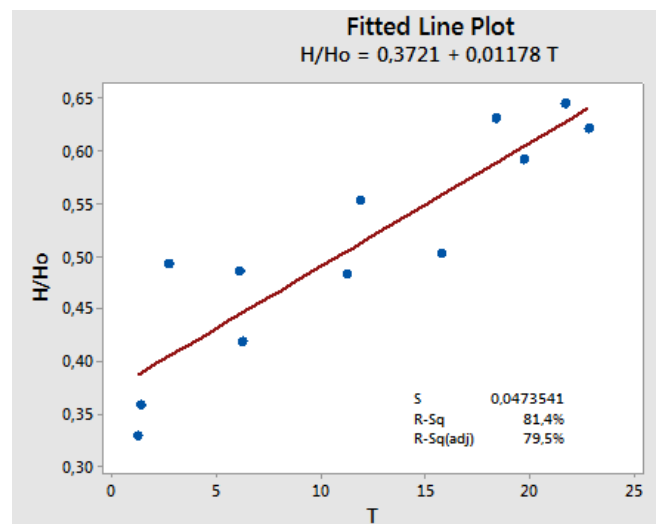


Figure 9. Linear regression between $(\frac{H}{H_o})$ and (T)

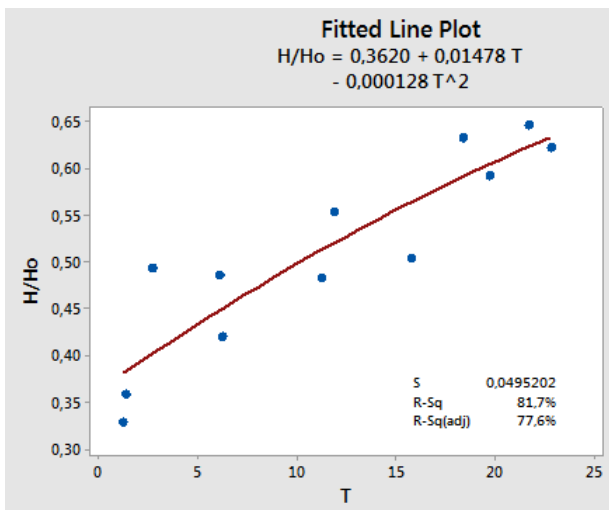


Figure 10. Second order polynomial regression line between $\left(\frac{H}{H_o}\right)$ and (T)

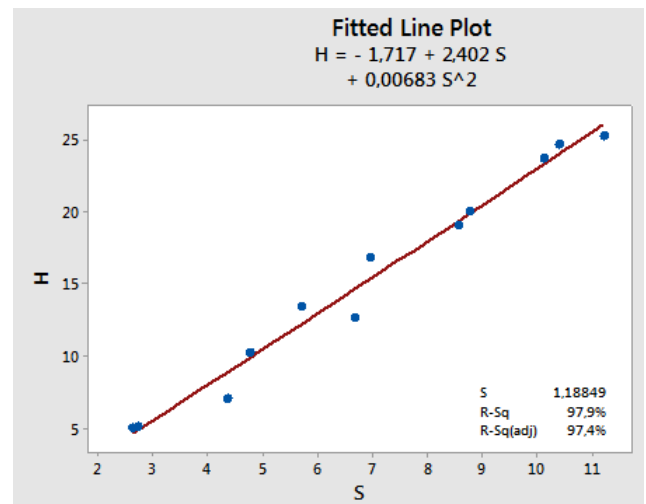


Figure 13. Second order polynomial regression line between (H) and (S)

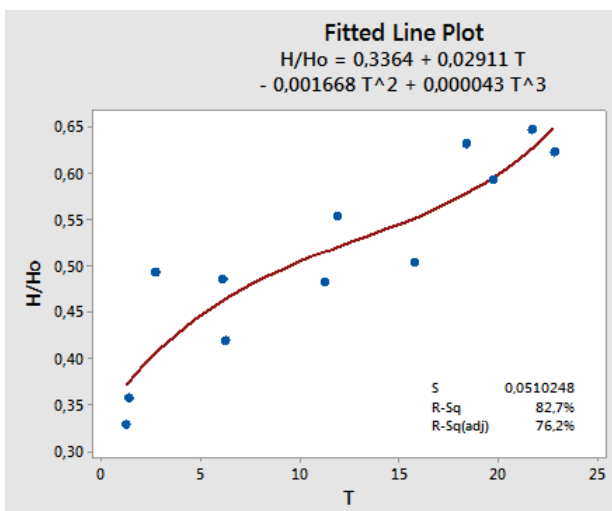


Figure 11. Third order polynomial regression line between $\left(\frac{H}{H_o}\right)$ and (T)

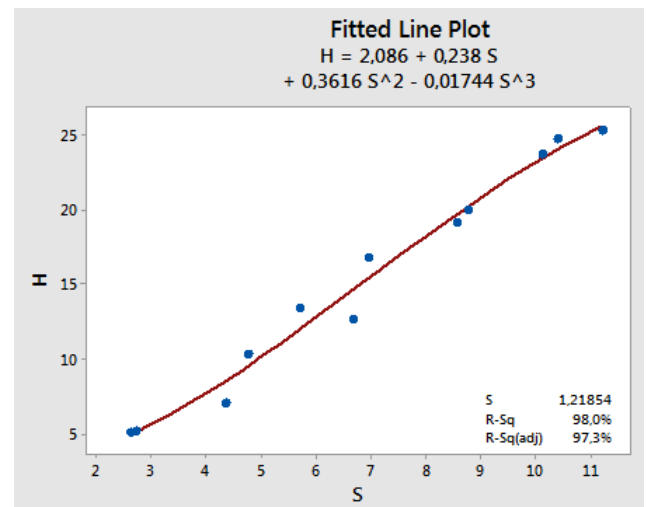


Figure 14. Third order polynomial regression line between (H) and (S)

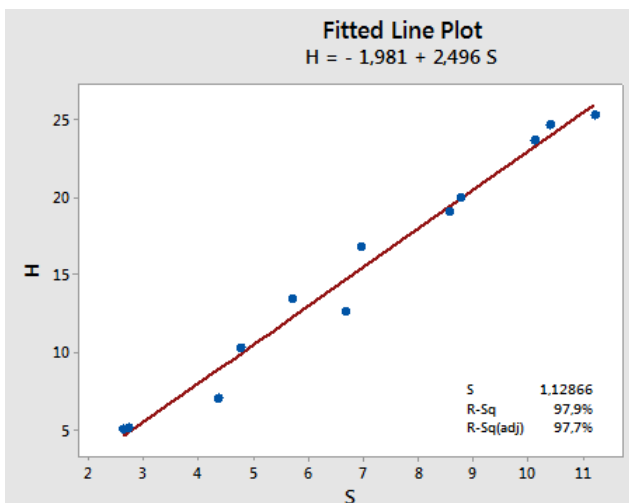


Figure 12. Linear regression between (H) and (S)

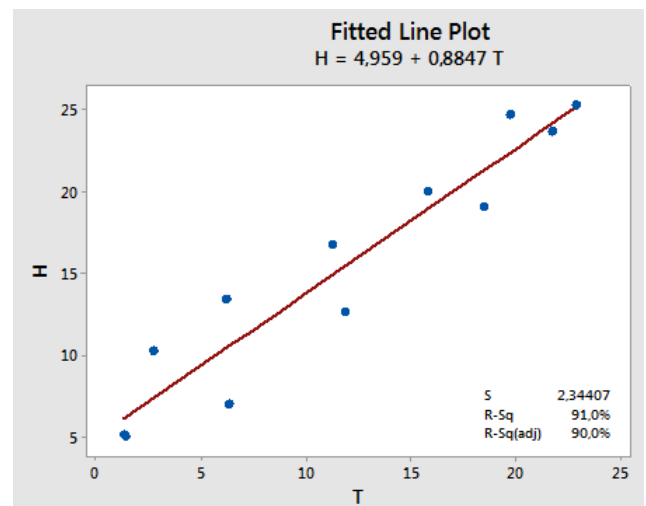


Figure 15. Linear regression between (H) and (T)

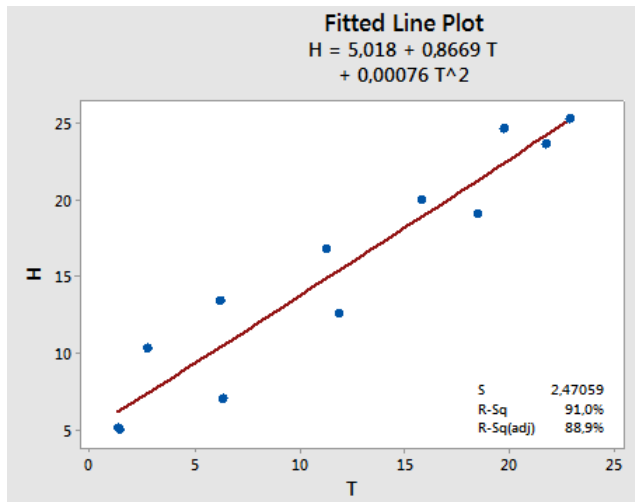


Figure 16. Second order polynomial regression line between (H) and (T)

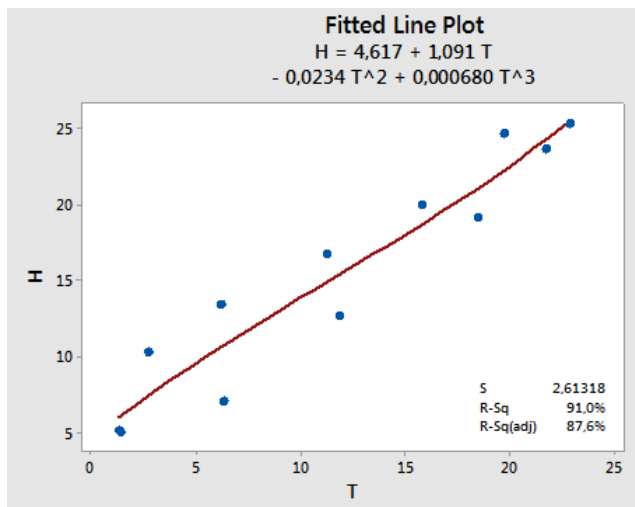


Figure 17. Third order polynomial regression line between (H) and (T)

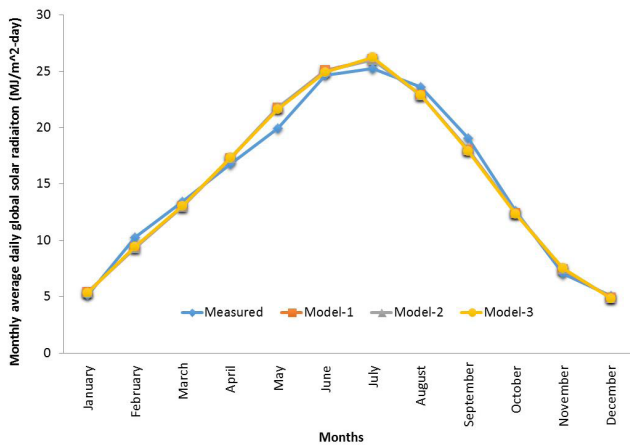


Figure 18. The annually distributions of the monthly average daily solar radiation estimated from Model-1, Model-2 and Model-3.

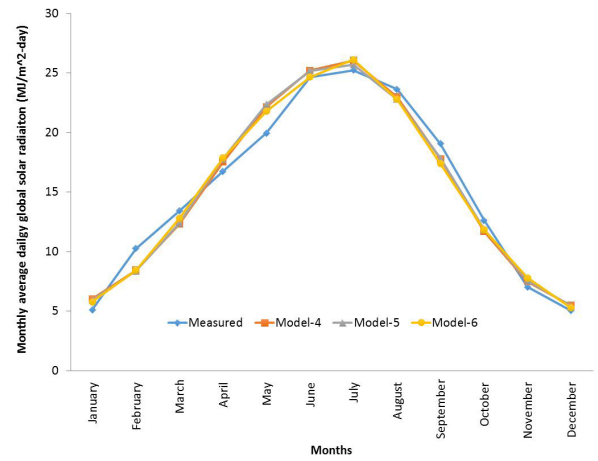


Figure 19. The annually distributions of the monthly average daily solar radiation estimated from Model-4, Model-5 and Model-6.

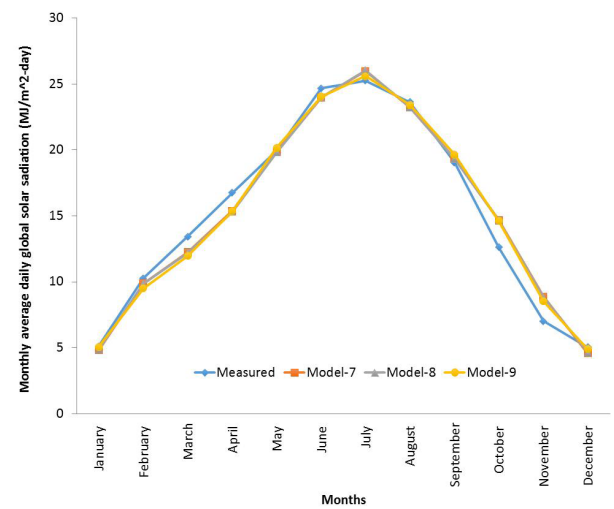


Figure 20. The annually distributions of the monthly average daily solar radiation estimated from Model-7, Model-8 and Model-9.

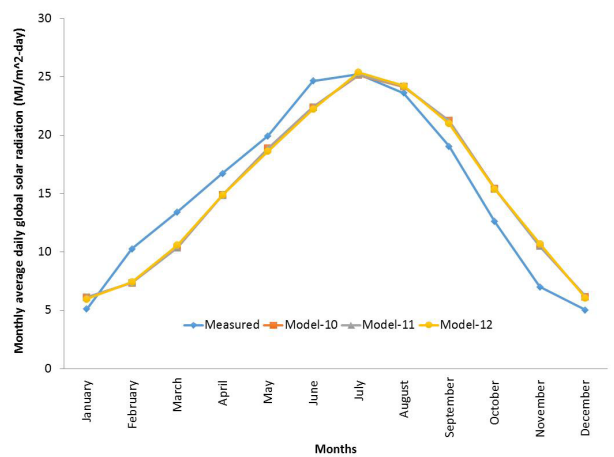


Figure 21. The annually distributions of the monthly average daily solar radiation estimated from Model-10, Model-11 and Model-12.

Table 2. Measured and calculated metrological data for Eskisehir City.

| Months | Measured values | | | | | | Calculated Values | | | |
|-----------|-----------------|------|------|-------|--------|-------|-------------------|-------|-------|-------|
| | H | S | V | T | P | RH | Ho | So | H/Ho | S/So |
| January | 5.11 | 2.72 | 3.50 | 1.29 | 907.41 | 60.89 | 15.57 | 9.56 | 0.328 | 0.285 |
| February | 10.27 | 4.75 | 3.58 | 2.73 | 902.91 | 53.48 | 20.87 | 10.55 | 0.492 | 0.450 |
| March | 13.43 | 5.7 | 3.97 | 6.14 | 920.32 | 43.00 | 27.70 | 11.73 | 0.485 | 0.486 |
| April | 16.75 | 6.95 | 4.05 | 11.24 | 907.68 | 42.56 | 34.77 | 13.05 | 0.482 | 0.533 |
| May | 19.96 | 8.75 | 3.75 | 15.75 | 904.44 | 41.88 | 39.71 | 14.17 | 0.503 | 0.618 |
| June | 24.66 | 10.4 | 4.02 | 19.73 | 910.98 | 39.77 | 41.71 | 14.74 | 0.591 | 0.706 |
| July | 25.24 | 11.2 | 4.60 | 22.82 | 910.17 | 39.24 | 40.64 | 14.48 | 0.621 | 0.774 |
| August | 23.63 | 10.1 | 4.39 | 21.73 | 911.33 | 40.18 | 36.61 | 13.51 | 0.645 | 0.747 |
| September | 19.06 | 8.55 | 3.75 | 18.42 | 912.01 | 39.54 | 30.20 | 12.24 | 0.631 | 0.698 |
| October | 12.62 | 6.68 | 3.37 | 11.87 | 912.84 | 47.14 | 22.83 | 10.93 | 0.553 | 0.611 |
| November | 7.03 | 4.35 | 3.11 | 6.29 | 912.50 | 48.55 | 16.79 | 9.82 | 0.419 | 0.443 |
| December | 5.05 | 2.63 | 3.58 | 1.39 | 910.69 | 50.78 | 14.12 | 9.27 | 0.357 | 0.284 |
| Average | 15.23 | 6.90 | 3.81 | 11.62 | 910.27 | 45.58 | 28.46 | 12.00 | 0.509 | 0.553 |

Table 3. The monthly average daily global solar radiation values estimated from the developed models.

| Months | Measured | Model-1 | Model-2 | Model-3 | Model-4 | Model-5 | Model-6 | Model-7 | Model-8 | Model-9 | Model-10 | Model-11 | Model-12 |
|-----------|----------|---------|---------|---------|---------|---------|---------|---------|---------|---------|----------|----------|----------|
| January | 5.11 | 5.41 | 5.39 | 5.36 | 6.03 | 5.93 | 5.78 | 4.81 | 4.87 | 5.06 | 6.10 | 6.13 | 5.98 |
| February | 10.27 | 9.34 | 9.36 | 9.43 | 8.44 | 8.38 | 8.44 | 9.88 | 9.85 | 9.51 | 7.37 | 7.39 | 7.43 |
| March | 13.43 | 12.98 | 13.01 | 13.07 | 12.31 | 12.41 | 12.80 | 12.25 | 12.20 | 11.96 | 10.39 | 10.37 | 10.59 |
| April | 16.75 | 17.28 | 17.32 | 17.31 | 17.54 | 17.80 | 17.87 | 15.37 | 15.31 | 15.35 | 14.90 | 14.86 | 14.89 |
| May | 19.96 | 21.76 | 21.80 | 21.63 | 22.14 | 22.36 | 21.80 | 19.86 | 19.82 | 20.17 | 18.89 | 18.86 | 18.65 |
| June | 24.66 | 25.07 | 25.05 | 24.94 | 25.21 | 25.18 | 24.67 | 23.98 | 24.00 | 24.05 | 22.41 | 22.41 | 22.25 |
| July | 25.24 | 26.08 | 26.02 | 26.21 | 26.04 | 25.71 | 26.13 | 25.97 | 26.04 | 25.61 | 25.15 | 25.20 | 25.41 |
| August | 23.63 | 22.92 | 22.88 | 22.92 | 22.99 | 22.80 | 22.79 | 23.23 | 23.24 | 23.41 | 24.18 | 24.21 | 24.25 |
| September | 19.06 | 18.02 | 18.01 | 17.92 | 17.79 | 17.84 | 17.38 | 19.36 | 19.32 | 19.65 | 21.25 | 21.24 | 21.02 |
| October | 12.62 | 12.42 | 12.44 | 12.35 | 11.69 | 11.86 | 11.85 | 14.69 | 14.63 | 14.61 | 15.46 | 15.41 | 15.40 |
| November | 7.03 | 7.44 | 7.45 | 7.52 | 7.49 | 7.55 | 7.79 | 8.88 | 8.86 | 8.53 | 10.53 | 10.50 | 10.73 |
| December | 5.05 | 4.90 | 4.88 | 4.85 | 5.48 | 5.40 | 5.28 | 4.58 | 4.65 | 4.90 | 6.19 | 6.23 | 6.09 |
| Average | 15.23 | 15.30 | 15.30 | 15.29 | 15.26 | 15.27 | 15.22 | 15.24 | 15.23 | 15.23 | 15.23 | 15.23 | 15.22 |

Table 4. The statistical analysis results of the new developed models

| Months | Relative Percentage Error (E) | | | | | | | | | | | |
|----------------|-------------------------------|---------|---------|---------|---------|----------|---------|----------|----------|----------|----------|----------|
| | Model-1 | Model-2 | Model-3 | Model-4 | Model-5 | Model-6 | Model-7 | Model-8 | Model-9 | Model-10 | Model-11 | Model-12 |
| January | 5.93 | 5.46 | 4.91 | 18.06 | 16.09 | 13.16 | -5.86 | -4.71 | -0.97 | 19.38 | 20.11 | 17.15 |
| February | -9.10 | -8.90 | -8.15 | -17.85 | -18.43 | -17.84 | -3.86 | -4.13 | -7.45 | -28.20 | -28.05 | -27.61 |
| March | -3.33 | -3.08 | -2.65 | -8.32 | -7.60 | -4.65 | -8.80 | -9.17 | -10.92 | -22.64 | -22.80 | -21.15 |
| April | 3.11 | 3.38 | 3.29 | 4.69 | 6.24 | 6.65 | -8.29 | -8.64 | -8.37 | -11.05 | -11.32 | -11.14 |
| May | 9.01 | 9.19 | 8.38 | 10.93 | 12.00 | 9.23 | -0.51 | -0.69 | 1.04 | -5.37 | -5.54 | -6.58 |
| June | 1.66 | 1.61 | 1.15 | 2.24 | 2.12 | 0.07 | -2.76 | -2.66 | -2.45 | -9.11 | -9.10 | -9.76 |
| July | 3.33 | 3.06 | 3.83 | 3.18 | 1.84 | 3.52 | 2.90 | 3.17 | 1.45 | -0.38 | -0.19 | 0.65 |
| August | -3.00 | -3.16 | -3.00 | -2.69 | -3.52 | -3.55 | -1.70 | -1.65 | -0.94 | 2.35 | 2.48 | 2.64 |
| September | -5.49 | -5.51 | -6.01 | -6.68 | -6.40 | -8.85 | 1.56 | 1.35 | 3.11 | 11.50 | 11.44 | 10.28 |
| October | -1.60 | -1.43 | -2.14 | -7.40 | -6.05 | -6.15 | 16.39 | 15.93 | 15.77 | 22.45 | 22.09 | 22.04 |
| November | 5.80 | 6.03 | 6.98 | 6.61 | 7.49 | 10.91 | 26.30 | 26.08 | 21.35 | 49.80 | 49.47 | 52.63 |
| December | -2.93 | -3.37 | -3.91 | 8.69 | 6.96 | 4.57 | -9.16 | -7.89 | -2.97 | 22.67 | 23.38 | 20.72 |
| MPE | 0.28 | 0.27 | 0.22 | 0.95 | 0.89 | 0.59 | 0.52 | 0.58 | 0.72 | 4.28 | 4.33 | 4.16 |
| MAPE | 4.52 | 4.52 | 4.53 | 8.11 | 7.90 | 7.43 | 7.34 | 7.17 | 6.40 | 17.08 | 17.16 | 16.86 |
| SSRE | 0.00265 | 0.00264 | 0.00257 | 0.00913 | 0.00868 | 0.00770 | 0.01051 | 0.01013 | 0.00815 | 0.04628 | 0.04643 | 0.04637 |
| RSE | 0.01485 | 0.01482 | 0.01463 | 0.02759 | 0.02690 | 0.02532 | 0.02960 | 0.02906 | 0.02607 | 0.06210 | 0.06220 | 0.06216 |
| MBE | 0.06611 | 0.06655 | 0.05849 | 0.02936 | 0.03310 | -0.01882 | 0.00311 | -0.00199 | -0.00006 | 0.00074 | 0.00022 | -0.00928 |
| RMSE | 0.78383 | 0.78677 | 0.77312 | 1.12130 | 1.14694 | 1.09609 | 1.03032 | 1.02927 | 0.99493 | 2.13984 | 2.13959 | 2.13369 |
| t-stat | 0.28073 | 0.28156 | 0.25163 | 0.08686 | 0.09576 | 0.05695 | 0.01000 | 0.00642 | 0.00021 | 0.00115 | 0.00034 | 0.01443 |
| R ² | 0.99447 | 0.99439 | 0.99457 | 0.98835 | 0.98765 | 0.98845 | 0.98945 | 0.98948 | 0.99017 | 0.95368 | 0.95369 | 0.95395 |

34. CONCLUSIONS

Solar energy occupies one of the most important places among the various possible alternative energy sources not only in Turkey but also in the other countries in the sunny belt. Solar energy technologies suggest a clean, renewable and domestic energy source, and are essential components of a sustainable energy future. In the design and study of solar energy, information on solar radiation and its components at a given location is very essential. In this regard, solar radiation models are of big importance.

The review and classification of the published works in estimation of solar radiation shows that sunshine duration, relative humidity, air temperature and geographical parameters such as longitude, altitude, and latitude are the most correlated parameters and the solar radiation estimation methods can be classified as linear, nonlinear, artificial intelligence modeling and fuzzy logic modelling techniques. In this study, twelve empirical models were developed to predict the monthly average daily global solar radiation over Eskişehir city of Turkey based on the measured data. The results of statistical analyzing methods indicate that all of the new developed empirical models are more suitable for Eskişehir City. However it is concluded that proposed Model-4 can be used to calculate the global solar radiation with good accuracy based on the statistical error tests. Model-4 is given as follows;

$$\frac{H}{H_o} = 0.0315 + 1.528 \frac{S}{S_o} - 1.835 \left(\frac{S}{S_o}\right)^2 + 1.144 \left(\frac{S}{S_o}\right)^3$$

Turkey lies in a sunny belt between 36° and 42° N latitudes and is geographically well situated with respect to solar energy potential. If the information of solar radiation potential is very limited, the temperature based models are an essential and economical tool for estimating solar radiation. In this regard, the solar radiation potential can be easily estimated from Model-10/-11/-12 for Eskişehir and neighboring cities in the similar region and climate. Model-11 is statistically best temperature based model and given as follows;

$$H = 5.018 + 0.8669T + 0.00076T^2$$

NOMENCLATURE

| | |
|--------------|--|
| a, b, c, d | coefficients in empirical relationship(-) |
| c_a | average of calculated value |
| c_i | i 'th calculated value |
| E | relative percentage error (%) |
| G_a | extraterrestrial radiation $\left(\frac{W}{m^2}\right)$ |
| G_x | solar constant $\left(= 1367 \frac{W}{m^2}\right)$ |
| H | monthly average daily global solar radiation $\left(\frac{MJ}{m^2-day}\right)$ |
| H_o | monthly average daily extraterrestrial solar radiation $\left(\frac{MJ}{m^2-day}\right)$ |
| m_a | average of measured value |
| m_i | i th measured value |

| | |
|-----------|---|
| MBE | mean bias error $\left(\frac{M}{m^2-day}\right)$ |
| MPE | mean percentage error (%) |
| $MAPE$ | mean absolute percentage error (%) |
| n_{day} | number of days of the year starting from first January |
| R^2 | correlation coefficient (per %) |
| $RMSE$ | root mean square error $\left(\frac{M}{m^2-day}\right)$ |
| RSE | relative standard error (%) |
| S | day length (h) |
| S_o | daylight (bright sunshine) duration (h) |
| $SSRE$ | sum of squares of relative errors (%) |
| $t-stat$ | t-statistic (-) |
| Z | altitude (elevation) (m) |

Greek letters

| | |
|----------|--|
| δ | solar declination angle ($^{\circ}$) |
| ϕ | latitude of site ($^{\circ}$) |

REFERENCES

- [1] Teke, A., Yıldırım, H.B., Celik, O., (2015). Evaluation and performance comparison of different models for the estimation of solar radiation. Renewable and Sustainable Energy Reviews. 50:1097–1107. <https://doi.org/10.1016/j.rser.2015.05.049>
- [2] Behar, O., Khellaf, A., Mohammedi, K., (2015). Comparison of solar radiation models and their validation under Algerian climate-The case of direct irradiance. Energy Conversion and Management. 98:236–251. <https://doi.org/10.1016/j.enconman.2015.03.067>
- [3] Gueymard, C.A., (2014). A review of validation methodologies and statistical performance indicators for modeled solar radiation data: Towards a better bankability of solar projects. Renewable and Sustainable Energy Reviews. 39:1024–34. <https://doi.org/10.1016/j.rser.2014.07.117>
- [4] Gueymard, C.A., (2009). Direct and indirect uncertainties in the prediction of tilted irradiance for solar engineering applications. Solar Energy. 83:432–444. <https://doi.org/10.1016/j.solener.2008.11.004>
- [5] Ulgen, K., Hepbasli, A., (2009). Diffuse solar radiation estimation models for Turkey's big cities. Energy Conversion and Management. 50: 149–156. <https://doi.org/10.1016/j.enconman.2008.08.013>
- [6] Khorasanizadeh, H., Mohammadi, K., (2013). Introducing the best model for predicting the monthly mean global solar radiation over six major cities of Iran. Energy. 51:257–266. <https://doi.org/10.1016/j.energy.2012.11.007>
- [7] Yaiche, M.R., Bouhanik, A., Bekkouche, S.M.A., Malek, A., Benouaz, T., (2014). Revised solar maps of Algeria based on sunshine duration. Energy Conversion Management. 82:114–123. <https://doi.org/10.1016/j.enconman.2014.02.063>
- [8] Robaa, S.M., (2009). Validation of the existing models for estimating global solar radiation over Egypt. Energy Conversion and Management. 50:184–193. <https://doi.org/10.1016/j.enconman.2008.07.005>

- [9] Manzano, A., Martin, M.L., Valeroa, F., Armenta, C., (2015). A single method to estimate the daily global solar radiation from monthly data. *Atmospheric Research*. 166:70-82. <https://doi.org/10.1016/j.atmosres.2015.06.017>
- [10] Yao, W., Li, Z., Xiu, T., Lu, Y., Li, X., (2015). New decomposition models to estimate hourly global solar radiation from the daily value. *Solar Energy*. 120: 87-99. <https://doi.org/10.1016/j.solener.2015.05.038>
- [11] Mesri, M., (2015). Numerical methods to calculate solar radiation, validation through a new Graphic User Interface design. *Energy Conversion and Management*. 90: 436-445. <https://doi.org/10.1016/j.enconman.2014.11.037>
- [12] Mohammadi, K., Shamshirband, S., Tong, C.W., Alam, K.A., Petkovic, D., (2015). Potential of adaptive neuro-fuzzy system for prediction of daily global solar radiation by day of the year. *Energy Conversion and Management*. 93: 406-413. <https://doi.org/10.1016/j.enconman.2015.01.021>
- [13] Linares-Rodríguez, A., Ruiz-Arias, J.A., Pozo-Vázquez, D., Tovar-Pescador, J., (2011). Generation of synthetic daily global solar radiation data based on ERA-Interim reanalysis and artificial neural networks. *Energy*. 36: 5356-5365. <https://doi.org/10.1016/j.energy.2011.06.044>
- [14] Benghanem, M., Mellit, A., Alamri, S.N., (2009). ANN-based modeling and estimation of daily global solar radiation data: A case study. *Energy Conversion and Management*. 50: 1644-1655. <https://doi.org/10.1016/j.enconman.2009.03.035>
- [15] Sahin, M., Kaya, Y., Uyar, M., (2013). Comparison of ANN and MLR models for estimating solar radiation in Turkey using NOAA/AVHRR data. *Advances in Space Research*. 5:891-904. <https://doi.org/10.1016/j.asr.2012.10.010>
- [16] Koca, A., Oztop, H.F., Varol, Y., Koca, G.O., (2011). Estimation of solar radiation using artificial neural networks with different input parameters for Mediterranean region of Anatolia in Turkey. *Expert Systems with Applications*. 38: 8756-8762. <https://doi.org/10.1016/j.eswa.2011.01.085>
- [17] Qazi, A., Fayaz, H., Wadi, A., Raj, R.G., Rahim, N.A., Khan, W.A., (2015). The artificial neural network for solar radiation prediction and designing solar systems: a systematic literature review. *Journal of Cleaner Production*. 104:1-12. <https://doi.org/10.1016/j.jclepro.2015.04.041>
- [18] Park, J.K., Das, A., Park, J.H., (2015). A new approach to estimate the spatial distribution of solar radiation using topographic factor and sunshine duration in South Korea. *Energy Conversion and Management*. 101: 30-39. <https://doi.org/10.1016/j.enconman.2015.04.021>
- [19] Hassan, G.E., Youssef, M.E., Mohamed, Z.E., Ali, M.A., Hanafy, A.A., (2016). New temperature-based models for predicting global solar radiation. *Applied Energy*. 179: 437-450. <https://doi.org/10.1016/j.apenergy.2016.07.006>
- [20] Yıldızay, H.D., (2015). Eskişehir ve yöresinde enerji üretimi amaçlı güneş ışınımı ve rüzgar hızı değerlerinin tespiti ve kullanılabilirliğini analizi. Determination of solar radiation and wind speed values for energy generation and availability analysis in Eskişehir region. Doctoral Thesis. Eskişehir Osmangazi Üniversitesi.
- [21] Zang, H., Cheng, L., Ding, T., Cheung, K.W., Wang, M., Wei, Z., Sun, G., (2019). Estimation and validation of daily global solar radiation by day of the year-based models for different climates in China. *Renewable Energy*. 135: 984-1003. <https://doi.org/10.1016/j.renene.2018.12.065>
- [22] Jamil, B., Siddiqui, A.T., (2017). Generalized models for estimating of diffuse solar radiation based on clearness index and sunshine duration in India: Applicability under different climatic zones. *Journal of Atmospheric and Solar-Terrestrial Physics*. 157-158:16-34. <https://doi.org/10.1016/j.jastp.2017.03.013>
- [23] Behar, O., Khellaf, A., Mohammedi, K., (2015). Comparison of solar radiation models and their validation under Algerian climate- The case of direct irradiance. *Energy Conversion and Management*. 98: 236-251. <https://doi.org/10.1016/j.enconman.2015.03.067>
- [24] Duffie, J.A., Beckman, W.A., (2006). *Solar engineering of thermal processes*. 3rd ed. New York: John Wiley & Son.
- [25] Angstrom, A., (1924). *Solar and Terrestrial Radiation Report to the International Commission for Solar Research on Actinometric Investigations of Solar and Atmospheric Radiation*. Q. J. R. Meteorol. Soc.,50: 121-126.
- [26] Prescott, J.A., (1940). Evaporation from water surface in relation to solar radiation. *Trans Roy Soc Austr.* 46:114-118.
- [27] Page, J.K., (1961). The estimation of monthly mean values of daily total short wave radiation on vertical and inclined surface from sunshine records for latitudes 40N-40S. *Proceedings of UN Conference on New Sources of Energy*. 4: 378-390.
- [28] Chang, K., Zhang, Q., (2019). Improvement of the hourly global solar model and solar radiation for air-conditioning design in China. *Renewable Energy*. 138: 1232-1238. <https://doi.org/10.1016/j.renene.2019.02.069>
- [29] Tarhan, S., Sari, A., (2005). Model selection for global and diffuse radiation over the Central Black Sea (CBS) region of Turkey. *Energy Conversion and Management*. 46(4): 605-613. <https://doi.org/10.1016/j.enconman.2004.04.004>
- [30] Bakirci, K., (2009). Correlations for estimation of daily global solar radiation with hours of bright sunshine in Turkey. *Energy*. 34:485-501. <https://doi.org/10.1016/j.energy.2009.02.005>
- [31] Katiyar, A.K., Pandey, C.K., (2010). Simple correlation for estimating the global solar radiation on horizontal surfaces in India. *Energy*. 35:5043-5048. <https://doi.org/10.1016/j.energy.2010.08.014>
- [32] Li, H., Ma, W., Lian, Y., Wang, X., Zhao, L., (2011). Global solar radiation estimation with sunshine duration in Tibet. *China Renewable Energy*. 36:3141-3145. <https://doi.org/10.1016/j.renene.2011.03.019>
- [33] Behrang, M.A., Assareh, E., Noghrehabadi, A.R., Ghanbarzadeh, A., (2011). New sunshine-based models for predicting global solar radiation using PSO (particle swarm optimization) technique. *Energy*. 36:3036-3049. <https://doi.org/10.1016/j.energy.2011.02.048>
- [34] Duzen, H., Aydin, H., (2012). Sunshine-based estimation of global solar radiation on horizontal surface at Lake Van region (Turkey). *Energy Conversion and Management*. 58: 35-46. <https://doi.org/10.1016/j.enconman.2011.11.028>
- [35] Teke, A., Yıldırım, H.B., (2014). Estimating the monthly global solar radiation for Eastern Mediterranean Region. *Energy Conversion and Management*. 87:628-635. <https://doi.org/10.1016/j.enconman.2014.07.052>
- [36] Chelbi, M., Gagnon, Y., Waewsak, J., (2015). Solar radiation mapping using sunshine duration based models and interpolation techniques: application to Tunisia. *Energy Conversion and Management*. 101: 203-215. <https://doi.org/10.1016/j.enconman.2015.04.052>
- [37] Dincer, I., Dilmac, S., Ture, I.E., Edin M., (1996). A simple technique for estimating solar radiation parameters and its application for Gebze. *Energy Conversion and Management*. 37 (2):183-198. [https://doi.org/10.1016/0196-8904\(95\)00168-D](https://doi.org/10.1016/0196-8904(95)00168-D)
- [38] Dumas, A., Andrisani, A., Bonnici, M., Graditi, G., Leanza, G., Madonia, M., Trancossi, M., (2015). A new correlation between global solar energy radiation and daily temperature variations. *Solar Energy*. 116:

- 117–124. <https://doi.org/10.1016/j.solener.2015.04.002>
- [39] Trabea, A.A., Shaltout, M.A.M., (2000). Correlation of global solar radiation with meteorological parameters over Egypt. *Renewable Energy*. 21:297-308. [https://doi.org/10.1016/S0960-1481\(99\)00127-5](https://doi.org/10.1016/S0960-1481(99)00127-5)
- [40] Annandale, J., Jovanovic, N., Benadé, N., Allen, R., (2002). Software for missing data error analysis of Penman–Monteith reference evapotranspiration. *Irrigation Science*. 21:57-67. <https://doi.org/10.1007/s002710100047>
- [41] Allen, R.G., (1997). Self-calibrating method for estimating solar radiation from air temperature. *J Hydrolic Engineering*. 2(2):56-67. [https://doi.org/10.1061/\(ASCE\)1084-0699\(1997\)2:2\(56\)](https://doi.org/10.1061/(ASCE)1084-0699(1997)2:2(56))
- [42] Goodin, D., Hutchinson, J., Vanderlip, R.L., Knapp, M.C., (1999). Estimating solar irradiance for crop modeling using daily air temperature data. *Acronomy Journal*. 91(5): 845-851. <https://doi.org/10.2134/agronj1999.915845x>
- [43] Tapakis, R., Michaelides, S., Charalambides, A.G., (2016). Computations of diffuse fraction of global irradiance: Part 1– Analytical modelling. *Solar Energy*. 139:711-722. <https://doi.org/10.1016/j.solener.2014.10.005>
- [44] Kurtz, B., Kleissl, J. (2017). Measuring diffuse, direct, and global irradiance using a sky imager. *Energy*. 141: 311-322. <https://doi.org/10.1016/j.solener.2016.11.032>
- [45] Mghouchi, Y.E., Bouardi, A.E., Choulli, Z., Ajzoul, T., (2016). Models for obtaining the Daily direct, diffuse and global solar radiations. *Renewable and Sustainable Energy Reviews*. 56: 87-99. <https://doi.org/10.1016/j.rser.2015.11.044>
- [46] Yorukoglu, M., Celik, A.N., (2006). A critical review on the estimation of daily global solar radiation from sunshine duration. *Energy Conversion and Management*. 47 (15):2441-2450. <https://doi.org/10.1016/j.enconman.2005.11.002>



Electromagnetic Analysis of Organic Waste and Blast Furnace Slag Mixtures

Mustafa Kaan Baltacıoğlu^{1*} , Mustafa Tunahan Başar² , Muharrem Karaaslan³ ,
Fatih Özkan Alkurt³ , Samet Alparslan Arıpek⁴ 

^{1,4}İskenderun Technical University, Engineering and Natural Sciences Faculty, Mechatronics Engineering Dep., Turkey

²İskenderun Technical University, Engineering and Natural Sciences Faculty, Mechanical Engineering Dep., Turkey

³İskenderun Technical University, Engineering and Natural Sciences Faculty, Electrical Engineering Dep., Turkey

Abstract

In this experimental study, a composite structure was obtained by combining apple pulp wastes with slag wastes. Electromagnetic field characteristics of test samples have been determined. In the scope of the study, dry apple pulp and slag wastes were transformed into square plate form using a specially designed mold and a pressing bench with a capacity of 50 tons. The measurements were carried out in the 3-18 GHz frequency band in the microwave laboratory. In the measurements, five different measurement results were obtained: air, high quality commercial absorber, pure apple pulp, 50 g apple pulp with slag and 150 g of slag added apple pulp. The results of the measured samples were compared and interpreted with the results of air and high quality commercial absorber material. As a result, the samples formed by pure apple pulp, 50 g slag-added sample and 150 g slag-added sample in terms of electromagnetic permeability similar results were obtained. The slag-added sample of 50 g performed better absorption in certain frequency regions than the slag-added sample of 150 g. In addition, it produces close transmission values in three samples in the 8-12 GHz X-band frequency range. In addition, considering the absorption values of the slag-added structures, it was determined that they absorb signals 90% on average in the frequency regions of 8 GHz and above.

Keywords: Organic waste, blast furnace slag, absorber, electromagnetic conductivity.

35. INTRODUCTION

Due to the increasing consumption trend with the developing technology, environmental pollution and dramatic waste formation occur on a global scale. This situation poses a great threat to the environment and human health [1]. On the other hand, considering the limited raw material resources and the increase in raw material needs, the idea of meeting the raw material need from waste arises [2].

Waste recovery is very important for economic sustainability. Therefore, developed and developing countries tend to work on the recovery and efficient use of waste [3]. Waste can be classified according to many parameters such as economic values, amount of formation, recovery conditions. However, they are classified as waste, organic waste, metal waste, plastic waste, electronic waste, paper-cardboard waste according to the amount of formation. When evaluated to its formation, most waste generation is observed in organic waste [4].

Increased waste generation for waste recovery is also associated with increased energy demand. Converting waste to energy has great advantages in terms of economic conditions and environment. Therefore, encouraging decisions have been taken in various countries around the world to provide energy recovery from waste [5-7]. The Government of India has seen agricultural waste as a significant income potential. In this context, studies have shown that farmers gain high income from biogas production and worm fertilization [8]. On the other hand, considering the dependence on fossil fuels, the fact that fossil fuels are exhaustible and pose an environmental threat reveals results that support the idea of using organic wastes as energy and raw materials [9-10]. If organic wastes are not utilized, their storage poses a problem. In addition, during traditional disposal methods, problems such as the inadequacy of the lands, the emission of greenhouse gases and the spread of harmful substances to the environment arise [11-13]. When organic wastes are integrated into recovery, it is possible to gain energy and raw materials. Organic wastes can be used as an energy source,

* Corresponding author
Email: mkaan.baltacioglu@iste.edu.tr



especially in obtaining biogas and using it in electricity generation [14-16].

Organic wastes, which are generally used for energy production, can also be used as a raw material source. In some studies, it is seen that it is appropriate to use agricultural wastes in animal feed production [17]. In another study conducted for the evaluation of food wastes, the chemical properties of some food wastes were examined. These wastes found that they have the potential to be reused in the production of products such as drugs and food supplements [18]. In a study conducted on the determination of some mechanical properties of organic wastes, the electromagnetic field and thermal properties of pomegranate seed wastes were tried to be determined and it was mentioned that these wastes could be added as additives to the compositions of thermal insulation, electromagnetic absorber, etc. [19-20]. In addition, absorber and radome applications have an important place in electromagnetic field applications [21].

In this study, it was tried to determine the electromagnetic field properties of the sample obtained by steel powder (slag) wastes used in the iron and steel industry with organic wastes. Within the scope of the study, the experimental results of pure apple pulp and slag-added apple pulp were examined in detail. The comparisons of both samples in terms of cutting or not affecting the signals on the electromagnetic field permeability are presented by graphical analysis.

36. MATERIALS AND METHODS

In this study, apple pulp wastes and metal wastes (slag) were selected as samples in experimental studies. First of all, the algorithm that enables organic wastes to be converted to sample format is shown in Figure 2.1. The waste product to be recycled is determined from organic wastes with a wide product potential. In the ongoing process, the determined waste product must be separated into structures such as water, shell and pulp. Decomposed waste structures are subjected to dehumidification and dried in the oven in order to prevent decay. Then, in order to determine the electromagnetic properties of the samples, the test samples are made ready by a press bench with a capacity of 50 tons and a specially produced square plate production mold.

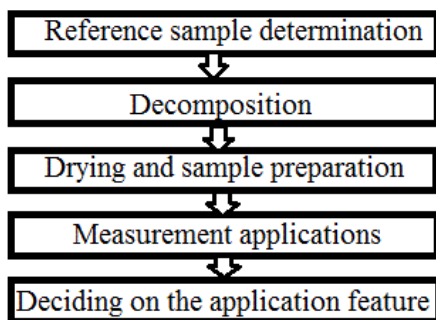


Figure 2.1. Wastw recovery algorithm

The slag used in the study was purchased from İskenderun Demir ve Çelik Company and its specific gravity is 2.89 g

/ cm³ and Blaine fineness is 540 m² / kg. In addition, the chemical properties of the slag are shown in Table 2.1.

Table 2.1. Chemical properties of blast furnace slag [22].

| Chemical composition | Analysis results of slag (%) |
|--------------------------------|------------------------------|
| CaO | 36.25 |
| SiO ₂ | 34-36 |
| SO ₃ | 0.60 |
| Na ₂ O | 0.28 |
| K ₂ O | 0.75 |
| S ⁻² | 0.51 |
| Al ₂ O ₃ | 11.34 |
| Fe ₂ O ₃ | 0.74 |
| MgO | 6.10 |
| Loss of glow | 0 |
| Free Lime | 0 |

The drying oven shown in Figure 2.2 is an oven with a capacity of 300 °C, powered by electricity and generating heat with the resistances inside. The waste samples laid on metal plates are dehumidified for 4 hours at 82 °C in this oven and converted into a form suitable for pressing.



Figure 2.2. Drying oven

The dried organic waste samples and slag wastes are converted into sample format with a specially designed mold and pressing bench.



Figure 2.3. Square Plate Production Mold Parts

As shown in Figure 2.3 the mold pressing block, designed to produce samples with a surface area of 16x16 cm² and a thickness of 5 mm - 50 mm, consists of a total of four main elements: lower table, female mold and sample extraction legs. Here, the thrust block is made of 1050 steel and is resistant to high pressures. The mold cavity is worked with 10⁻³cm measurement accuracy. The lower table is the part on

which the sample is pressed and it is made of st-37 steel. The female mold serves as the filling chamber of the sample and is the most important part of the mold. This part is made of 2040 manufacturing steels and the working gap is designed with 10^{-3} cm precision.



Figure 2.4. Pressing Bench

The pressing bench shown in Figure 2.4 is a bench with a maximum capacity of 50 tons and can be operated manually. A specially produced mold is placed between the upper and lower jaws seen on the counter. After the mold cavity and compression blocks are fixed, pressing at the desired value can be applied to the sample in the mold cavity through the control screen of the device. With the help of the screen on the pressing machine unit, the applied pressure value is observed and can be adjusted to the desired values instantly.

Two-port Agilent N5234A PNA-L Microwave Network Analyzer was used to determine the properties of the prepared samples.

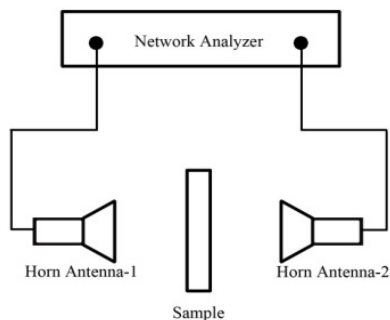


Figure 2.5. Schematic view of Agilent N5234A PNA-L Microwave Network Analyzer

The schematic view of the test setup established to determine the electromagnetic behavior of the samples is as shown in Figure 2.5. Testing is carried out by placing samples at the midpoint of two broadband linearly polarized horn antennas. Network analyzer is used to measure the parameters S11, S12, S21 and S22 for a two-port system called scatter parameters (S-parameters). Here, S11 and S22 represent the amount of power reflected back from the first and second ports, respectively, while the parameters S12 and S21 show the power transferred between the two ports. As a result, the parameters S11 and S22 selected as reflection

parameters are equal to each other, and in the same way, the parameters S12 and S21, which are evaluated as transmission parameters, are equal to each other.



Figure 2.6. Electromagnetic test setup and test application

While performing the measurements, firstly, the calibration process of the device is performed in three conditions, open, closed and short circuit. Then the measurement for air is taken as a reference. Finally, produced samples are subjected to the measurement process as seen in Figure 2.6. The samples are made by placing the samples vertically between two antennas at a distance of 10 cm from each antenna.

37. RESULTS AND DISCUSSION

In this section, reflection and transmission values of samples prepared by experimental studies in the microwave laboratory have been obtained. As is known, empty air environments do not affect electromagnetic signals in terms of reflection or transmission parameters. Therefore, the air environment reflection and transmission parameters were determined in the device first, and other measurements were interpreted according to the air reference. In addition, measurement results were obtained for a professional absorber material currently in use, and electromagnetic characteristics were obtained for pure apple, 50 g slag-added sample and 150 g slag-added sample according to their close behavior to air and absorber material.

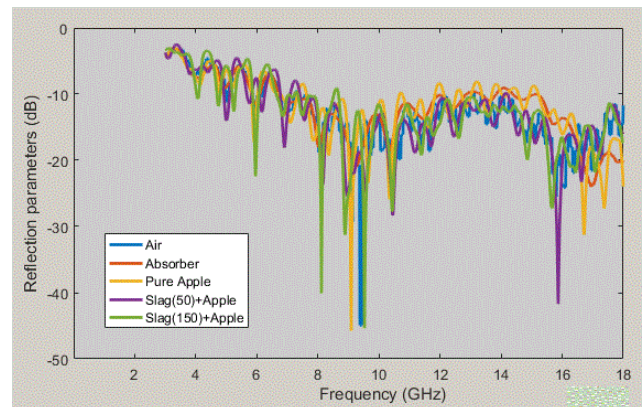


Figure 3.1. Reflection parameters of samples after electromagnetic field test

The reflection values obtained with five different setups are as shown in Figure 3.1. These five different mechanisms are described in the following order;

- Air
- Electromagnetic absorber
- pure apple sample
- 50gr Slag and Apple combination
- 150gr Slag and Apple combination

Here, when the reflection values are compared with air, the retro reflection values of the combinations of slag and apple samples occur in a multi-band fashion, which supports the idea that the signals are not reflected back.

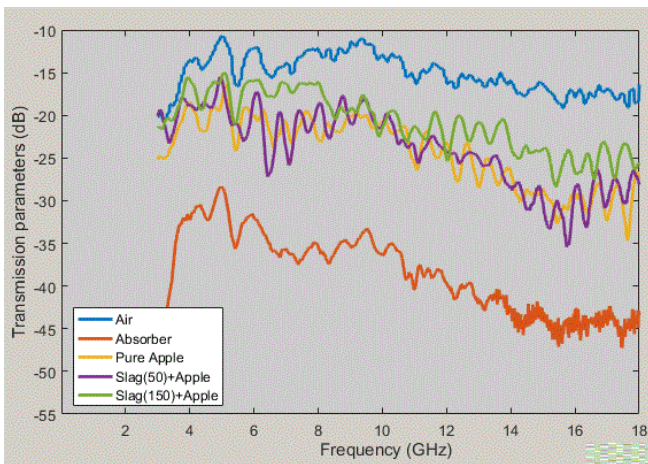


Figure 3.2. Transmission parameters of samples after electromagnetic field tests

Transmission values between two antennas have been measured with five different setups and are given in Figure 4.2. As shown in Figure 4.2, compared to air, the combination of apple and slag-apple structures reduce the transmission value in the 3-18 GHz range. The structure using 50gr slag in the 6-8 GHz and 13-16 GHz bands reduces the transmission value by approximately 10 dB compared to the structure using 150 gr slag. Remarkably, when the slag addition is increased, the transmission values decrease. In addition, when the frequency range of 8-12 GHz is examined in transmission parameters, it is seen that transmission losses at the

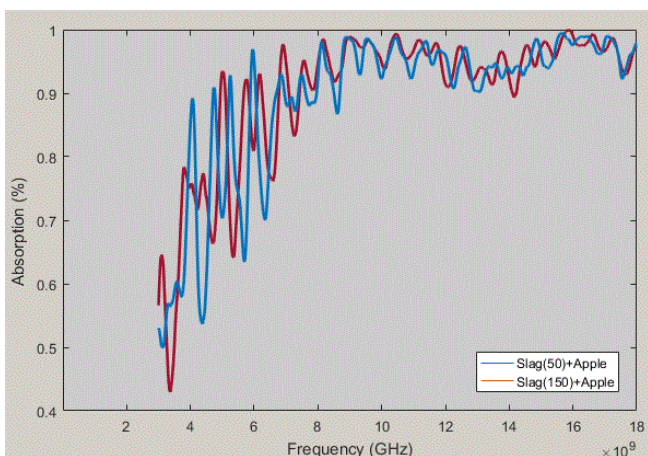


Figure 3.3. Signal absorption characteristic of 50 g slag-added sample and 150 g slag-added sample

same levels are observed in pure apple, 50 g slag-added apple and 150 g slag-added apple structures. In this case, it was determined that the slag addition does not provide great advantages to the pure apple pulp structure in terms of electromagnetic permeability in some frequency regions.

S11 (reflection values) and S12 (transmission values obtained as a result of electromagnetic field tests can be calculated with the help of the formula shown in Eq.1 for each sample.

$$Absorption = 1 - (|S11|^2) - (|S12|^2) \quad (1)$$

The reflection and transmission values obtained by using the absorption equation were converted from decibels to linear. The graph given in Figure 4.3 gives the electromagnetic signal absorption characteristic of both slag combinations. The developed samples perform excellent signal absorption in the 10.25 GHz and 15.8 GHz frequency regions. In addition, there is an average of 90% signal absorption in the 8-17 GHz range.

In the light of the results obtained, it is predicted that the proposed sample can be used in communication systems such as radar. In addition, these frequency regions have a wide range of applications.

38. CONCLUSION

In general, millions of tons of waste derivatives are dysfunctional worldwide and pose problems for the environment and public health. In this study, by approaching waste recovery with an innovative perspective, a new structure was obtained by combining apple pulp, an organic waste, and slag samples with metal waste, and the electromagnetic absorption characteristic of this samples was examined in detail. In this context, it has been proved that it is possible to develop absorber materials that are economically used in high value-added technologies in the study conducted on recycling waste.

With the samples proposed in the study, it has been shown that it is possible to obtain absorption with high efficiency, especially in high frequency regions. Considering the general findings, it has been determined that studies on the physical combination of slag wastes and apple pulp wastes need to be deepened and the results change negatively when a certain amount of slag additions are exceeded in terms of electromagnetic field permeability. Ensuring improvements in combining two waste structures with each other during the sample preparation process and determining the optimum slag amount in a more convergent result between these two reference measurements can be a source for future studies.

RERENCES

- [1] Karak, T., Bhagat, R. M., & Bhattacharyya, P. (2012). Municipal solid waste generation, composition, and management: the world scenario. *Critical Reviews in Environmental Science and Technology*, 42(15), 1509-1630. DOI: <https://doi.org/10.1080/10643389.2011.569871>

- [2] Giugliano, M., Cernuschi, S., Grosso, M., & Rigamonti, L. (2011). Material and energy recovery in integrated waste management systems. An evaluation based on life cycle assessment. *Waste Management*, 31(9-10), 2092-2101. DOI: <https://doi.org/10.1016/j.wasman.2011.02.029>
- [3] Li, Y., Jin, Y., Borrion, A., & Li, H. (2019). Current status of food waste generation and management in China. *Bioresource technology*, 273, 654-665. DOI: <https://doi.org/10.1016/j.biortech.2018.10.083>
- [4] Kaza, S., Yao, L., Bhada-Tata, P., & Van Woerden, F. (2018). What a waste 2.0: a global snapshot of solid waste management to 2050. The World Bank. DOI: <https://doi.org/10.1596/978-1-4648-1329-0>
- [5] Alzate-Arias, S., Jaramillo-Duque, Á., Villada, F., & Restrepo-Cuestas, B. (2018). Assessment of government incentives for energy from waste in Colombia. *Sustainability*, 10(4), 1294. DOI: <https://doi.org/10.3390/su10041294>
- [6] Jeswani, H. K., & Azapagic, A. (2016). Assessing the environmental sustainability of energy recovery from municipal solid waste in the UK. *Waste Management*, 50, 346-363. DOI: <https://doi.org/10.1016/j.wasman.2016.02.010>
- [7] Scarlat, N., Motola, V., Dallemand, J. F., Monforti-Ferrario, F., & Mofor, L. (2015). Evaluation of energy potential of municipal solid waste from African urban areas. *Renewable and Sustainable Energy Reviews*, 50, 1269-1286. DOI: <https://doi.org/10.1016/j.rser.2015.05.067>
- [8] Singh, A., Tiwari, R., Chandrahas, & Dutt, T. (2020). Augmentation of farmers' income in India through sustainable waste management techniques. *Waste Management & Research*, 0734242X20953892. DOI: <https://doi.org/10.1177/0734242X20953892>
- [9] Saprónova, Z., Sverguzova, S., & Svyatchenko, A. (2019, December). Use of municipal vegetative waste as raw material for sorbent production. In *IOP Conference Series: Materials Science and Engineering* (Vol. 687, No. 6, p. 066061). IOP Publishing.
- [10] Heredia-Guerrero, J. A., Heredia, A., Domínguez, E., Cingolani, R., Bayer, I. S., Athanassiou, A., & Benítez, J. J. (2017). Cutin from agro-waste as a raw material for the production of bioplastics. *Journal of experimental botany*, 68(19), 5401-5410. DOI: <https://doi.org/10.1093/jxb/erx272>
- [11] Rong, W. U., Shanjiang, L. I. U., & Ying, D. U. (2016). Research Advances in Agricultural Reutilization of Urban-rural Organic Wastes. *Agricultural Science & Technology*, 17(2).
- [12] Liu, Y., Ni, Z., Kong, X., & Liu, J. (2017). Greenhouse gas emissions from municipal solid waste with a high organic fraction under different management scenarios. *Journal of Cleaner Production*, 147, 451-457. DOI: <https://doi.org/10.1016/j.jclepro.2017.01.135>
- [13] Hoornweg, D., & Bhada-Tata, P. (2012). What a waste: a global review of solid waste management.
- [14] Kumar, A., & Samadder, S. R. (2020). Performance evaluation of anaerobic digestion technology for energy recovery from organic fraction of municipal solid waste: A review. *Energy*, 117253. DOI: <https://doi.org/10.1016/j.energy.2020.117253>
- [15] Tufaner, F., & Avcı, Y. (2014). Yenilenebilir Bir Enerji Kaynağı Olarak Organik İçeriği Yüksek Atıklardan Biyogaz Üretim Teknolojisi. *Adıyaman Üniversitesi Bilim, Kültür ve Sanat Sempozyumu (ADYÜ-Sempozyum)*.
- [16] Rayner, A. J., Briggs, J., Tremback, R., & Clemmer, R. M. (2017). Design of an organic waste power plant coupling anaerobic digestion and solid oxide fuel cell technologies. *Renewable and Sustainable Energy Reviews*, 71, 563-571. DOI: <https://doi.org/10.1016/j.rser.2016.12.084>
- [17] San Martín, D., Ramos, S., & Zufía, J. (2016). Valorisation of food waste to produce new raw materials for animal feed. *Food chemistry*, 198, 68-74. DOI: <https://doi.org/10.1016/j.foodchem.2015.11.035>
- [18] Mirabella, N., Castellani, V., & Sala, S. (2014). Current options for the valorization of food manufacturing waste: a review. *Journal of Cleaner Production*, 65, 28-41. DOI: <https://doi.org/10.1016/j.jclepro.2013.10.051>
- [19] Üstün, İ., Koç, Y., Yağlı, H., Köse, Ö., Başar, M., Karakuş, C., Akgöl, O., Koç, A. (2019). Determination of heat transfer coefficient and electromagnetic directional analysis of pomegranate seed. *International Advanced Researches and Engineering Journal*, 3 (2), 98-104. DOI: 10.35860/iarej.412270
- [20] Başar, M. T. (2020). Organik atıkların geri kazanımı için mekanik, ısı ve elektromanyetik özelliklerinin araştırılması (Master's thesis, İskenderun Teknik Üniversitesi/Mühendislik ve Fen Bilimleri Enstitüsü/Makine Mühendisliği Anabilim Dalı).
- [21] Abdulkarim, Y. I., Deng, L., Altıntaş, O., Ünal, E., & Karaaslan, M. (2019). Metamaterial absorber sensor design by incorporating swastika shaped resonator to determination of the liquid chemicals depending on electrical characteristics. *Physica E: Low-dimensional Systems and Nanostructures*, 114, 113593. DOI: <https://doi.org/10.1016/j.physe.2019.113593>
- [22] Balçıklı, M. (2016). Alkalilerle aktive edilmiş çimentosuz cüruf lu betonların mekanik ve geçirimsizlik özellikleri ve üretim optimizasyonu (Master's thesis, İskenderun Teknik Üniversitesi/Mühendislik ve Fen Bilimleri Enstitüsü/İnşaat Mühendisliği Anabilim Dalı).